Dissertations (1934 -)   Dissertations, Theses, and Professional
                                                                    Projects

Resonant Two-Photon Ionization and Velocity Mapped Ion Imaging Studies of Aromatic Van Der Waals Complexes

James T. Makuvaza
Marquette University

RESONANT TWO-PHOTON IONIZATION AND VELOCITY-MAPPED ION
IMAGING STUDIES OF AROMATIC VAN DER WAALS COMPLEXES

by

James T. Makuvaza, BSc
A dissertation submitted to the Faculty of the Graduate School,
Marquette University,
in partial fulfillment of the requirements for
the Degree of Doctor of Philosophy

Milwaukee, Wisconsin

August 2021

ABSTRACT
RESONANT TWO-PHOTON IONIZATION AND VELOCITY-MAPPED ION
IMAGING STUDIES OF AROMATIC VAN DER WAALS COMPLEXES

James T. Makuvaza, BSc

The study of van der Waals complexes provides a means for understanding the nature and strength of non-covalent interactions. Non-covalent interactions including C-H/π, C-H/O, C-H/N, C-H/F, halogen and chalcogen bonding are found in important intermediates that regulate chemical and biological processes in many forefront areas of science including molecular self-assembly, drug substrate interactions, supramolecular chemistry, crystal engineering and biochemistry. To better understand these interactions, laser spectroscopic techniques that include mass selected two color resonant two photon ionization (2CR2PI) and velocity mapped ion imaging spectroscopy in combination with complementary *ab initio* calculations were used to probe the electronic structure, geometries, and binding strengths in aromatic van der Waals clusters. Prototypical systems of anisole$\cdots(CH_4)_n$, aniline$\cdots(CH_4)_n$ (n=1,2) and toluene$\cdots CH_3F$ were utilized for probing the cooperation/competition of C-H/π with C-H/O, C-H/N and C-H/F interactions. For anisole-CH_4 1:1 complex, we found a dual presence of C-H/O and C-H/π interactions, consistent with the observation that the measured S_0 binding energy is additive of energies determined for systems exhibiting only C-H/π and C-H/O interactions. In a follow up study on anisole-methane 1:2 complex, to probe the degree of cooperativity, the binding energies increased relative to the 1:1 complex across the three electronic states (S_0, S_1, D_0), indicative of cooperative binding. For the aniline-methane 1:1 and 1:2 complexes the binding strength in the three electronic states were also determined. Similar to anisole-methane 1:1 complex, the aniline-CH_4 was stabilized by both C-H/π and C-H/N interactions, and the S_0 binding energy was additive when compared to that of systems exhibiting only C-H/π and C-H/N interactions. Contrary to anisole-methane 1:2 complex which showed an enhanced binding, the S_0 binding energy required to remove one methane from aniline-CH_4 1:2 complex decreased, indicating a loss in cooperative binding. The experimental results reported are in good agreement with the *ab initio* calculations performed. A theoretical study on Toluene$\cdots CH_3F$ complex using Density Functional (DFT) methods benchmarked from studies of complexes of CH_4 with anisole and aniline also show a dual presence in binding (C-H/π and C-H/F interactions). The predicted ground state binding energy is also additive when compared to that of systems only exhibiting C-H/π and C-H/F interactions.

ACKNOWLEDGEMENTS

James T. Makuvaza, BSc

TABLE OF CONTENTS

LIST OF TABLES

LIST OF FIGURES

GLOSSARY OF ACRONYMS AND ABBREVIATIONS

BBO: beta-Barium Borate

BE: Binding Energy

BSSE: Basis Set Superposition Error

2CAP: Two Color Appearance Potential

DCM: 4-Dicyanomethylene-2-methyl-6-p-dimethylaminostyrl-4H-pyran

DFT: Density Functional Theory

DNA: Deoxyribonucleic acid

HF: Hartree - Fock

IP: Ionization Potential

MCP's: Microchannel plates

Nd:YAG: Neodymium-doped yttrium aluminum garnet

REMPI: Resonance Enhanced Multiphoton Ionization

R2PI: Resonance Two Photon Ionization

2CR2PI: Two Color Resonance Two Photon Ionization

RNA: Ribonucleic acid

TOF: Time of flight

TDDFT: Time Dependent Density Functional Theory

VMI: Velocity Mapped Imaging

CHAPTER 1: RESONANT TWO PHOTON IONIZATION STUDIES OF NON-COVALENT INTERACTIONS

This chapter gives an overview of the various non-covalent interactions and a detailed description of the instrumentation used for the investigations. The experimental method used to produce the jet cooled molecular clusters, and the spectroscopic and theoretical methods used to characterize the weakly bound clusters will also be discussed.

1.1 INTRODUCTION TO NONCOVALENT INTERACTIONS

Non-covalent (neither a bond is formed or broken) interactions are notably weaker than covalent interactions, with the total stabilization energy of a molecular cluster usually lying between 1 and 10 kcal/mol, significantly less than the energy of a covalent bond, which is in the order of 100 kcal/mol. Such interactions originate from the interaction of permanent multipoles, or a permanent multipole and an induced multipole, or between an instantaneous time variable multipole and induced multipole.[1] The respective energy terms are generally attractive and can be categorized as electrostatic, induction and dispersion.[2] Typically, several attractive terms contribute to the overall stabilization of a given non-covalent cluster. Various non-covalent interactions fall into a general class of donor (electron-rich) acceptor (electron-poor) interactions, and these include hydrogen bonding, C/H-π, C/H-O and halogen bonding and other σ-hole type of interactions.

Non-covalent interactions play a subtle but decisive role in nature, impacting a vast array of fields spanning biochemistry, drug substrate interactions, anion recognition,

crystal engineering, molecular self-assembly and supramolecular chemistry. The prevalence of non-covalent interactions in nature is evidenced by hydrogen bonding interactions as the main driving force that determines the structure of macromolecules such as DNA and protein side chains. In DNA base pairs, responsible for the transfer of genetic information, the structure is determined by the strong and specific hydrogen bonding, whilst the overall stability of the double helix is determined by the vertical $\pi - \pi$ stacking originating from the dispersion interactions.[1,2] Hydrogen bonding and other non-covalent interactions can also be involved in a cooperative interaction important for enzyme – substrate binding at the active site.[3]

Insight into all these processes is gleaned from the study of molecular complexes, which provide a bridge from isolated gas phase molecules to condensed phases, enabling us to gain invaluable insights on solvation processes, solution dynamics, and the nucleation and growth of complexes. Isolated molecular clusters with well-defined composition exhibiting intermolecular bonds originating from non-covalent interactions can be prepared experimentally using jet cooled supersonic expansions (molecular beams). Due to the weakness of the noncovalent interaction, the study of these forces is only possible at low temperature. Within the rarified environment of a supersonic expansion, where molecules are rapidly cooled in expansion from high pressure region into vacuum, such complexes can be readily formed and stabilized. However, the composition of the cluster is not easily controlled and thus combining supersonic expansion methods with mass spectrometry is a powerful tool for elucidation of such complexes. The characterization of the clusters is successfully carried out based on spectral changes of the chromophore upon cluster formation.

Previous studies of weakly bound clusters have often utilized a reference chromophore consisting of an aromatic molecule bound to a different atom or molecule (rare gas atom, diatomic or small polyatomic molecules). The aromatic chromophore can typically be spectroscopically detected via fluorescence and with mass selected resonant two photon ionization (R2PI) methods allowing for the interrogation of the cluster. For example, infrared spectroscopy and high-level *ab initio* calculations were employed on several isolated methane clusters with benzene, toluene, naphthalene, mesitylene and *p*-xylene in the gas phase to support the existence of C/H-π interactions.[4] As another example, simple aromatic dimers of toluene and benzene have long been proposed as model systems for investigating C/H-π and π-π stacking interactions in proteins, and Bernstein and co-workers reported the first excitation spectrum of toluene dimer using R2PI spectroscopy.[5] Similar studies have been reported on substituted benzene dimers including dimers of fluorobenzene, chlorobenzene, phenol, aniline, and other analogues.[6–8]

1.1.1 HYDROGEN BONDING INTERACTIONS

Hydrogen bonding is an important non-covalent interaction in which a hydrogen atom bound to an electronegative atom X (usually F, N, or O) interacts with a nucleophilic atom on another molecule. The interaction can be represented according to the following scheme, D-H···A, where D is the proton donor and A the acceptor. When the hydrogen atom loses its electron density in a polar bond, it essentially becomes capable of forming a strong interaction with the lone pair on an adjacent electronegative

atom. This type of interaction is best explained by the presence of a region of positive

electrostatic potential on the outer surface of the hydrogen atom, which is directed along

the X-H bond, as illustrated in Figure 1.1-1 below for water. This accounts for the

directionality of hydrogen bonding.
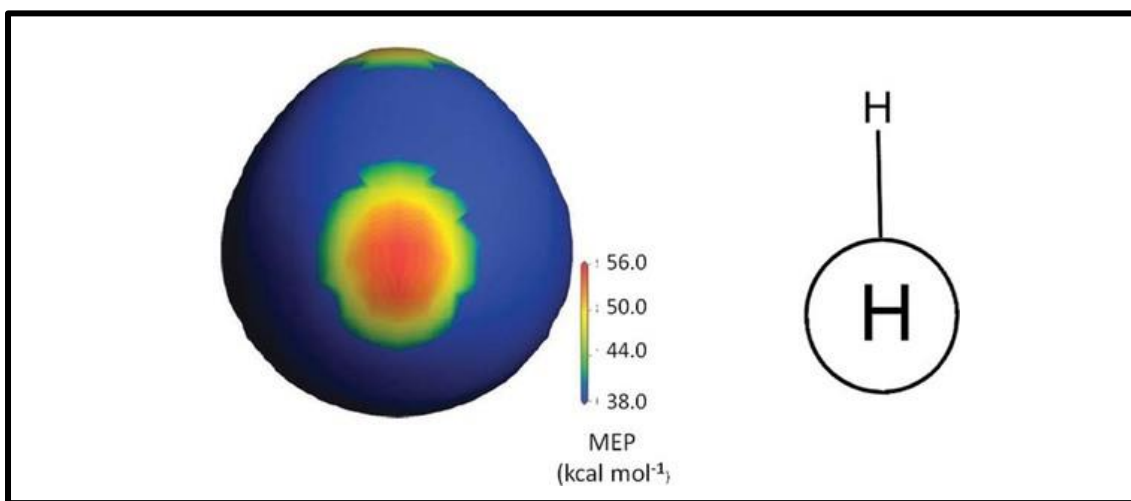
Figure 1.1-1: Electrostatic potential map of a water molecule viewed along the H-O bond. The scale to the right indicates the potential in units of kcal/mol. Taken from ref. 9.

Complexes which undergo hydrogen bonding are stabilized by electrostatic (the

most attractive contribution), dispersion and charge transfer energy terms which gives the

hydrogen bond their often and very important directionality.[1,2] In the presence of an

electron withdrawing substituent, hydrogen interactions correlate very well with the

magnitude of the sigma hole, thus confirming the electrostatic driven nature of these

interactions.[10] Hydrogen bonding interactions with D and A as F, O and N are best

known,[11] but in the last few years, the concept has been extended to C-H⋯Y, where Y is

an electronegative atom and C-H⋯π type of interactions.[7,4,12–14] However, these latter two

types of interactions are mainly stabilized by dispersion and charge transfer

interactions,[15–18] which are much weaker than the former.[19,20] Though not a very common type of hydrogen bonding interaction, *ab initio* quantum calculations confirmed the C-H⋯O type of interaction to behave more like a conventional O-H⋯O type hydrogen bond.[21–23]

C-H⋯π interactions are believed to lie between the critical region of the weak hydrogen bond and the van der Waals interaction.[4] Nevertheless, the C-H⋯π type of hydrogen bonding although also relatively weak, can still be of relevance in biomolecular structures considering their widespread occurrence in nature. Earlier studies on C-H⋯π interactions on ethylene-methane clusters insisted on the major source of attraction being electrostatic and charge transfer interactions. However, recent high-level *ab initio* calculations on benzene-methane clusters and several other C-H⋯π analogues show the dominance of dispersion forces, with very minimum contribution from electrostatic interactions.[24,25] The preferred configuration is the one in which the aliphatic C-H bond of the methane is pointing towards the aromatic system as shown in Figure 1.1-1 below.[4] Studies have shown C-H⋯π interactions serve several functions in proteins, such as secondary structure stabilization, drug recognition and enzyme substrate binding at the active site.[3] Also, non-covalent hydrogen bonding interactions play a remarkable role in DNA base pairing, where hydrogen bonding is the dominant energy term whilst the non-specific π⋯π stacking originating from the dispersion effects is energetically less significant.[1]
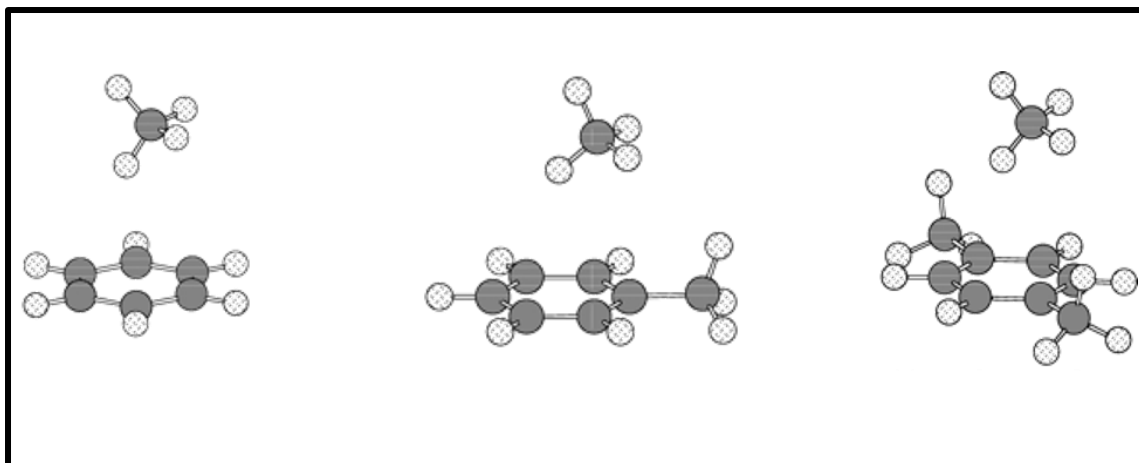
Figure 1.1-2: Methane clusters with benzene, toluene and *p*-xylene. Taken from ref. 4.

1.1.2 HALOGEN BONDING INTERACTIONS

Contrary to hydrogen bonding interactions, less is known about halogen bonding interactions, which involves a polarizable halogen atom acting as an electron *acceptor* due to the highly anisotropic electron density around the halogen nucleus. The general scheme involves: R-X$\cdots$Y where X can be Cl, Br, I, with F being inactive due to *sp* hybridization, R is covalently bound to X, and Y as a negative site such as a π cloud of an aromatic system or Lewis base. A region of positive electrostatic potential known as a "σ-hole" is found on the outer side of the halogen atom that is covalently bonded to the electron withdrawing residue.[9,10,26] It is through the σ-hole that the halogen interacts with the lone pair of a Lewis base or with the π cloud of an aromatic residue. This type of interaction is highly directional, as illustrated in Figure 1.1-2. Remarkably, hydrogen and halogen bonds have similar characteristics due to common electron donors.[9,10,26] Based on benchmarked computational data sets,[27] the two have comparable stabilization energies and thus, there is competition between the two interactions in solvent systems.

However, hydrogen bonds are stronger than halogen bonds involving Cl, but become comparable for X = Br and I.[26] Generally the interaction increases in strength in the order Cl < Br < I.[26,28,29] The existence and magnitude of σ-hole depends upon three factors: 1) the electron withdrawing power of the halogen, 2) the electron withdrawing power of the remainder of the molecule, and 3) the degree of *sp* hybridization of the *s* unshared electrons of the halogen. Halogen atoms are typically found at the periphery of molecules in organic compounds where they are ideally positioned to be involved in a wide range of intermolecular interactions, playing a key role in many chemical and biological processes. Recent studies have reported on the existence of short R-X⋯Y contacts in protein-ligand interactions with the most common binding interactions involving C-X⋯ π and C-X⋯O, with C-X⋯N to a lesser extent.[30–33] Hence utilizing a prototypical system involving anisole and a halomethane or dihalogen would be an ideal platform to explore and characterize the different kinds of possible interactions.
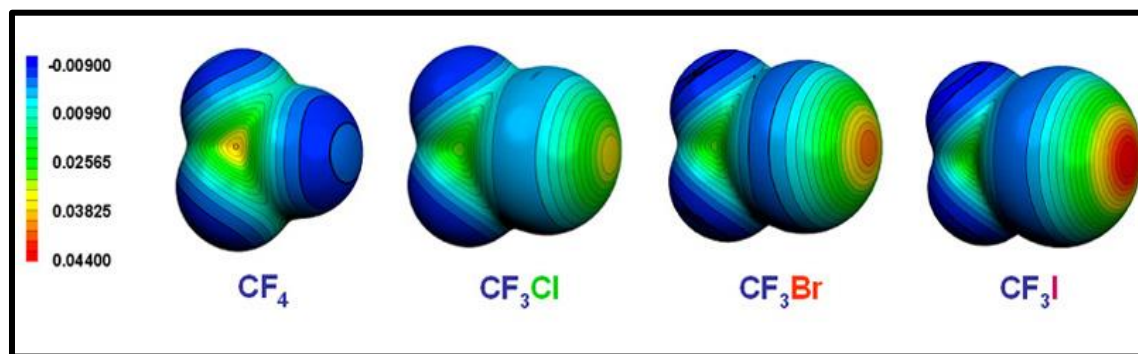
Figure 1.1-3: Electrostatic potential maps of CF_3X (X=F, Cl, Br, I) molecules viewed along the C-X bond. This figure illustrates the formation of the sigma-hole and the scale to the left indicates the potential in units of kcal/mol. Taken from ref. 34.

1.1.3 CHALCOGEN BONDING INTERACTIONS

Similar to halogen bonding interactions, chalcogen bonding is another type of a non-covalent interaction that involves a sigma hole and is less frequently known. This type of noncovalent interaction occurs between the positive electrostatic potential located on the surface of a chalcogen atom (O, S, Se, Te) covalently bonded on one fragment and a negative site on another or the same molecular entity.[35] The electron rich site can be a lone pair of electrons on a donor atom of a Lewis base, π electrons of a conjugated system or a chalcogen atom itself. In a similar way to hydrogen and halogen bonding, chalcogen non-covalent interactions are highly directional as illustrated in Figure 1.1-4. The strength of the chalcogen interaction depends on four factors: 1) the basicity of the electronegative site, 2) the nature of the chalcogen atom which generally increases in the order (Te > Se > O > S), 3) the polarizability of the chalcogen atom, and 4) the interaction angle, which should be close to 180° for strong interaction.[35] Complexes which undergo chalcogen bonding are stabilized by electrostatic (main attractive contribution), charge transfer and dispersion energy terms.[36] There has been a considerable interest in chalcogen noncovalent interactions in recent years, due to the fundamental role they play in diverse areas of science including catalysis,[37] molecular self-assembly,[38,39] drug design[40] and crystal engineering.[41,42] For example, sulfur is ubiquitous in nature, specifically in biologically active natural products where it affects molecular recognition mechanisms.[40]

Several studies have been conducted on chalcogen bonded complexes in the gas phase via rotational and vibrational spectroscopy in combination with theory. For

example, Godwin and Legon studied the rotational spectrum of the weakly bound dimer

of sulfur dioxide and hydrogen cyanide to understand the molecular structure and

binding. Analysis of the spectroscopic constants from the observed rotational spectrum of

the complex confirmed a ground state structure in which the HCN is perpendicular to the

plane of SO_2, with the N positioned close to the plane. The authors concluded that the

structure of the complex was out of plane, stabilized by a chalcogen bond formed

between S and N. The experimental result was in good agreement with molecular

electrostatic potential (MESP) calculations performed on HCN and SO_2, which showed

the most nucleophilic region of HCN (non-bonding pair on N) interacting with the

electrophilic region of SO_2 (σ-hole on S surface), resulting in a perpendicular geometry.

[43,44] In another study, Ford and Ramasami carried out an *ab initio* theoretical

investigation on sulfur bonded van der Waals complexes of carbon dioxide analogues

with common Lewis bases, XCS···Y, where X= (O, S, Se) and Y=(NH_3, H_2O, PH_3, H_2S).

The optimized ground state structures of complexes with NH_3, H_2O and PH_3 adopted a

linear configuration, while complexes comprised of H_2S were characterized by a

perpendicular geometry (XCS···S).[45]
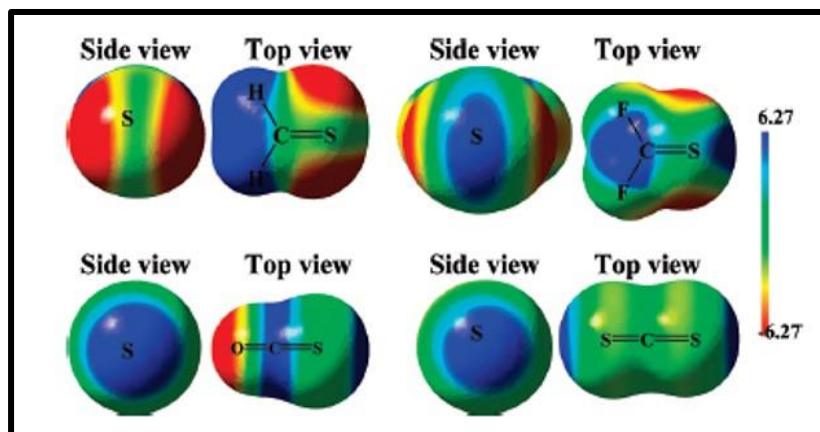
Figure 1.1-4: Electrostatic potential maps of H_2CS, F_2CS, OCS and SCS compounds viewed along the C=S bond computed at the MP2/aug-cc-pVTZ . This figure illustrates the formation of the sigma hole and the scale to the right shows the potential in units of kcal/mol. Taken from ref. 36.

1.1.4 Π-Π INTERACTIONS

Lastly, $\pi - \pi$ interactions are attractive non-covalent interactions that occur between aromatic rings, that impact fields such as chemistry, material science, and biochemistry.[46,47] The type of forces governing this type of interaction are electrostatic, van der Waals and dispersion forces. π - π interactions are fundamental to the understanding of many supramolecular organization and recognition processes,[48] playing a remarkable role in areas such as DNA supramolecular structure, intercalation of drugs into DNA, host-guest chemistry, crystal packing, alignment of liquid crystals, self-assembly of synthetic molecules and protein side chain interactions.[46,47,49–53]

Gas phase spectroscopic studies in combination with theoretical calculations have been conducted on prototypical aromatic π-stacked systems to understand the structure and bonding.[8,54,55,5] For the benzene dimer, three types of conformers have been identified, the sandwich, parallel displaced and the T-shaped (C-H···π) conformer, and

these are shown in Figure 1.1-5. High-level *ab initio* calculations predicted the T-shaped

and the parallel displaced structures to be the most stable and nearly isoenergetic.

However, only the T-shaped conformer contributed to the excitation spectrum[56] and the

stability was ascribed to quadrupole-quadrupole interactions,[57] which are repulsive for

parallel rings but stable for the T-shaped configuration.[58]
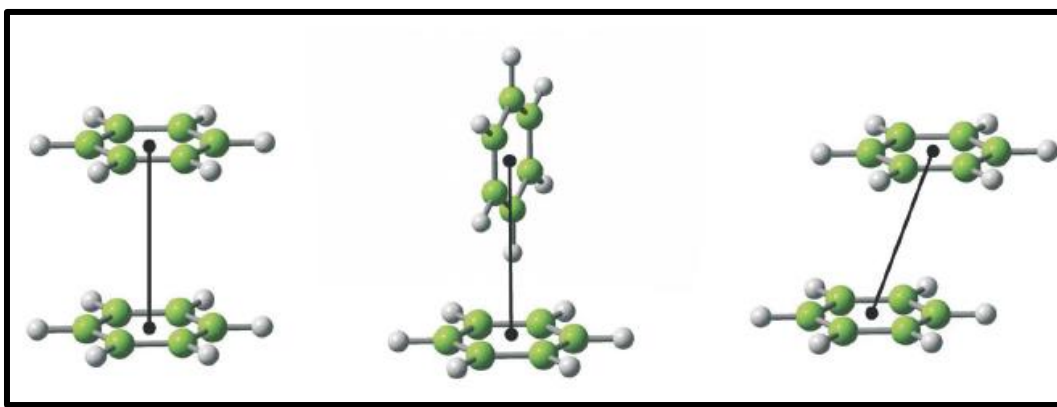
Figure 1.1-5: Types of noncovalent conformers of benzene van der Waals dimer. Taken from ref. 54.

The experimental outcome of solution and gas phase experiments on the toluene

dimer predicted the sandwich and the parallel displaced configurations to be more stable

than the T-shaped configuration. The preferred stacked configuration was stabilized by

dipole-dipole attractive interactions which overcame the repulsive quadruple-quadruple

interactions.[48]

In the context of understanding charge transfer processes in π stacked systems,

DNA and nucleobase oxidative damage, the Reid group reported on experimental

spectroscopic investigations of the fluorene dimer ($C_{13}H_{10}$) augmented with high-level *ab*

initio and DFT methods.[59] It was shown that the van der Waals dimer was π stacked in

ground (S_0), first excited (S_1) and cationic (D_0) states, with the vertical excitation from the ground state structure corresponding to a parallel orthogonal arrangement. In contrast, the global minimum on the S_1 and D_0 surfaces corresponded to a sandwich excimeric structure.[60] The sandwich, orthogonal and parallel displaced conformers are shown in Figure 1.1-6 below. To determine the binding energies of the dimer in all three (S_0, S_1, D_0) electronic states, the two-color appearance potential (2CAP) method was used. Later, these experiments were extended further to investigate the magnitude of the binding energies involved and the effect of methyl-substitution.[61,62] The dimethyl substituted system $(F1)_n$ mainly showed a hybrid configuration stabilized by both π-stacking and C-H$\cdots\pi$ interactions. The global minimum energy structure of the methylated dimer was a tilted non π stacked structure which was slightly more strongly bound than the π stacked fluorene dimer, evidencing the important role of C-H$\cdots\pi$ interactions in increasing the steric constraints restricting the cofacial approach, hampering the formation of sandwich type structures.[61]
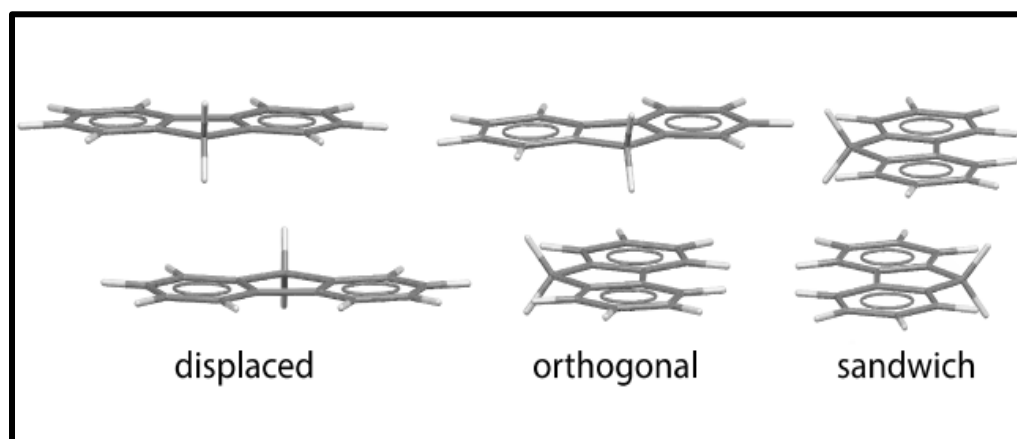
Figure 1.1-6: Types of noncovalent conformers of fluorene van der Waals dimer ($C_{13}H_{10}$). Taken from ref. 59.

1.2 EXPERIMENTAL BACKGROUND AND METHODOLOGIES

1.2.1 FORMATION OF JET COOLED MOLECULAR CLUSTERS

Non-covalent molecular clusters have previously been produced in a continuous or pulsed supersonic expansion beam. The species of interest is seeded in an inert buffer gas (He, Ar, Ne, etc.) and the resultant gaseous mixture is expanded from a region of high pressure to a region of relatively low pressure through a small orifice in a nozzle.[63] Expansion into vacuum leads to a conversion of random (3-D) translation motion into 1-D motion, giving a very dense and narrow velocity distribution of the expansion.[64] It is the width of this distribution which determines the translational temperature.[65–67] In seeded supersonic molecular beams, the species of interest is present as a small fraction of the monoatomic carrier gas. Collisions occurring during the initial stages of the expansion will accelerate the sample molecules to relatively the same speed as the buffer gas. With subsequent collisions, the internal degrees of freedom are cooled, into the lowest accessible rotational and vibrational quantum states.[68] This greatly reduced spectral congestion and leads to simplification of the spectrum; rotational temperatures <10K are common even for relatively large systems, while vibrations are cooled less efficiently but can reach temperatures <100K.[66]

In the high pressure region of the expansion, three-body collisions can lead to formation of weakly bound clusters. Here, cluster formation occurs in the presence of a third body which is generally another inert carrier gas atom. The carrier gas is responsible for absorbing away the excess energy contained in the moderately greater degrees of freedom of the cluster. Atoms do not possess vibrational or rotational degrees of freedom

and as a result the inert gas is scattered away at an increased momentum.[69] The large number of collisions occurring during the first stages of the expansion not only cool the expansion mixture but can also lead to the production of large concentrations of small and large clusters via the three-body collision process.

Various parameters of the expansion can affect the clustering size distributions and these include, nozzle diameter, mixing ratio and the temperature of the buffer gas.[70] At high backing pressure a distribution of the clusters forms in the expansion including dimers, trimers and other high order clusters.[63] However, this problem can be solved by operating at very low seed ratios, favoring smaller cluster sizes, and using Resonant two-photon ionization with the time of flight mass spectrometric analysis (R2PI-TOFMS) to selectively interrogate the spectra of mass-selected species. The experiments used here combine supersonic jet cooling with R2PI methods and TOF mass spectroscopy.

1.2.2 RESONANCE ENHANCED MULTIPHOTON IONIZATION (REMPI-TOF)

Resonance enhanced two photon ionization (R2PI) combined with mass spectroscopic methods have been employed to determine the excitation spectrum of molecules and weakly bound clusters. The R2PI method involves the absorption of a resonant photon by the species of interest to an electronically excited intermediate state. Absorption of a second photon achieves ionization. Several variants of this method are possible. One-color Resonant Two Photon Ionization (1C-R2PI or R2PI) involves excitation and ionization photons of the same frequency, which often come from the same laser system.[71] Alternatively, if the excitation and ionization photons have different

frequencies, the scheme is known as Two-Color Resonant Two Photon Ionization

(2CR2PI). The difference between the two schemes is clearly illustrated in Figure 1.1-7.

The 2CR2PI method provides information which is not readily attainable through 1C-

R2PI.
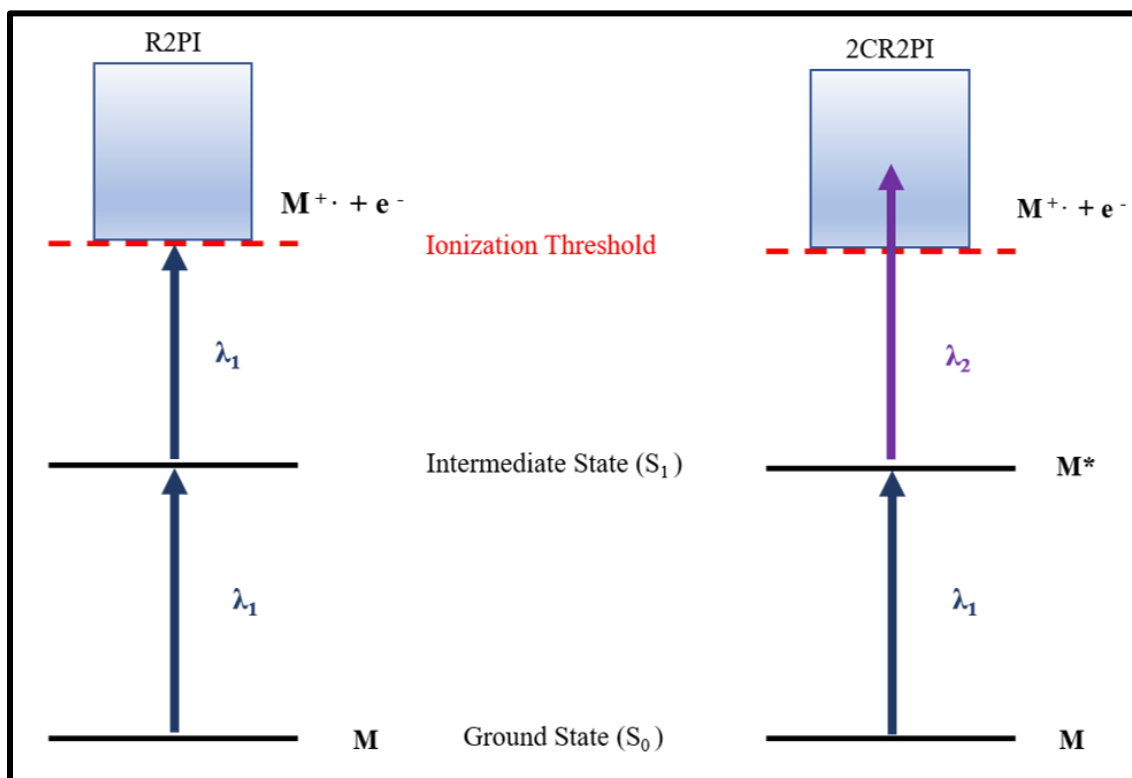
Figure 1.1-7: Schematic representation of the energy level diagram of R2PI (left) and 2CR2PI (right).

Two types of experiments are common in 2CR2PI experiments. If the ionizing

photon is fixed and the excitation photon is scanned, an electronic spectrum of the

species of interest (i.e., S_0-S_1 spectrum) is obtained. If instead the excitation wavelength

is fixed and the ionization wavelength scanned, then an ion-yield (IY) spectrum is

obtained, which can be used to derive the ionization threshold.

1.2.3 EXPERIMENTAL CONFIGURATION FOR REMPI-TOF MASS SPECTROMETRY

The experimental set up is similar to that described from the previous work done in the Reid lab.[7,8,72,73] Three types of experiments were conducted namely, 2CR2PI, Ion yield and 2-Color Appearance Potential (2CAP), yielding the excitation spectrum, ionization potential and binding energy respectively.

For the experiments discussed in Chapter 2 and 3, the excitation laser consisted of a dye laser (Lambda Physik Scanmate 2E) pumped with the third harmonic of a Quantel Q-Smart 850 Nd:YAG laser and operated typically with Coumarin 540A dye. The output of the dye laser was frequency doubled by incorporating a barium borate crystal (BBO-1), giving a tunable wavelength range of 261 to 293 nm and an energy of 0.5 to 0.9 mJ/pulse. The excitation laser beam path is pictured in Figure1.1-8.
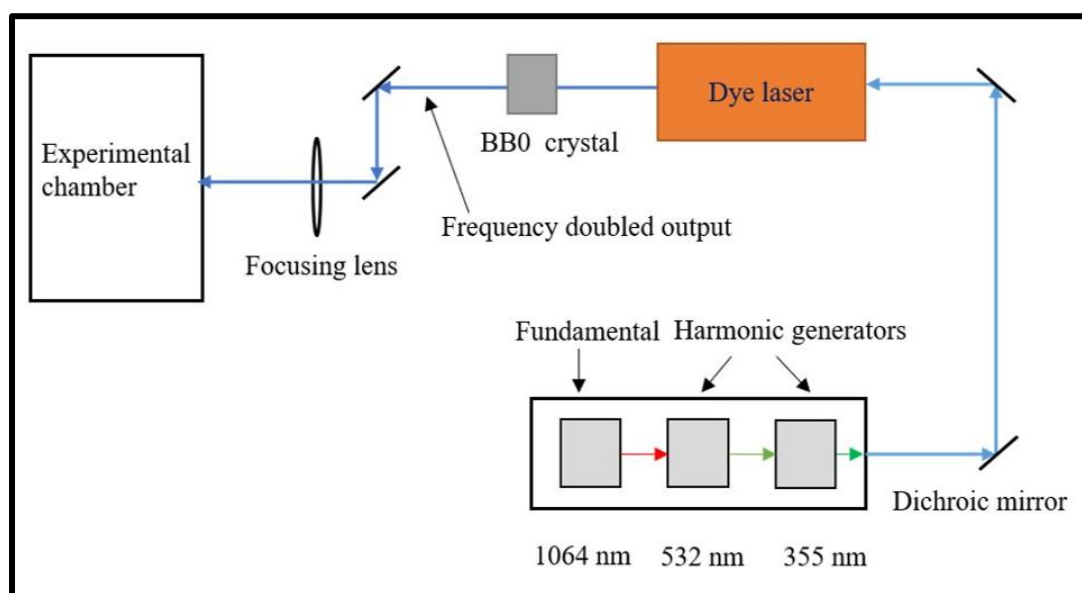
Figure 1.1-8: Schematic representation of the experimental set up of the laser beam path into the TOF chamber.

The ionizing laser consisted of a second frequency doubled dye laser (Sirah Cobra-Stretch), pumped with the second harmonic (532 nm) of the Spectra-Physics INDI Nd:YAG laser and operated with a combination of two red dyes (DCM and Pyridine 1), giving a frequency doubled lasing range of 318 to 348 nm, at ~1mJ/pulse. Red dyes are inefficient absorbers of the 355 nm pump radiation, and thus for these experiments a pump wavelength of 532 nm was employed. The output from both laser systems was overlapped temporally and loosely focused into the extraction region of the main chamber via (1.0 or 2.0 m respectively) plano-convex focusing lenses and intersected with the supersonic molecular beam in a mutually perpendicular geometry. Temporal control of the experiment e.g. delay between nozzle opening and laser interrogation and hence the time delay between the two lasers was controlled by an 8-channel digital pulse/delay generator (Berkeley Nucleonics 565).

Ion yield (IY) spectra measurements were conducted to determine the ionization potentials (IP) for the monomer and cluster. Here, as described above, the excitation laser wavelength (λ_1) was tuned on resonance with the species of interest, and the ionization laser wavelength (λ_2) was scanned through the ionization threshold. The time delay between the excitation and ionization laser (dissociation) was set at 5 ns and the power of the excitation laser was attenuated with a polarizer such that no one color signal was observed.

Two-color appearance (2CAP) measurements were obtained in a similar way, but by monitoring the monomer mass channel while scanning the wavelength of second photon (λ_2) above the cluster IP, with the first photon (λ_1) fixed on resonance with the cluster. For total photon energies (E) larger than the cluster binding energy (BE), the

monomer cation will appear from the cluster breaking. The 2CAP method sets up an upper limit to the ground state binding energy, as we do not account for field ionization effects in our measurements. This can ultimately affect the onset and shape of the IP curve. The schematic of the REMPI-TOF overall experimental set up is shown in Figure 1.1-9.

In studies of the anisole-methane complexes, a free jet molecular beam expansion was formed by flowing a premix of 10 % methane in inert Ar carrier gas, at backing pressures ranging between 40 to 80 psi, through a bubbler containing liquid anisole (Sigma Aldrich, 99 % purity). The stainless-steel bubbler was placed in a refrigerated bath maintained at –5 °C, to control the concentration of anisole in the molecular beam. The gas mixture was then expanded into the source chamber via a 0.8 mm diameter opening in the cap of a pulsed nozzle (General Valve series 9, 10 Hz, with an opening duration time of 220 µs). The gas pulse passed into the main chamber via a 1.5 mm diameter nickel skimmer. The critical alignment of the skimmer and the nozzle allowed for the central, coldest, and most stable part of the supersonic expansion (according to gas dynamical properties) which has the highest concentration of clusters to be spatially filtered by the skimmer before entering the time-of-flight tube.
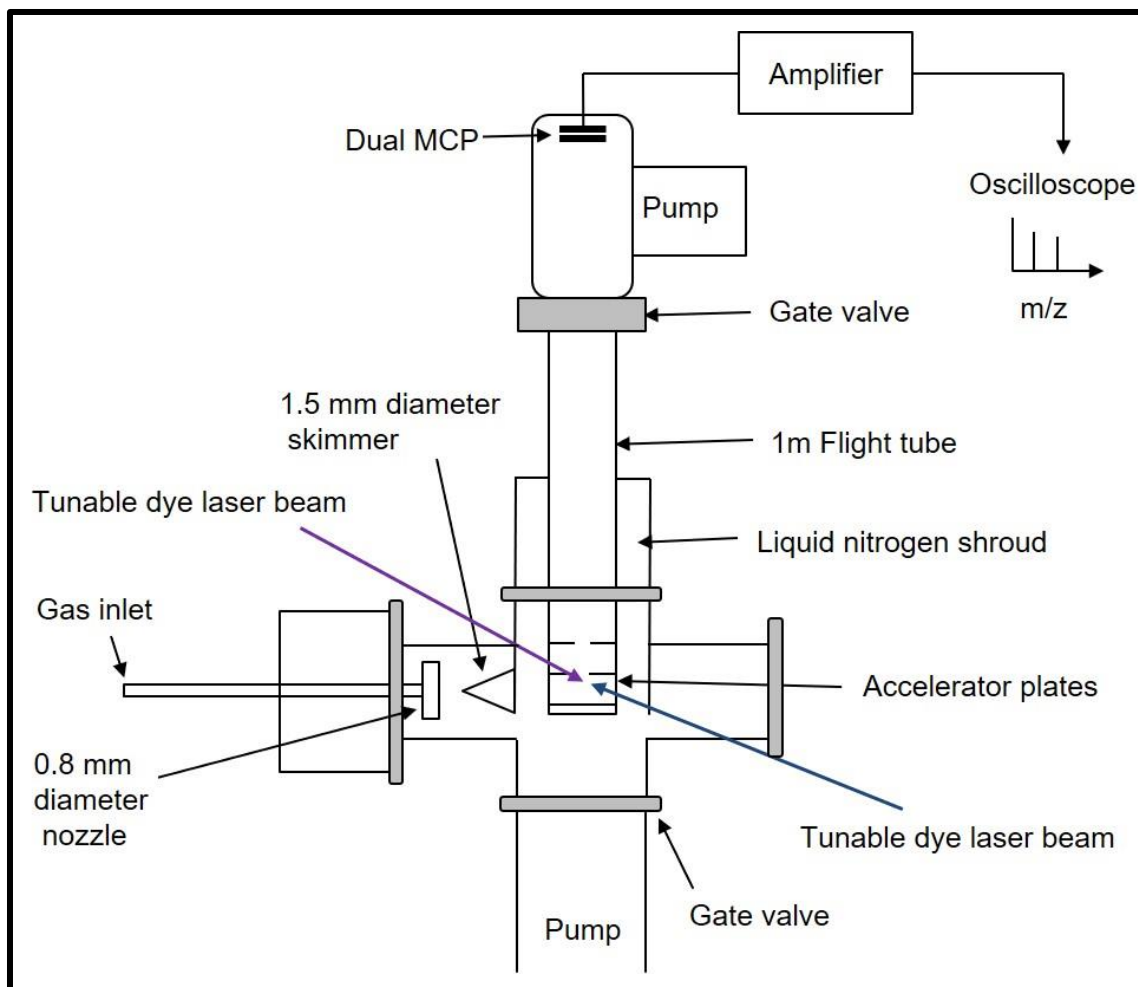
Figure 1.1-9: Schematic representation of the Resonant Ionization-TOF experimental setup.

The skimmer is also responsible for reducing the molecular flow into the ionization region, keeping the background pressure in the flight tube low. This is not only desirable for the optimum operation of the vacuum pump but also ensures that there is a collisional free passage from the skimmer to the detector. This is crucial for obtaining maximum signal intensity, which is also achieved by with varying the nozzle-skimmer distance (mechanically moving the nozzle back and forth). In the main chamber, the molecular beam transmitted through the skimmer is crossed perpendicularly by the two co-propagating pulsed laser beams at the point of interaction between the repeller and the

extractor electrodes. A three-plate electrode stack was employed, with the repeller, extractor and ground plate typically held at +2200 V, +1950 V and 0 V respectively. The ions produced leave the ionization region and enter the acceleration region where they quickly reach the field-free drift region. The ions traverse a path of one meter before striking the dual micro-channel plate (MCP) (detector). The detector signal was amplified 25 times by a fast preamplifier (Stanford Research SRS445A) and displayed on a digital oscilloscope (Tektronix TBS 1042) that is in turn interfaced to a personal computer controlled by a LABVIEW program. This program was used for the data acquisition and stepping of the laser during scans, with typical step size of 0.01 nm for survey scans and 0.002 nm for finer scans.

The source/main chamber was evacuated by a water baffled diffusion pump (Varian VHS-4) backed with a rotary vane pump (Edwards E2M18). The flight tube was kept under vacuum by a 250 L/s turbo-molecular pump (Varian Turbo V250) backed with a rotary vane pump (Varian DS 102), with a gate valve that isolated the detector which was always under vacuum. The typical working pressures obtained when the nozzle was in operation were $\sim 1\text{-}4 \times 10^{-5}$ mbar in the source chamber and $\sim 1\text{-}3 \times 10^{-6}$ mbar in the flight tube. At times the background pressure in the flight tube was reduced further by cooling the vacuum shroud with liquid nitrogen. Shrouding the flight tube with liquid nitrogen could reduce the background noise caused by the back streaming of condensable vapors from background species such as those used previously in the experiment and oil, however this step was skipped for the experiments reported herein.

1.2.4 VELOCITY MAPPED ION IMAGING (VMI) TECHNIQUE

Following from the seminal work conducted by Chandler and Houston on the ion imaging technique,[74] and from Eppink and Parker in developing an improved Velocity Mapped Ion Imaging (VMI) lens configuration,[75] the VMI technique has developed as a powerful tool for the study of photodissociation processes. The VMI technique has advanced to a point where it is becoming equivalent or more superior than the conventional methods in terms of efficiency and energy resolution.[76] In recent studies, the VMI technique has been used to determine the binding energy (BE) of weakly bound clusters in the cationic radical state (D_0) and these include the dimers of anisole, benzene, water, ammonia, molecular oxygen and iodine.[77,78,79,80,75,76] The Reisler group focused on several experiments where they measured the binding interactions of prototypical hydrogen bonded model complexes using this technique.[79–82] Other weakly bound van der Waals clusters studied include benzene and pyrazine aromatics with argon.[83,78]

The Lawrance group at Finders have also reported on a variety of van der Waals clusters using VMI in conjunction with REMPI. The group carried out studies on clusters of benzene with acetylene and argon (including high order clusters) to investigate the cluster size responsible for spectral features and their binding interactions in the D_0 state.[78,84,85] Using a similar approach, they reported studies on clusters of *p*-difluorobenzene with argon,[86–88] and studies of van der Waals clusters of NO with rare gases (He, Ne and Ar) and CH_4 as simple prototypes for investigating dispersion interactions.[89,90,91]

Under the proper focusing conditions, charged particles formed in the ionization volume at different initial positions but with the same velocity vector are focused on to the same spot on the VMI detector screen as illustrated in Figure 1.2-1. Thus, the method produces two-dimensional (2D) circular images from a three-dimensional (3D) charged particle (electrons or ions) distribution. The radial extent of the image is directly proportional to the velocity of the ions and is always perpendicular to the time of flight direction.[76] The intensity distribution around the outer edge of the images is indicative of the angular distribution. In contrast to conventional methods, the significance of the method is illustrated in the ability to characterize the full 3D velocity distribution. This offers the method the multiplexing advantage of detecting all the velocities of the charged particles in a single image, thus all the necessary information is extracted (kinetic energy and angular distributions).[75]
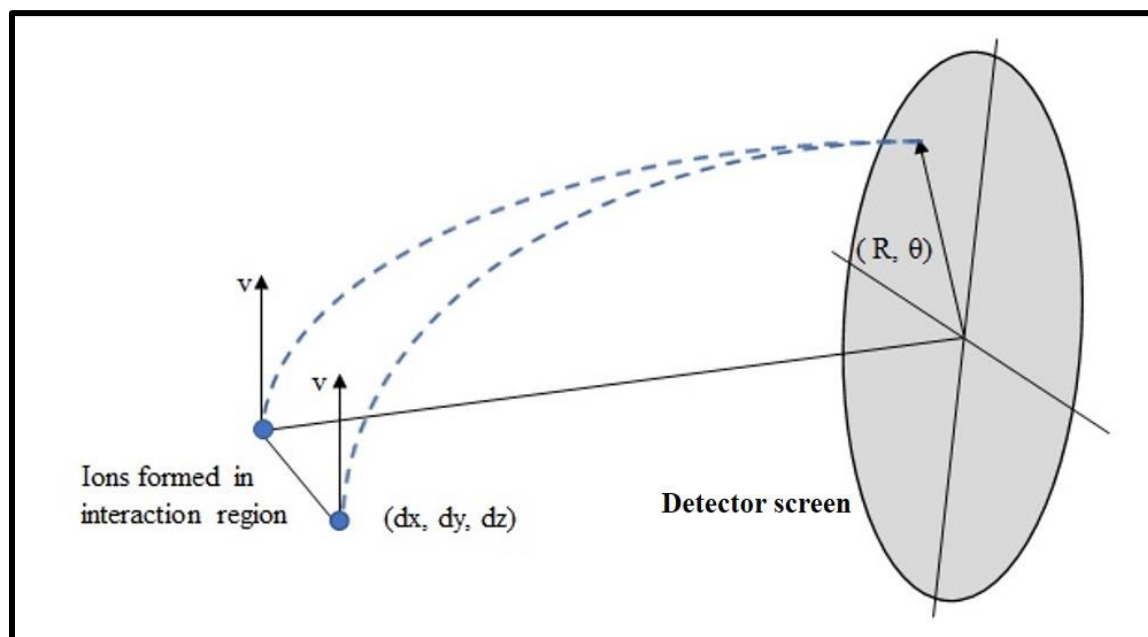
Figure 1.2-1: Schematic representation of the VMI lens system focusing two ions formed at different locations in the interaction region with the same velocity vector to the same point on the detector screen.

In the VMI technique applied to examine the binding energy of clusters, a two-color excitation scheme is normally employed, similar to that used in the IY and 2CAP measurements described above. First, a laser pulse tuned to cluster resonant frequency selectively excites the cluster from the ground vibrational state (S_0) to a vibrational level within the excited sate (S_1) below the dissociation threshold. A second laser pulse further excites the cluster from the S_1 state to the ground cationic radical state (D_0), with total energy above the cluster ion dissociation energy. Cations are thus produced with vibrational energies in excess of the cluster dissociation energy in a range of vibrational states with populations governed by the Frank Condon factors of the transitions from the S_1 state to the D_0 state. The cluster subsequently dissociates into two monomeric fragments, a cationic and neutral fragment respectively. The observed maximum kinetic energy (KE_{max}) release corresponds to the production of the two fragments with zero internal energies and zero kinetic energy for the ejected electron. Based on these assumptions, the binding energy in the D_0 state can be determined following equation (1), which represents the conservation of energy in the photodissociation process.

$$KE_{max} = E^{\dagger} = E_{photon} - BE(D_0) \qquad (1)$$

In equation (1), KE_{max} is the total translational energy available in the system, E_{photon} is the total energy of the excitation (λ_1) and ionizing (λ_2) photons, and BE is the binding energy of the cluster in the D_0 state. It is apparent that the observed KE_{max} is directly proportional to E_{photon}. This method sets up an upper limit to the binding energy because signal to noise ratio (S/N) limitations may result in an observed KE_{max} smaller than expected. In contrast, space charge effects due to the long path length employed can lead

to image blurring which may result in a KE_{max} larger than expected. To minimize of this effect, the number of ions per laser shot was minimized during image acquisition. Another limiting factor is that the kinetic energy distribution of the departing electron is not known.

1.2.5 VMI EXPERIMENTAL SET UP

The velocity ion imaging experiments were carried out on a newly built spectrometer in the Reid lab. The spectrometer utilizes a molecular beam source identical to the one used in REMPI-TOF. The overall experimental set up of the VMI is shown in Figure 1.2-2. The source chamber was differentially pumped by a 6-inch diffusion pump (VHS-6) and the base pressure in the source region was typically 10^{-6}, which rose to 10^{-5} torr when the pulsed nozzle was in operation. The molecular beam was expanded by the nozzle into the ionization region by passing through a 1.5 mm diameter conical nickel skimmer (Beam Dynamics). The molecular beam, once in the interaction chamber, enters the ion optic assembly of the VMI.

The ion optic assembly consisted of eleven 100 mm diameter, 1.5 mm thick polished stainless-steel electrodes and was housed in a large cylindrical chamber that was pumped by an 8-inch turbomolecular pump. The first five electrodes were separated by ceramic spacers of dimensions, 6.35 mmm diameter and 20 mm length. The remaining electrodes were separated by spacers of the same diameter but different length (25 mm). The electrode stacking was then mounted on a base plate (mounting plate) of dimensions (200 mm diameter, 2.0 mm thickness). The electrodes and the base plate had apertures of

diameter, 5 mm on the mounting plate and the first electrode (repeller), with the second

(extractor) and the rest of the electrodes being 25, 25, 40, 40, 40, 40, 40, 40, 40 and 40

mm respectively. The overall ion optic assembly is illustrated as an expanded view on the

inset in Figure 1.2-2. To minimize space charge effects, the electrodes were coated with a

thin layer of colloidal graphite (AERODAG) prior to installation.
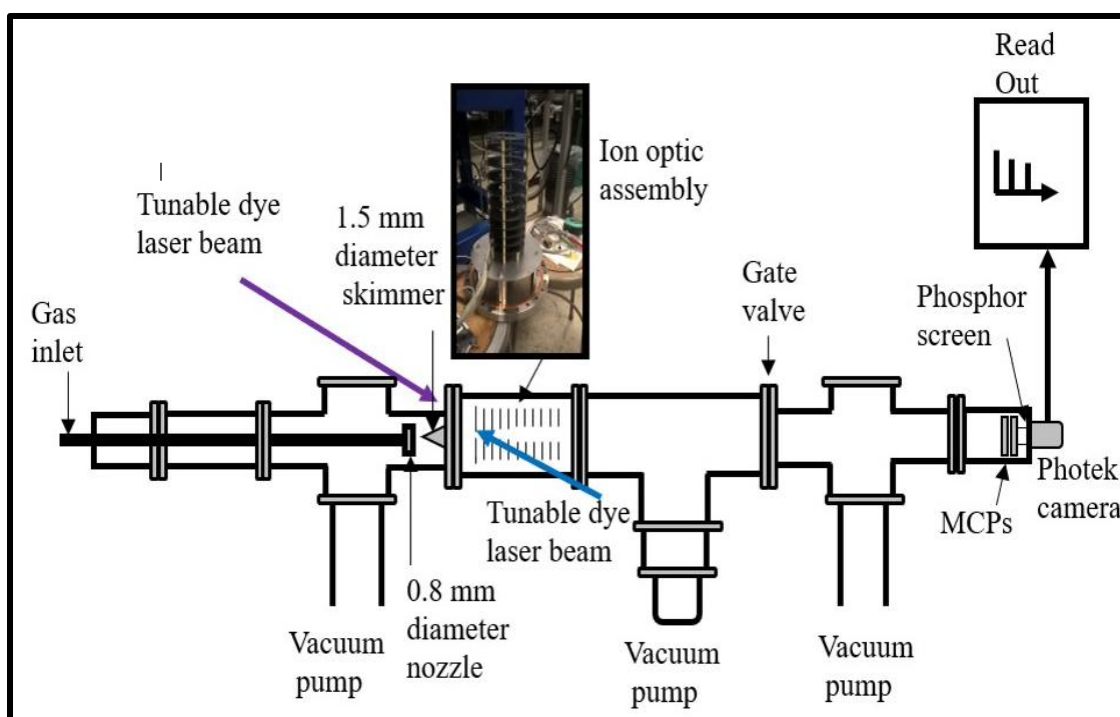
Figure 1.2-2: Schematic representation of the VMI experimental set up, the insert is showing the photographed image of the lens assembly.

The pump (λ_1) and probe (λ_2) lasers were overlapped in time and in space and

counter-propagated, intercepting the supersonic molecular beam at right angles at a point

150 mm downstream of the nickel skimmer orifice, between the first (repeller, V_R) and

second (extractor V_E) electrode. A critical parameter for achieving good velocity

focusing (good image resolution) depends on the ratio of the voltages (V_E/V_R) applied to

the electrodes. The new VMI design was based on a three-plate lens configuration, where the V_R and V_E electrodes were biased at 2000 V and ~1380 V respectively, with the third and successive electrodes grounded, and extended out along the flight tube to shield the ion trajectory from stray fringe fields. To establish the validity of our approach ion trajectory simulations were conducted prior to experimentation to obtain optimum conditions for the VMI configuration using the SIMION 8.1 charged particle optics simulation program. With the repeller voltage set, measurements for a range of extractor voltages were conducted to establish the voltage ratio for best imaging resolution. The voltages for the electrodes were tuned precisely in ±1 V increments by high voltage power supplies (Stanford Research Systems PS325) to obtain the desired velocity mapping conditions.

The expanding ion sphere produced by the electric field in the extraction region is subsequently mapped coaxially onto a two-dimensional microchannel plate detector coupled to a phosphor screen. The detection system was housed in a separate chamber pumped by a 6-inch turbomolecular pump and a gate valve was used to isolate the detection system from the main flight tube. The background pressure in this region was typically 10^{-8}, which rose to 10^{-7} torr when the nozzle was in operation. The detection system comprised of a VID275 camera with a dual 75 mm diameter chevron microchannel plate (MCP) configuration interfaced with an image intensifier and IDS U13060 camera. A (Photek) triple output digital high voltage power supply was used to supply the voltages to the detection system. The input voltage for the MCP was grounded with the front and rear MCP voltages typically set at 850 and 1700 V respectively. The phosphor screen voltage was typically set at 5000 V, and during image acquisition, the

rear MCP was reduced by 500 V and a variable gate pulse of +500 V amplitude was AC connected to the rear MCP using a separate gate unit.

In order to extract quantitative information from the observed images, it is necessary to determine the magnification factor of the lens assembly, which is based upon the expansion velocity and the time of flight. The magnification factor is a function of the position of focus along the flight tube and electrode settings, and could be estimated from the SIMION simulations.[84,75] The images were calibrated and experimental magnification factor derived by measuring the binding energy of a cluster system that has been precisely determined, in this case the anisole···Ar complex.[92] An instrument magnification factor of 1.3 was established from these experiments, which agreed well with that estimated from SIMION simulations.

In principle, the images are circularly symmetric and represents a three-dimensional velocity distribution projected onto a two-dimensional detector. To reconstruct the 3D data from the 2D plot, a mathematical conversion was carried out using an inverse Abel transformation and this was performed on a pBASEX algorithm[93] on a LABVIEW coded program. This way, the raw image data was converted from velocity space to kinetic energy space. A plot of probability of energy P(E) vs radial distribution in pixels was obtained and the pixel count was further calibrated to a kinetic energy scale.

1.3 THEORETICAL METHODS

This section covers the background on some of the Theoretical Methods used for comparison with the experimental findings.

1.3.1 DENSITY FUNCTIONAL THEORY METHODS

Density Functional Theory (DFT) is a computational method that describes properties of an interacting system of atoms, nuclei or electrons based on electron density of the system. The ground state properties predicted include molecular geometries, total energies, vibrational frequencies and ionization energies.[94] When compared to conventional quantum chemistry methods such as the Hartree-Fock (HF) and post-HF, DFT does not rely on a mathematical construct, the wavefunction which is not a physical observable, but rather on the physical characteristic of the system. The electron density is a function with three variables, the x-, y-, and z- positions of electrons and as a result its determination is independent of the number of electrons. Contrary to this, the wavefunction methods becomes significantly more complicated with increasing number of electrons. DFT methods are appealing as they provide approximations for exchange correlation potentials, exchange interactions and exchange correlation energy functionals. DFT methods have a significant improvement in computational accuracy without a further increase in computational time. However, the methods suffer from one major drawback in that, prior to choosing an appropriate method for a task, one must consult the literature. DFT methods can be classified into three categories, local density approximation (LDA) which assumes a uniform density throughout the molecule,

typically not a very popular method and, gradient corrected (GC) methods which accounts for the inhomogeneity of electron density, and hybrid methods which are a combination of *ab initio* methods (HF) and improved DFT mathematics (B3PW91, B3LYP, M06, M06-2X and CAM-B3LYP). Some DFT methods are designed for a specific application, Zhao and coworkers developed a hybrid M06-2X which performed very well in describing non-covalent interaction energies.[95] The Rathore group established the B1LYP40 functional with 40% HF contribution as a method of choice for predicting charge stabilization/delocalization for π conjugated systems in the cation radical state.[90-92]

1.3.2 COUNTERPOISE CORRECTION AND BASIS SET SUPERPOSITON ERROR

In calculations of non-covalent interactions such as in weakly bound clusters, there can be an artificial shortening of intermolecular distances leading to an artificial strengthening of the intermolecular interaction. This occurs when one monomer in a dimer utilizes the basis functions from another monomer to describe its electron distribution and vice versa, lowering the energy of the dimer in a way that is not possible for the isolated monomers, leading to an overestimation in the binding strength of the complex.[27] This effect is more pronounced for smaller basis sets, and the inconsistent treatment for the basis set for each respective monomer as the intermolecular distance is varied is referred to basis set superposition error (BSSE). The famous Boys-Bernardi counterpoise correction is employed for removing BSSE when studying intermolecular

interactions in weakly bound clusters.[96] The uncorrected interaction energy between monomers A and B is determined by equation 2.

$$\Delta E_{int}(AB) = E_{AB}(AB) - E_A(A) - E_B(B) \qquad (2)$$

In equation (2), the subscripts denote the basis and geometry used, and the symbol in parentheses denotes the chemical system considered. E_{AB} represents the interaction energy of the cluster evaluated at the cluster basis (union of the basis sets on A and B). Likewise, monomers A and B are also evaluated separately at their own basis sets. The counterpoise correction is performed as three separate standard computations which considers the calculated equilibrium geometries of the respective monomers and cluster in doing the calculation. Equation 2 can be corrected by estimating the amount by which monomer A is artificially stabilized by the extra basis functions from B and vice versa as shown in equations (3) and (4).[97]

$$E_{BSSE}(A) = E_{AB}(A) - E_A(A) \qquad (3)$$

$$E_{BSSE}(B) = E_{AB}(B) - E_B(B) \qquad (4)$$

With the assumption that there is no change in geometry as monomers A and B approach each other, it is expected that the energy of the respective monomers be lower in the dimer basis than in the monomer basis ($E_{AB}(A) < E_A(A)$ and thus $E_{BSSE}(A) < 0$). Subtracting the error from the interaction energy defined in equation (2), the terms $E_A(A)$ and $E_B(B)$ cancel out resulting in a counterpoise corrected interaction energy (ΔE_{CP}) represented by equation 5.

$$\Delta E_{CP}(AB) = E_{AB}(AB) - E_{AB}(A) - E_{AB}(B) \qquad (5)$$

CHAPTER 2: ANISOLE-CH$_4$ 1:1 VAN DER WAALS CLUSTER

2.1 BACKGROUND ON ANISOLE AND PREVIOUS STUDIES OF ANISOLE VAN DER WAALS CLUSTERS WITH ATOMS AND MOLECULES

Methoxybenzene or anisole is pictured in Figure 2.1-1. Due to its structure anisole possesses two sites that can act as proton acceptors, the electron lone pair on oxygen and its aromatic electron system[98], in addition to the possibility of secondary in-plane interactions.[99] Anisole is a prototypical molecule of strong relevance for studying different intermolecular interactions as evident by the reported studies on the formation and characterization of molecular complexes with simple systems like CO_2, NH_3, H_2O, BF_3, Ar.[92,100–102] and anisole dimer.[77,103,104] The gas phase absorption spectrum of anisole and the deuterated anisole was first measured at room temperature by Balfour,[105] who assigned some of the fundamental vibrations in the S_1 state. The excited state is known to exhibit longer lifetimes compared to benzene and other monosubstituted benzenes due to the oxygen donor class on anisole, making it readily ionized via R2PI.[106]

The anisole jet cooled excitation spectrum was also characterized by Bamgartel *et al*, who reported on both allowed and forbidden transitions in the rich vibronic structure in an energy range of up to 1600 cm^{-1} above the electronic origin.[107] The forbidden transitions were evidenced by comparably weak vibrational modes of the aromatic ring, particularly the 18b and 6b modes. The excitation spectrum showed similarities in vibrational structure with benzene and other monosubstituted derivatives such as phenol, chlorobenzene and fluorobenzene, and this was ascribed to the fact that the geometrical changes upon electronic excitation were similar in this series of molecules.

To further gain insights into the ionic properties of anisole, the adiabatic

ionization potential (IP) was measured by Tzeng *et al* using high resolution mass

analyzed threshold ionization (MATI)[108] and previously by other investigators.[109,110] The

observed IP value (8.232 eV) was lower than that of benzene and this was attributed to

the effect of the substituent on the transition energy and molecular vibrations. The

interaction between the substituent and the ring is stronger in the cation (D_0) than in the

neutral (S_0) state, causing a red shift in IE despite the properties of the substituent.[108]
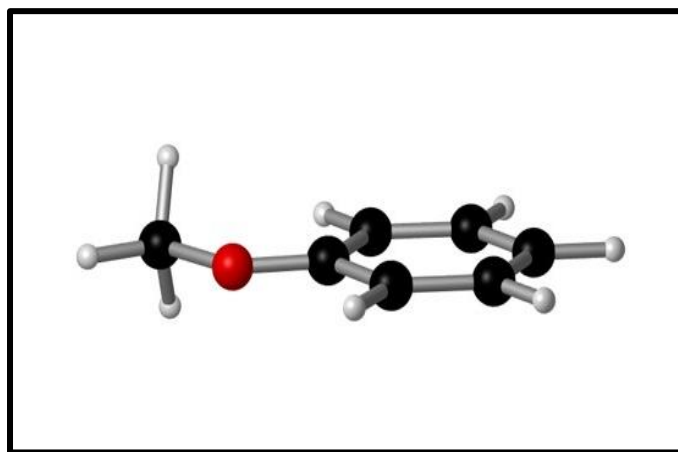
Figure 2.1-1: Optimized structure of methoxy benzene obtained at the CAM-B3LYP/6-311++g(3df,3pd) level.

Considering van der Waals complexes of anisole, with the two primary sites

acting as proton acceptors, it was observed that small molecules such as water and

ammonia would be slightly shifted from the center of the ring system in the direction of

the oxygen substituent upon moving from benzene-water[111] to anisole-water[112,113] or

anisole-ammonia.[114] Currently most of the examples of anisole van der Waals clusters

reported in literature involve two moieties interacting through hydrogen bonding,

dispersion or strong dipolar interactions. Hydrogen bonding interactions are characterized by specific functional groups (N-H, O-H) or with the π electron system of the aromatic ring. In the case of the rare gases, the rare gas atom is centered above the anisole aromatic ring system and the complex is stabilized by dispersion forces and through π bonding interactions.[103] The anisole-argon complex has been extensively analyzed and is red shifted with respect to the anisole monomer origin by -38 cm^{-1}.[84,109,92] The binding energies in the ground (S_0), excited (S_1) and cation radical state (D_0) were also determined and increase in the order: $S_0 < S_1 < D_0$.

A few studies on clusters of anisole other than with Ar also exist in literature.[84,115] The excitation spectrum of the anisole dimer was initially analyzed by REMPI and high resolution LIF spectroscopy.[116] The dimer origin was red shifted by -218 cm^{-1} with respect to the monomer origin, and DFT/TD-DFT methods confirmed a parallel displaced optimized geometry with two symmetric C-H-π and limited π-π superimposition.[104] Following from these studies, Becucci and coworkers reported for the first time on the direct measurement of the binding energies of the dimer in the S_0, S_1 and D_0 state using the VMI technique.[77] The VMI results severely overestimated the previous DFT binding energy calculations and the discrepancy was attributed to the fact that the dissociation produced one of the products in an excited vibrational state. Very recently, Hobza and coworkers accurately determined the binding energies using the 2CAP technique in combination with CCSD(T)/CBS and DFT-D3 methods.[103]

Brutschy *et* al,[101,113] carried out both experimental and theoretical investigations on anisole-water 1:1 complex and observed that the structure was planar, stabilized by hydrogen bonding between the water molecule (proton donor) and the methoxy

substituent (proton acceptor). One hydrogen of the water molecule points towards the lone pair of the methoxy substituent on anisole, with the second hydrogen from water interacting with the π system of anisole. Experimental spectra of the anisole-water 1:1 cluster found a blue shift of -124 cm^{-1} in the complex origin with respect to the monomer origin, indicating that the cluster was destabilized in the excited state. It was suggested that, upon electronic excitation, the hydrogen bond becomes weaker as the electron density is donated from the anisole oxygen to the ring system.[107] The anisole-methanol cluster origin was also reported to be blue shifted with respect to the isolated monomer origin, and theoretical calculations predicted the π interactions to be less favorable to occur than the in plane interactions by at least 1 kJ/mol.[117]

The anisole-carbon dioxide[118] 1:1 complex is also characterized by an in-plane binding geometry. Here, the most stable equilibrium geometry has the carbon dioxide molecule positioned in plane of the anisole ring, adjacent to the methoxy substituent. The origin band is blue shifted by -117 cm^{-1} from the corresponding anisole monomer origin, again indicating a destabilization of the complex in the excited electron state. In the case of the anisole-ammonia 1:1 complex, a non-planar configuration was found, in which the ammonia was located above the anisole ring system and displaced towards the methoxy substituent. Here, one hydrogen of ammonia interacts with the π cloud of the ring and a second hydrogen from the methoxy group interacts with the lone pair of electrons localized on the nitrogen. The S_0-S_1 transition energy was redshifted by -250 cm^{-1} from the anisole origin, indicating that the intramolecular interactions become stronger upon electronic excitation.[98,114]

Very recently, the anisole-toluene cluster was investigated by Thurn and Grotemeyer,[119] who observed a broad, largely unresolved spectrum of the complex, which was redshifted by -275 cm^{-1} with respect to the anisole origin and by -1395 cm^{-1} from the toluene origin. The broadness in the spectrum was attributed to the existence of 3 isomers that differed in their relative orientation, and to the presence of unresolved vibrational structure in Frank-Condon active modes. In another experiment, the anisole-phenol cluster was investigated, and the origin band was again redshifted with respect to band origins of both monomers (-387 cm^{-1} for anisole and -351 cm^{-1} for phenol).[48]

Motivated by the unique experimental platform offered by anisole with dual binding sites to a hydrocarbon featuring C-H···O and C-H···π interactions, which can act in concert or competition, here we seek to examine the spectra and binding energy of the anisole-methane complex. Specifically, we wish to observe how the geometry and C-H···π binding characteristics can be influenced by the methoxy substituent in comparison to the well-studied clusters of methane with benzene, indole, phenol, and toluene.[126,122] With this in mind, the anisole-methane cluster is studied experimentally to obtain primary information on the nature of the dispersion forces, equilibrium geometry and interaction energies augmented with the help of complementary high-level theoretical calculations.

Thus, in this work, the spectroscopic properties of the anisole-methane van der Waals cluster are examined using two color resonance two photon ionization (2CR2PI) in combination with time-of-flight analysis (TOF). Despite the importance of the interactions, experimental results are limited on the binding interactions of the C-H-π clusters. To address this issue, we utilize a technique, two-color appearance potential (2CAP) measurement, that was recently employed in our group to examine the π-stacked

fluorene dimer.[60] Thus, two Color Appearance Potential (2CAP) measurements were

conducted on the monomer and the isolated anisole-methane cluster to determine the

binding energies as shown in Figure 2.1-2. With all the relevant information available

that is, 2CR2PI excitation spectra, ion yield spectra and 2CAP measurements of the

ground state binding energy of the neutral cluster, the binding energies for the S_1 and D_0

states can be retained to spectroscopy accuracy by applying the thermochemical

cycle.[103,60] The experimental BE is a valuable parameter to measure as it provides a

benchmark for the complementary theoretical methods.
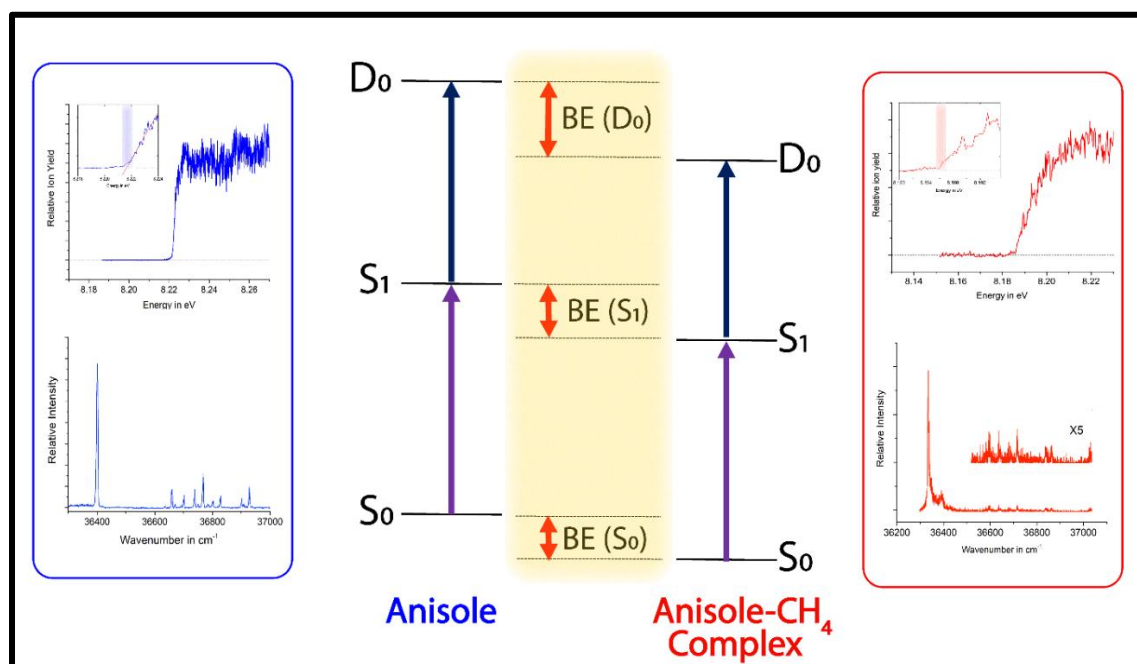
Figure 2.1-2: A snapshot of the spectroscopic data for anisole and anisole-methane complex, together with the energy correlation diagram. 2CR2PI measurements were used for the excitation spectra and ion yield spectra for the monomer and the complex.

2.2 RESULTS AND DISCUSSION

2.2.1 2CR2PI SPECTRA OF ANISOLE AND ANISOLE-CH$_4$ 1:1 CLUSTER

Initial experiments targeted a reference system, in this instance the toluene-methane 1:1 cluster, which has been previously investigated, to optimize the performance of the instrument and to establish the experimental conditions (method) suitable for forming the weakly bound clusters. The 2CR2PI spectra of toluene and toluene-methane van der Waals cluster were obtained under the experimental conditions reported earlier. The toluene-methane origin band appeared to the lower energy side of the toluene monomer origin band by –42 cm^{-1}. The 2CR2PI excitation spectra of both toluene and toluene-methane complex are shown in Figure 2.1-3 and are in excellent agreement with results previously reported.[121,123] A more detailed discussion of experiments on the toluene-methane complex is not included in this document as it has been previously reported.

Following the toluene-methane investigation to establish optimum conditions for the formation of weakly bound complexes with methane, 2CR2PI spectra for the jet cooled anisole monomer and the anisole-methane complex were recorded and are shown in Figure 2.1-4. Details on the experimental procedure used and optimized conditions are included in chapter 2. The electronic excitation spectrum of pure anisole was readily obtained, and it agreed well with that previously reported.[105] The (S$_0$-S$_1$) transition is typically a n-π* transition involving the donation of electron density from the oxygen of anisole towards the ring upon electronic excitation.[107] Some of the fundamental

vibrational frequency modes are observed to the high energy region of anisole origin (36400 cm^{-1}) and a detailed discussion on the assignment of fundamental vibrational modes of anisole in S_1 state can be obtained from previous publications.[105,108,124]

The anisole-methane cluster origin band was found at 36336 cm^{-1}, red shifted (-64 cm^{-1}) with respect to the monomer origin band transition (S_0-S_1). As found for anisole, the spectrum is origin dominated. Smaller features appear to the high energy region of the complex origin band which are probably due to intermolecular vibrational modes of methane with respect to the anisole chromophore. The magnitude of the red shift (–64 cm^{-1}) for the cluster is significantly larger than that observed for benzene-methane (–41 cm^{-1}) and toluene-methane (–43 cm^{-1}) 1:1 clusters. This clearly shows how the substituent affects the electronic structure of the aromatic π system. The electronic density is believed to be greater in the excited state (S_1) than in the neutral state (S_0) and the red shift is indicative of the cluster being more strongly bound in the former than the later state,[4] since the electronic transition enhances the stability of the interaction.[102,107] The frequency shift in the origin band of the out of plane structure of anisole-methane cluster is opposite of what is observed for the in plane structures of anisole-water and anisole-carbon dioxide systems which are blue shifted from the monomer origin.[101,113,124,118] A correlation between the magnitude of the frequency shift and the cluster geometry was previously established for the salvation of small molecules on aromatic chromophores. It was observed that the closer the solvent (small molecule) is to the aromatic ring system, the greater the red shift.[123] The influence of the intermolecular interactions of methane on anisole is demonstrated by small shifts in the aromatic ring vibrations upon complexation.
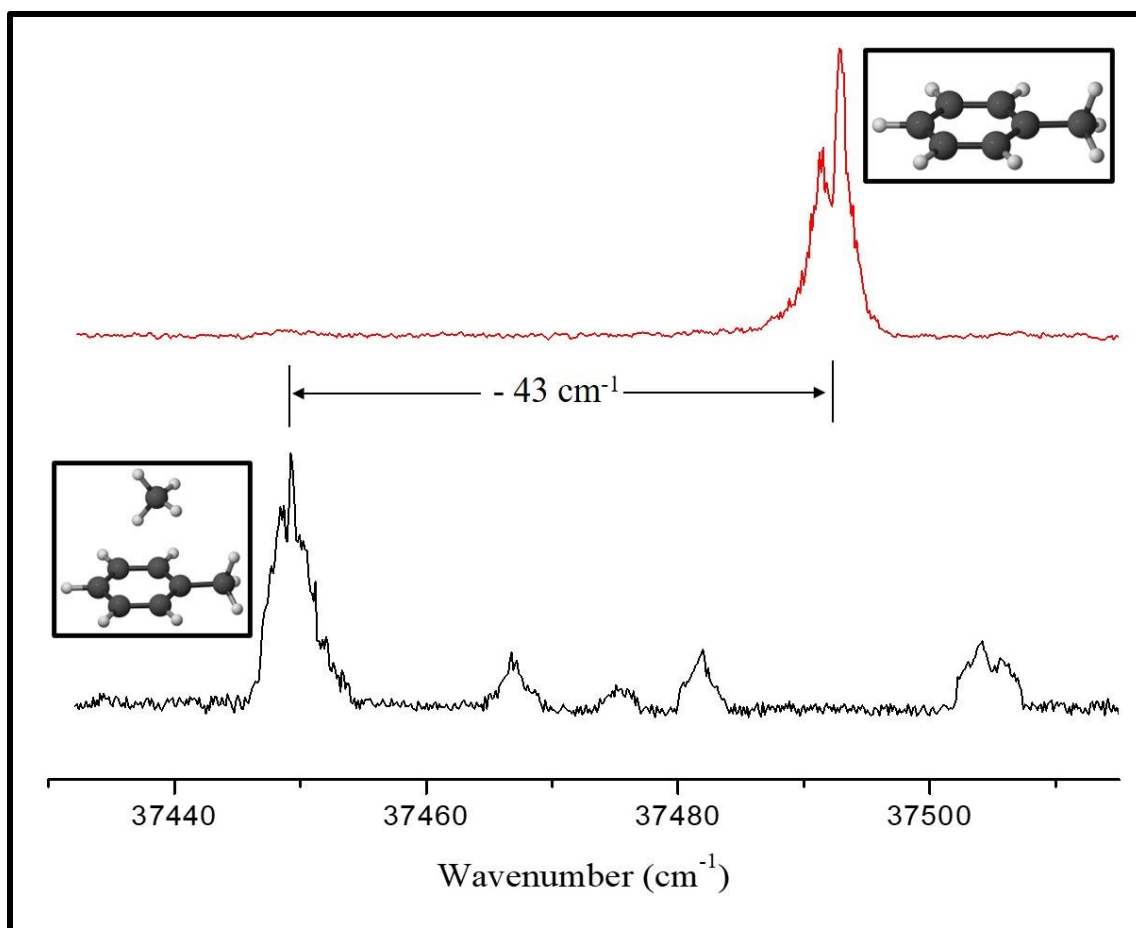
Figure 2.1-3: 2CR2PI mass spectrum of toluene (red) and toluene-methane cluster (black).
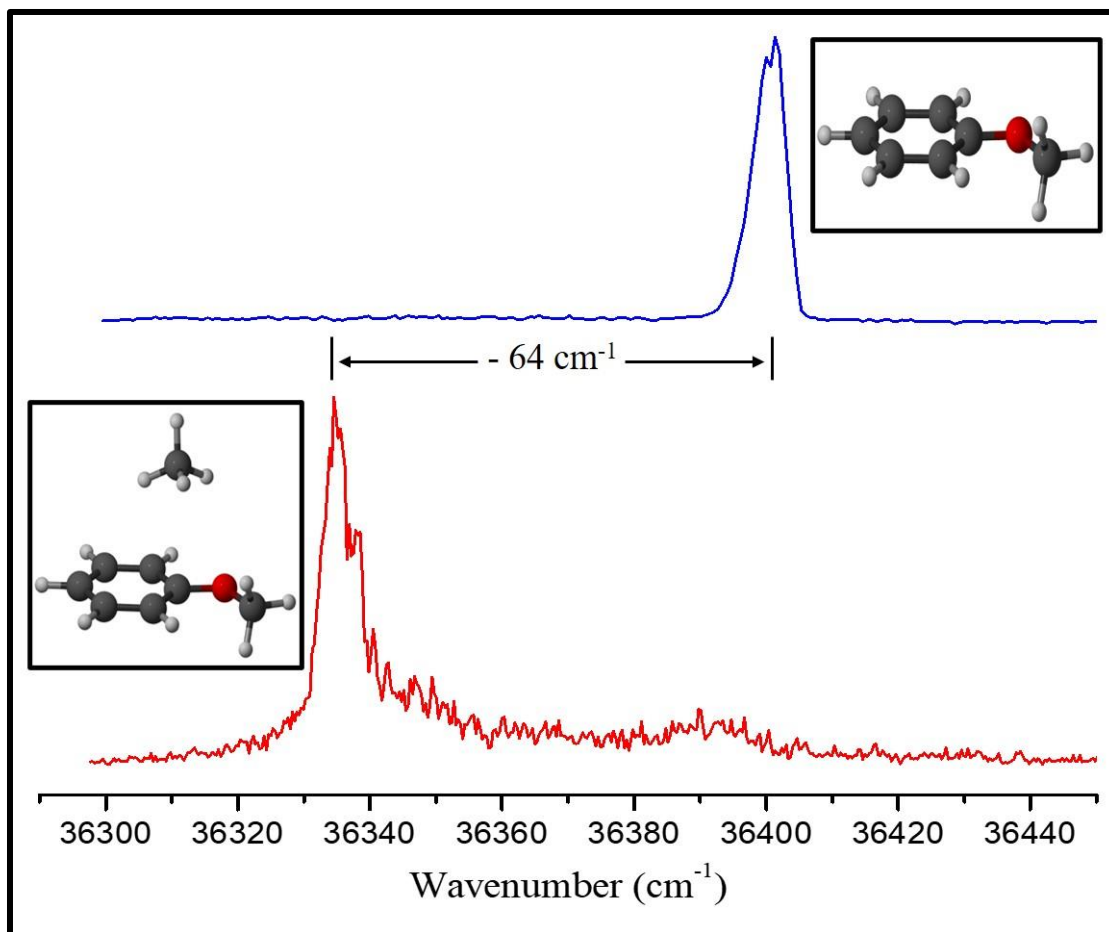
Figure 2.1-4: 2CR2PI mass spectrum of anisole (blue) and anisole-methane cluster (red).

2.2.2 2CAP MEASUREMENTS OF ANISOLE-CH$_4$ 1:1 CLUSTER

Ion yield (IY) spectra measurements were conducted to determine the ionization potentials (IP) for the monomer and the 1:1 cluster, respectively, which are shown in the upper panels of Figure 2.1-2-. In the monomer IY curve, a sharp ionization onset is clearly observed, giving an IP of 8.222(5) eV. A sharp onset is also observed in the corresponding cluster IY curve, giving an IP of 8.186(5) eV. The relatively sharp onsets observed in both spectra are indicative of minimal geometry changes upon ionization. The IP values have been reported to one standard deviation and it is noteworthy for the

first time the IP value for the anisole-methane cluster has been reported. The value
obtained for the monomer IP is slightly lower than that previously obtained (8.232)
eV[108,109] and this difference in values can be attributed to the fact that measurements
reported here were not corrected for shifts arising from electrostatic fields in the time of
flight mass spectrometer. Indeed, it is the difference in IPs which is relevant for our
studies.

With the excitation and IP curves determined for the anisole monomer and
complex, two color appearance potential (2CAP) measurements were then conducted.
The primary difference between 2CAP and IP measurements is that in the latter, the
cluster ion is detected, while in the former the monomer (anisole) cation is detected,
which results from the breakup of the cluster. The energetic onset making the appearance
of the anisole cation fragment represents the sum of the ground state binding energy and
the ionization potential of the monomer as illustrated in the left section of Figure 2.1-5.
From the 2CAP spectrum presented in the right section of Figure 2.1-5, two clear sharp
onsets are observed. The onset to the lower energy side represents a hot band
($6b_1^1$ transition) of the anisole monomer, which overlaps the electronic origin of the
anisole-methane 1:1 cluster. This hot band was more prominent at low backing pressure
and made it difficult to observe the onset of cluster breaking on the anisole mass channel
when scanning λ_2. By cooling the anisole to reduce its concentration in the beam and
operating at high backing pressure, we could relatively minimize the hot band as
illustrated in Figure 2.1-6. At high backing pressure more collisional cooling occurs,
lowering the vibrational temperature of the entrained species. Since anisole has an
excited state lifetime of around 23 ns, the time delay between the excitation and the

ionizing laser was biased against the monomer hot band signal by increasing the delay between the two lasers to 50 ns. However, this complication had no effect when analyzing the cluster ion in spectroscopic experiments.

In Figure 2.1-5, the onset to the higher energy side represents the true color appearance potential for the anisole monomer obtained from the fragmentation of the anisole-methane 1:1 cluster. The x-axis energy scale for the 2CAP spectrum of the complex was then obtained by doing a linear extrapolation to obtain the energy of the two photons, followed by subtracting the previously obtained monomer IP value. A ground state (S_1) binding energy value of 0.060(2) eV was obtained, equivalent to 5.8(2) kJ/mol in a more traditional unit used for reporting cluster binding energies. The method sets up an upper limit to the binding energy values estimated and through the application of the thermochemical cycle shown in Figure 2.1-2, binding energies of 6.6(2) and 9.2(2) kJ/mol are retained for the S_1 and D_0 respectively.
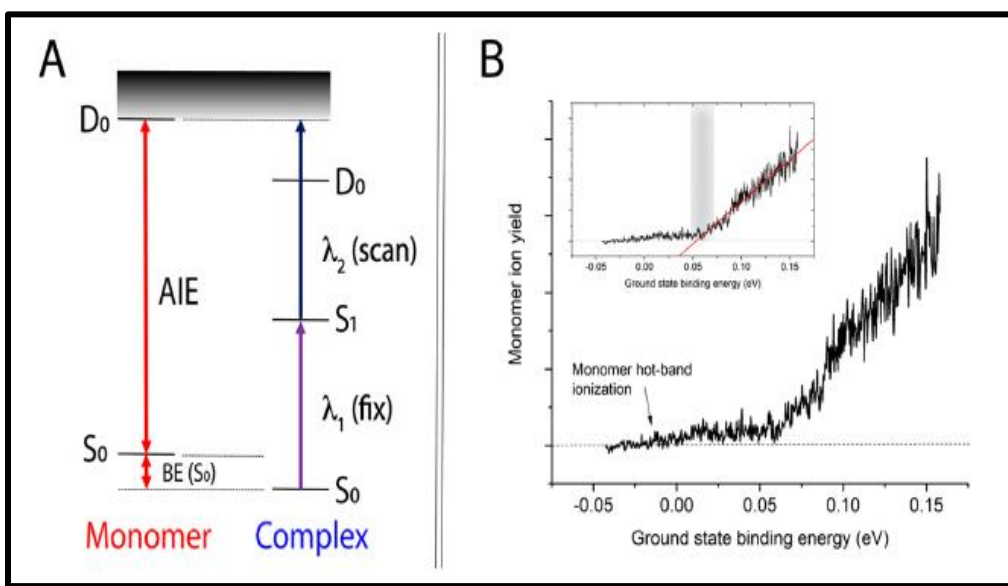
Figure 2.1-5: Schematic of the 2CAP technique (A) and 2CAP spectrum of anisole-methane complex (B).
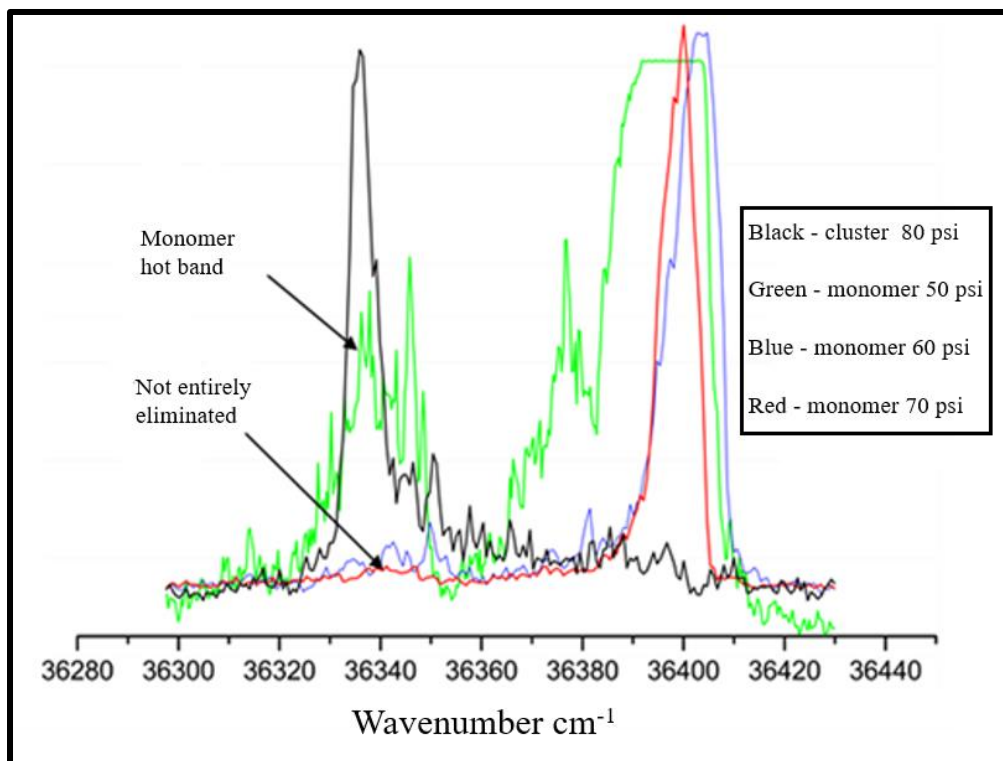
Figure 2.1-6: An illustration of the monomer hot band overlap with the origin of anisole-methane 1:1 cluster.

2.2.3 VMI MEASUREMENTS OF ANISOLE-CH$_4$ 1:1 CLUSTER

To validate the results from the 2CAP experiments, velocity ion imaging (VMI) experiments were carried out using our newly constructed VMI spectrometer, following the procedure explained in chapter 2 of this document. Images were collected below and above the breaking threshold over a period of 30 minutes. In this time period, typically 18000 (=30 min x 60 sec/min x 10 shots/sec) laser shots were acquired. During image acquisition, the signal was attenuated by introducing a polarizer into the path of the laser beam to ensure that only a few ions are detected, a necessary step taken to avoid image blurring from space charge effects.

The upper panel of Figure 2.1-7 show VMI images collected for the anisole cation following excitation of the anisole-methane cluster at the total energies shown. The image to the far left was taken at an energy below the breaking threshold, while the rest of the images were taken at energies above the breaking threshold. The images acquired above breaking were background corrected using images obtained with the second photon set below the threshold. Following the background correction, the three images collected above the ionization threshold were Inverse Abel transformed using the pBASEX algorithm to produce a probability of energy P(E) and kinetic energy distribution plot of the images as shown in the lower panel of Figure2.1-7. From the plot, it is observed that the maximum kinetic energy (KE_{max}) of the cation fragment increases as the total energy above the dissociation threshold increases, and this agrees well with conservation of energy equation (eq. 1). The cluster binding energy in D_0 was then derived from the KE_{max} and the total available energy at each data point collected. This was then averaged over measurements collected at different ionizing photon wavelengths. With the D_0 binding energy value determined, the corresponding binding energy values for the S_0 and S_1 were retained using the thermochemical cycle shown in Figure 2.1-2. The values are reported to one standard deviation as shown in Table 2.1, which compares the VMI and 2CAP measurements. Remarkably, results from the VMI are in excellent agreement with results from the 2CAP measurements.
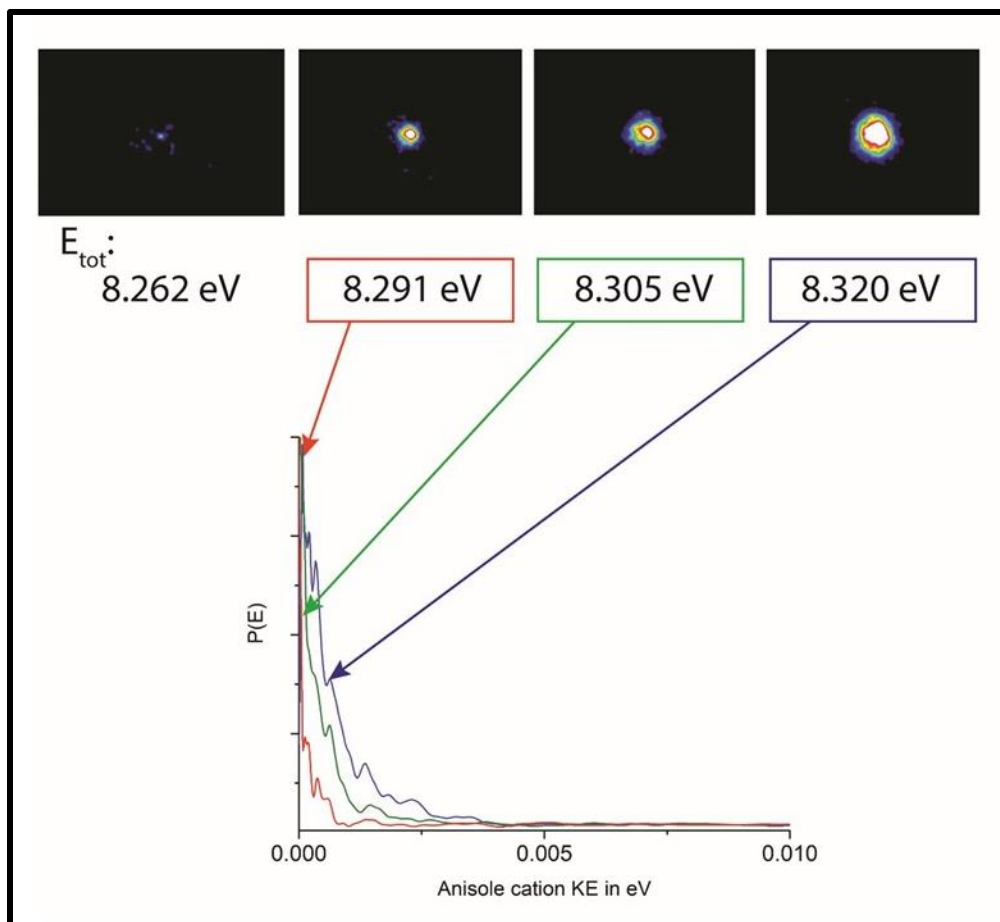
Figure 2.1-7: Upper panel, anisole monomer images obtained from the dissociation of the ionized anisole-methane complex at four different total energies highlighted. The lower panel presents a plot of P(E) distribution vs the kinetic energy of anisole cation fragment.

Table 2.1: Comparison of experimental 2CAP and VMI binding energies for the anisole-methane 1:1 cluster in the three electronic states. Binding energy values are reported to one standard deviation in parenthesis.

Method	Binding Energy (kJ/mol)		
	S_0	S_1	D_0
Experiment (2CAP)	5.8(2)	6.6(2)	9.2(2)
Experiment (VMI)	5.8(1)	6.6(1)	9.2(1)

2.2.4 THEORETICAL CALCULATIONS FOR ANISOLE-CH$_4$ 1:1 CLUSTER

Electronic structure calculations were carried out to estimate the equilibrium geometries and energetics of the anisole-methane 1:1 complex using the GAUSSIAN 09 software package.[125] Geometry optimization and the corresponding binding energy calculations for the anisole-methane cluster were carried out using both dispersion corrected Density Functional Theory (DFT) and *ab initio* methods. The full geometry optimizations were carried out from a variety of initial configurations which included geometries sampling out of plane C-H···π interactions and in-plane C-H···O hydrogen bonding interactions. The methods of choice were based on previous studies. In a study of the benzene dimer, PBE0[126,127] density functional augmented with the D3 version of Grimme's dispersion term could accurately predict the ground and excited state energies of the dimer.[125] Recent studies on fluorene based compounds proved that the CAM-B3LYP-D3 with QZVPPD or 6-311++g(3df, 3pd) basis sets was a better method in reproducing the binding energies across all three states (S_0, S_1, D_0).[128,129] The calculated binding energies were also corrected for zero point energy (ZPE) and basis set superposition error (BSSE) using the counterpoise correction method. It was observed that the BSSE was negligibly smaller at the QZVPPD and 6-311++g(3df, 3pd) basis set.

Considering the cation radical states, previous computational studies of π stacked dimers revealed the calibrated BILYP functional with 40% of Hartree Fock exchange (BILYP-40) was the best method in reproducing the properties of the cation radical state of π-conjugated systems.[60] However, this method performed poorly in the current study,

and we instead resorted to dispersion corrected DFT and *ab initio* methods to evaluate the binding interactions in the ground and cation radical states.

Complete geometry optimization of the complex yielded the structure shown in Figure 2.1-8 as the lowest energy conformer for the ground state. The methane is positioned above the plane of the anisole ring, with one C-H interacting with the O atom lone pair and a second hydrogen interacting with the π system of the anisole aromatic ring. The average distance between one hydrogen of methane and the aromatic ring oxygen is approximately 3.100 Å in the S_0 state.

Following the ground state geometry optimization, optimizations in the cation radical state were also performed using spin unrestricted wavefunctions at different levels of theory and with different basis function. Figure 2.1-9 compares the optimized geometrical structures of anisole methane complex in the ground and cation radical states. In the later, not only is the methane shifted more towards the methoxy substituent of anisole but also, the C-H$^{...}$O bond length shortens to 2.868 Å than in the former (3.134 Å). However, the optimized structure for the D_0 state is roughly consistent with the S_0 state structure. This is consistent with the sharp onset observed in the ion yield curve and the origin dominated excitation spectrum which suggest a smallest geometry change upon excitation.
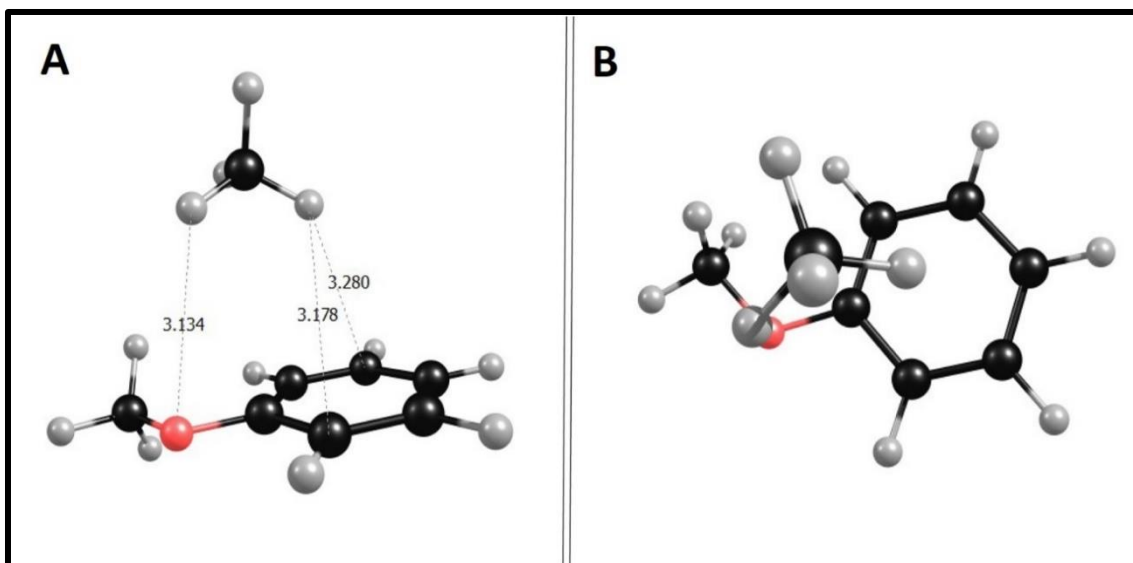
Figure 2.1-8: A. Optimized ground state (S_0) structure for the anisole-methane 1:1 complex at the PBE0-D3/def2-QZVPPD level of theory. **B**. Alternate view illustrating the presence of both C-H···O and C-H···π interactions in the complex.
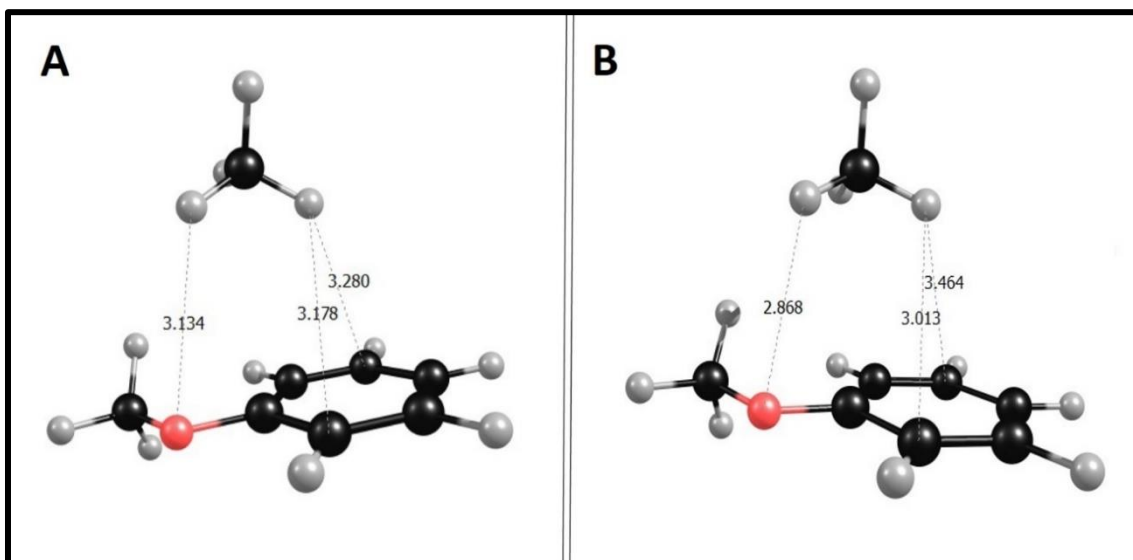
Figure 2.1-9: Comparison of the optimized structures of anisole-methane complex for the S_0 (A) and B for the (D_0) state at the PBE0-D3/def2-QZVPPD level of theory.

Considering the binding energy calculations in the ground state, the optimized structure of the complex was corrected for ZPE and BSSE using the counterpoise method at the different levels of theory. The procedure used was explained in detail in section 1.3 of Chapter 1. The calculated binding energies estimated very well the experimental binding energies for the S_0 state, and the values ranged from 5.2 to 6.6 kJ/mol as shown in Table 2.2. When comparing between the methods used for the optimization and hence the binding energy calculations, the MP2/6-31++(3df,3pd) level of theory was the best in matching the experimental ground state binding energy.

The same approach was employed for the D_0 state with the only difference being that spin unrestricted wavefunctions were used, and when doing the counterpoise correction, the two fragments were defined by assuming that the anisole chromophore is ionized (anisole cation radical), with the methane fragment being neutral. The calculated binding energy values ranged from 9.2 to 10.5 kJ/mol, which are in very good agreement with experimental results from 2CAP and VMI experiments. The only exception was from the UMP2/aug-cc-pVTZ level which underestimated the experimental value by roughly 25% (6.6 kJ/mol). The UCAM-B3LYP-D3/6-31++(3df, 3pd) level was the best method for estimating the experimental binding energy in the cation radical state. Some theoretical results have not been reported on Table 2.2 due to time constraints and issues encountered when running the calculations on the PERE cluster.

Very few studies have been reported on the direct measurements of aromatic-methane systems[130] and it will be informative to do a comparison of our results with previous experimental and theoretical studies. Related theoretical studies on clusters of methane with benzene as a prototypical system for C-H$\cdots\pi$ interactions predict that the

1:1 complex adopts a C_{3v} symmetry, with one C-H of the methane interacting directly with the π system of the aromatic ring through a C-H···π interaction.[122] In an experimental study, high resolution MATI spectroscopy predicted the magnitude of the C-H···π binding interactions to be in the rage of 4.31-4.73 kJ/mol,[131] and this was very consistent with the estimated theoretical value at the CCSD(T) level of theory.[122]

To investigate C-H···O binding interactions, Ruckenstein and coworkers performed theoretical studies on clusters of methane and water using ab initio methods, and predicted the interaction energy of the methane-water 1:1 complex to be around 1 kJ/mol.[132] It is interesting to note that the binding energy which we measure for the anisole-methane 1:1 complex, in comparison with prior measurements of benzene–methane and water-methane 1:1 complexes, is consistent with the dual role of C-H···π and C-H···O interactions in stabilizing the cluster. This is borne out by theoretical calculations of the optimized ground state structure of the complex, which cannot be determined by our experimental measurements.

Table 2.2: Comparison of experimental and computed binding energies for the anisole-methane 1:1 cluster. Experimental binding energies are reported to one standard deviation in parenthesis. Calculated binding energies were corrected for ZPE and BSSE.

Method	Binding Energy (kJ/mol)		
	S_0	S_1	D_0
Experiment (2CAP)	5.8(2)	6.6(2)	9.2(2)
Experiment (VMI)	5.8(1)	6.6(1)	9.2(1)
PBE0-D3/6-311++G(3df,3pd)	6.6		10.5
PBE0-D3/def2-QZVPPD	6.1		9.7
B3LYP-D3/6-311++G(3df,3pd)	5.5		9.4
M06-2X-D3/6-311++G(3df,3pd)	5.4		9.5
CAM-B3LYP-D3/6-	5.3		9.1
CAM-B3LYP-D3/def2-QZVPPD	5.2		9.0
MP2/6-311++G(3df,3pd)	5.8		...
MP2/aug-cc-pVTZ	6.0		6.6

2.3 CONCLUSIONS ON ANISOLE-CH$_4$ 1:1 CLUSTER

The study of prototypical van der Waals complexes provide a means for understanding the nature and strength of non-covalent interactions. An examination of the anisole-methane cluster was carried out here using mass selected 2CR2PI spectroscopy in concert with electronic structure calculations. Important insights were gained on the nature and strength of the interactions involved. We used 2CAP and VMI experiments to characterize the binding interactions of anisole-methane 1:1 cluster in the three respective electronic states, i.e., the S_0, S_1 and D_0 states. The obtained experimental results were in excellent agreement with the theoretical predictions obtained using DFT and *ab initio* methods. The optimized ground state structure of the complex showed the dual presence of C-H···O and C-H···π interactions and this was consistent with the measured ground

state binding energy. Furthermore, with the methane positioned above the ring, a red shift

in the cluster origin with respect to the monomer origin band was observed.

CHAPTER 3: ANISOLE–CH₄ 1:2 VAN DER WAALS CLUSTER

This work builds upon our previous investigation of anisole-methane 1:1 complex discussed in chapter 2. In this section we focus on the 1:2 complex of anisole-methane to study solvation effects and cooperativity in binding.

3.1 BACKGROUND ON HIGHER ORDER CLUSTERS OF AROMATICS WITH ATOMS AND MOLECULES

The detailed mechanisms of solvation continue to be actively explored through the study of isolated molecular clusters,[9,142] yielding insights into the strength and mechanisms of hydrogen bonding,[137] halogen bonding and other sigma-hole type interactions,[26,138,139] π-π interactions,[134] C-H-π interactions,[4,131,140–146] and C-H-O interactions,[22,23] among others. Following initial solvation with a single solvent molecule, competition between self-interaction in the solvent and interaction with the solute chromophore can occur, leading to differing solvation mechanisms. Studies of micro–solvation, exploring the role of competition between solute-solvent and solvent-solvent interactions, can be probed via the study of higher order complexes. For solvents with strong hydrogen bonding interactions, e.g. ammonia (dimer binding energy of 12.9 kJ/mol)[147] or water (dimer binding energy of 20.9 kJ/mol),[148] the solvent-solvent interaction may dominate. For example, studies of $PhCl\cdots(NH_3)_n$ (n =1-3) complexes show that upon ionization, the $PhCl\cdots NH_3$ dimer (i.e., n = 1) cation radical reacts via two distinct pathways: 1) Cl atom loss, to give protonated aniline, and 2) HCl loss, to give the

aniline cation radical.[72] These reactive pathways are blocked in complexes with $n = 2$ and 3, presumably due to the larger self-interaction between the ammonia moieties.

The role of cooperativity in the binding energies of model complexes and clusters is an active research area. Representative studies include the examination of interplay between hydrogen bonding, anion-π and lone pair-π interactions in anion recognition,[149] the cooperativity of hydrogen and halogen bonding interactions,[150] competition between weak hydrogen bonds,[151] and the strengthening effect of halogen, chalcogen, and pnicogen bonding on the halogen-π interaction.[152] Many contributions in this area to date have come from theory. Experimental investigation of such effects in weakly bound complexes is challenging, yet significant progress has been made in the study of three body effects between aromatics and rare gases. Hobza and coworkers determined the binding interactions of benzene-Ar and benzene-Ar_2 clusters to be 649.2 cm^{-1} and 1324.7 cm^{-1} respectively,[153] indicting an increase in binding energy for the second Ar (+4%). In a related study, Lawrence and Bellm investigated the dissociation energy for the loss of an Ar atom from the p-difluorobenzene-Ar_2 complex (339 cm^{-1}).[87] Using a previously derived value for the dissociation of the p-difluorobenzene-Ar complex (337 cm^{-1}),[86] they concluded that the two values were consistent within experimental uncertainty, and the presence of the first Ar atom affected the binding energy of the second by less than ~ 2%. Solvation of anisole with Ar atoms ($n = 1$-3) has been studied by Mazzoni et al, using a combination of quantum chemical calculations and high resolution resonant two-photon Ionization techniques.[92] They found the global minimum structure of the An$\cdots$(Ar)$_2$ system was one where the Ar atoms sat on opposite faces of the aromatic chromophore, and that the addition of a third Ar had no distinct minimum.[154,155]

Complexes of two methane molecules with benzene, toluene, and aniline have previously been studied using Resonant 2-photon Ionization (R2PI) spectroscopy by Bernstein and co-workers.[123,156,157] Two distinct structures were considered, with the methane molecules positioned on the same side or on opposite sides of the aromatic ring. These early studies demonstrated a strong dependence of spectral shift on cluster geometry. Taking benzene-methane as an example, the 1:2 cluster resulted in two distinct geometries which had different spectral shifts.[156] Following their assignments, a conformer with the methane moieties on opposite sides of the ring gave a spectral shift in the electronic spectra with respect to the bare chromophore that was approximately additive; i.e., roughly twice that of the 1:1 complex. A second conformer, with the methane molecules on the same side of the aromatic ring, gave a spectral shift observed that was non-additive and similar to that observed for the 1:1 cluster.

Two distinct isomers were also found for the toluene-$(CH_4)_n$ 1:2 complex.[123] Here the isomer with both methane moieties on the same side exhibited an electronic origin shifted to the blue of the 1:1 complex, which itself lies roughly 43 cm^{-1} to the red of the toluene monomer origin. In contrast, the isomer where the methane moieties were found on opposite sides of the chromophore led to a larger red shift, again additive in being roughly twice that found for the 1:1 complex. Interpretation of spectral shifts is somewhat qualitative, as the shift arises from the relative difference in binding energy between S_1 and S_0. However, complexes of aromatics which involve the π system tend to be more strongly bound in the S_1 state and thus exhibit a red-shifted spectrum. Thus, the origin position of the 1:2 same side isomer is consistent with disruption of the C-H/π interaction of the first methane by binding of the second. In contrast, the binding of a second

methane on opposite face of the π-system leads to no such disruption and a larger red-shift from the monomer origin.

For the anisole-$(CH_4)_2$ complex, various structures are thus expected, with the two methane molecules being on opposite sides of the aromatic ring or on the same side. The anisole-methane 1:2 cluster will be characterized by mass selected 2CR2PI, 2CAP and VMI, and experimental results will be augmented with theoretical calculations to gain important insights into solvation effects. The properties of interest will be the solvent spectral shift, cluster geometry and the binding interactions between successive solvent species and the solute molecule.

The experimental beam conditions and laser configurations used for the mass selected 2CR2PI, 2CAP and VMI experiments were similar to the ones described previously for the anisole-methane 1:1 cluster experiment. Briefly, a premix of 10 % methane in Ar carrier gas was bubbled through liquid anisole (sigma Aldrich, 99 % purity) held in a refrigerated bath maintained at 5 °C. The gaseous mixture was then expanded into the source chamber of the REMPI-TOF and VMI spectrometer respectively.

<center>3.2 RESULTS AND DISCUSSION</center>

<center>3.2.1 2CR2PI SPECTRA OF ANISOLE AND ANISOLE-$(CH_4)_n$ (n=1,2) CLUSTERS</center>

The mass selected 2CR2PI spectra of anisole and anisole-methane 1:1 and 1:2 clusters are presented in Figure 3.1-1. The origin band of the 1:2 cluster is shown to be red shifted by 129 cm^{-1} with respect to the monomer origin, which is twice that of the

anisole-methane 1:1 complex (64 cm^{-1}). The additive spectroscopic shift is consistent

with related studies of methane complexes with benzene and toluene,[123,156] and suggests

that the two methane molecules occupy equivalent positions on opposite faces of the ring.

Peaks close in frequency to the 1:1 cluster have been observed for benzene···(CH$_4$)$_2$ and

toluene···(CH$_4$)$_2$ and were assigned to the conformer in which both methane moieties

reside on the same side of the ring. Here, there is but a hint of a minor feature lying ~ 68

cm^{-1} from the monomer origin in the 1:2 cluster spectrum, slightly red shifted from the

1:1 complex origin. This could represent a second conformer, but the intensity is very

weak, and this feature was not considered further.
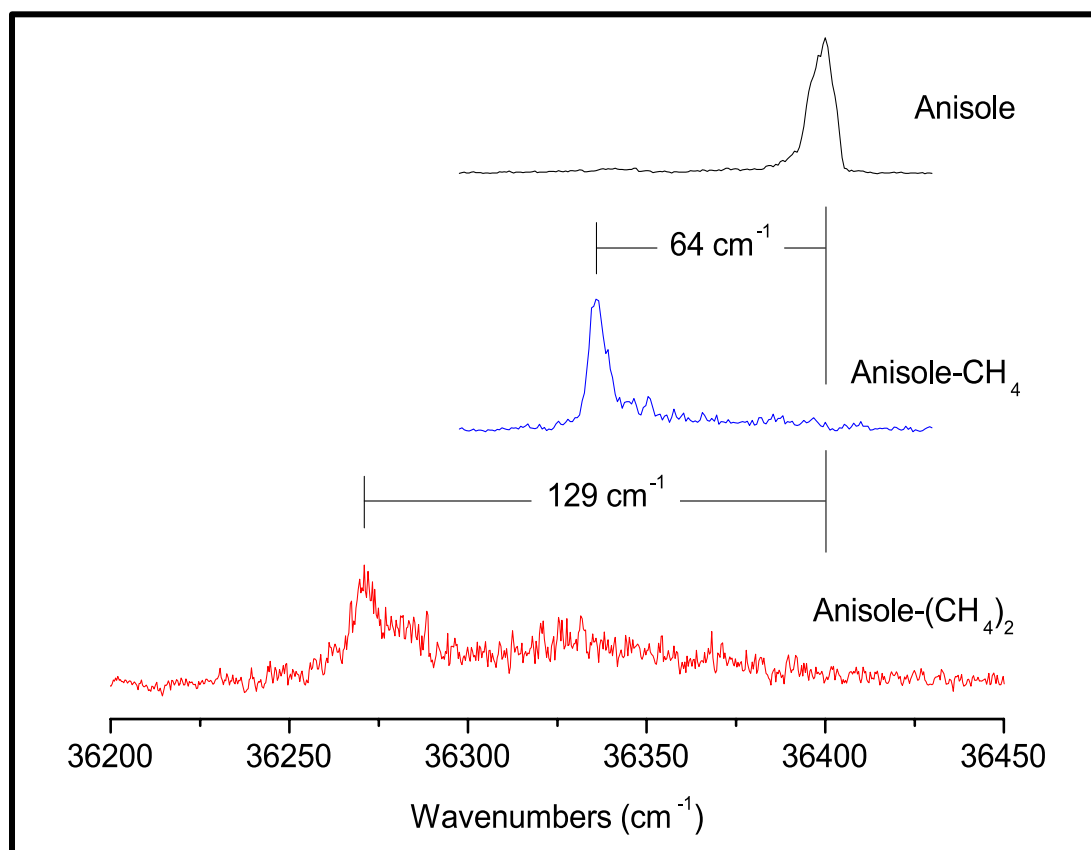
Figure 3.1-1: A comparison of mass selected 2CR2PI spectra of anisole, and anisole-methane 1:1 and 1:2 cluster.

3.2.2 2CAP MEASUREMENTS OF ANISOLE-CH$_4$ 1:2 VAN DER WAALS CLUSTER

The ionization potential (IP) for the anisole-methane 1:2 complex was determined using the experimental procedure employed earlier for the anisole-methane 1:1 complex. The upper figure in the right panel of Figure 3.1-2 shows the measured IY curve for the anisole-methane 1:2 complex, obtained by setting the pump laser on resonance and scanning the frequency of the second laser through the ionization threshold, monitoring the onset of the cluster signal. The anisole-methane 1:2 cluster ionization onset is more gradual compared to that of the 1:1 cluster with a clear threshold observed around 8.151(5) eV. This value is slightly lower than the previously determined IP values for the anisole monomer and anisole-methane 1:1 complex respectively. The difference in IP values have also been observed for the anisole-argon and anisole-argon 1:2 aggregates.[158] This result can be interpreted on the basis of the higher order clusters stabilizing further the cationic charge in the ionized cluster. This trend was previously observed for fluorene based clusters where the IP sequentially dropped with cluster size.[59,60,62] The IY curve for the anisole-methane 1:1 complex is not discussed further as it was reported earlier.
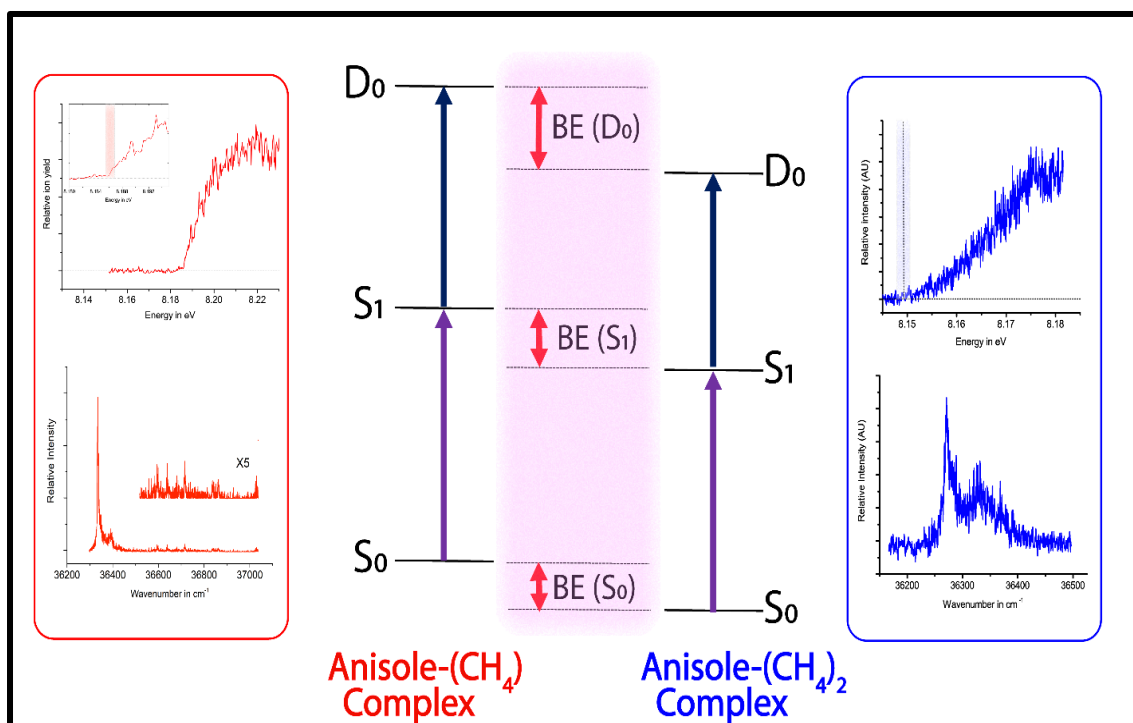
Figure 3.1-2: A snapshot of the spectroscopic data obtained for the 1:1 and 1:2 anisole-methane complexes, together with the energy ladder diagram. For each species, electronic spectra (S_0-S_1) were obtained in 2CR2PI experiments as described in the text (lower figure in each panel). Ion yield spectra were obtained in 2CR2PI measurements using a tunable second photon, to determine the ionization threshold (upper figure in each panel).

Two-color appearance potential (2CAP) measurements of the anisole-methane 1:2 complex were conducted following the procedure described previously for the anisole-methane complex. The production of the (anisole-methane)$^+$ cation from the fragmentation of the anisole-methane 1:2 complex was monitored by setting the excitation laser on resonance while scanning the ionizing laser. The energetic onset making the true appearance potential of the (anisole-methane)$^+$ cation fragment represents the sum of the ground state binding energy and the ionization potential of the anisole-methane complex as illustrated in the left panel of Figure 3.1-3. The 2CAP spectrum of the anisole-methane 1:2 cluster, plotted in terms of binding energy in the ground state (S_0) using the derived anisole-methane IP is shown on the right section of

Figure 3.1-3. An upper limit to the ground state (S_0) binding energy value of 0.067(2) eV

(6.5(2) kJ/mol) was obtained following a linear extrapolation of the rising edge to the

baseline and the subsequent subtraction of the anisole-methane 1:1 complex IP value.

Application of the thermochemical cycle shown in Figure 3.1-2 retains the binding

energies of 0.075(2) and 0.103(2) eV for the S_1 and D_0 states respectively. As mentioned

earlier, these are upper limit to the true binding energy values.
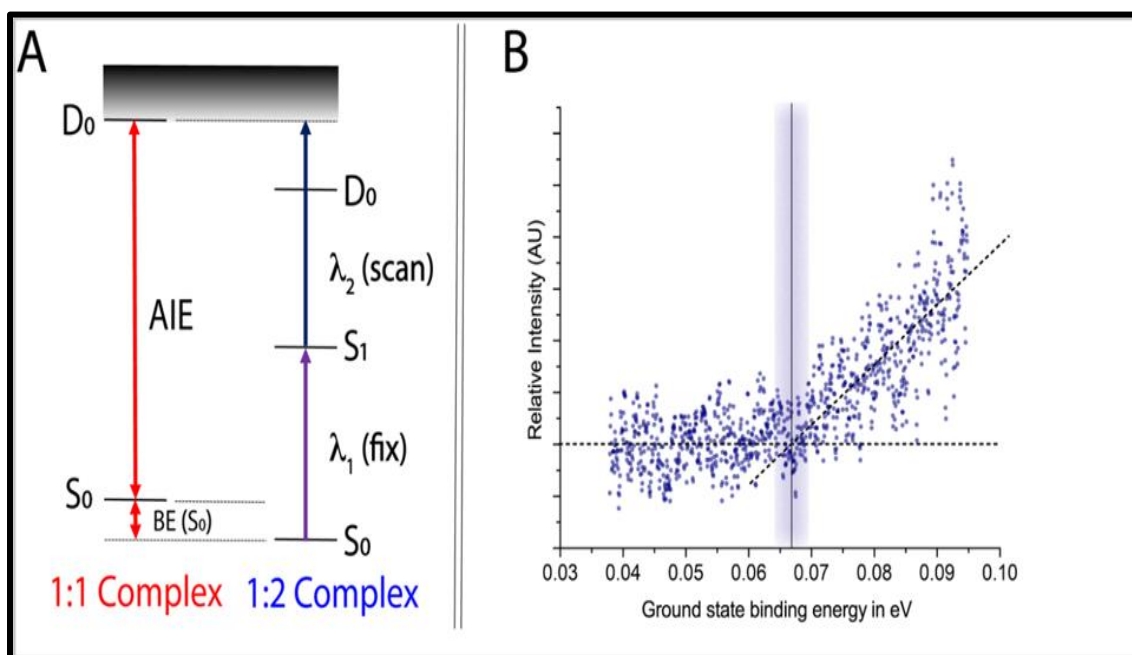
Figure 3.1-3: A: Illustration of the 2CAP method as used to determine the binding energy of the 1:2 complex. Here the reference system is the 1:1 complex. **B**. 2CAP measurements for the anisole-methane 1:2 complex. The x-axis is scaled to reflect the ground state binding energy of the complex with respect to loss of a single methane.

3.2.3 VMI MEASUREMENTS OF ANISOLE-CH$_4$ 1:2 VAN DER WAALS CLUSTER

VMI experiments were also conducted to determine the binding energy of

anisole-methane 1:2 cluster in the cation radical state (D_0) for comparison with the results

from the 2CAP measurements. The procedure used was similar to the one presented

earlier for the determination of the binding energies of anisole-methane 1:1 complex and

it involved measuring the kinetic energy of the anisole-methane cation radical following

the detachment of a single methane from the ionized 1:2 complex. Figure 3.1-4 displays

VMI images obtained at three different two-color energies of 8.226 eV (below

dissociation threshold), 8.260 eV, and 8.283 eV. From the analysis of the energetic cutoff

in the transformed kinetic energy distribution, we derived an upper limit to the binding

energy in the D_0 state of 0.102(2) eV or 9.8(2) kJ/mol. The corresponding binding

energies for the S_1 and S_0 states were retained after the application of the thermochemical

cycle shown in Figure 3.1-2.
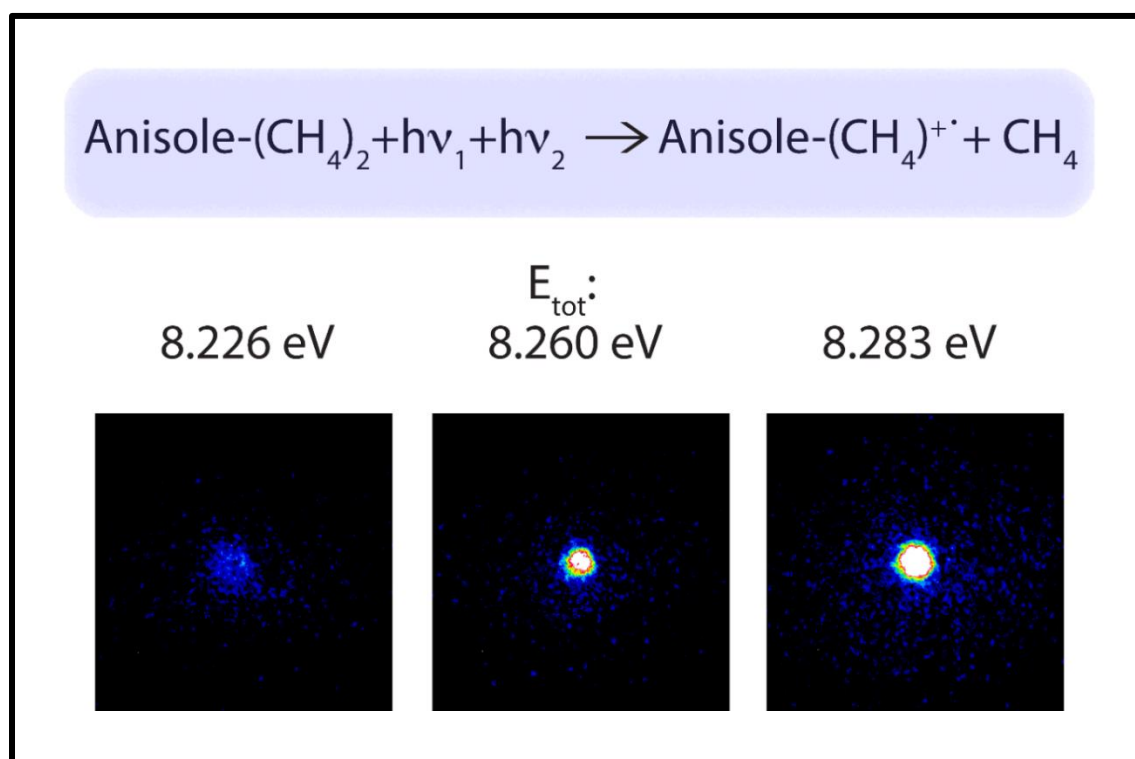
Figure 3.1-4: Velocity mapped ion images of the 1:1 anisole-methane cation radical produced from dissociative ionization of the 1:2 anisole methane complex using two-color sequential ionization. In the panel at left, the total energy is below the fragmentation threshold.

The values obtained across all three electronic states are presented in Table 3.1, which also compares the 2CAP and VMI data with that of anisole-methane 1:1 complex. The 2CAP and VMI experimental results were in excellent agreement, a trend also observed from the previous investigation of anisole-methane 1:1 complex. When compared with our earlier study of the 1:1 complex, these results show a 10% increase in the binding energy for the 1:2 complex across all three states (S_0, S_1, D_0). If the methane molecules occupy equivalent positions, it is expected that the dissociation energy for the removal of methane from anisole-methane 1:2 complex be comparable to that of the removal of methane from anisole-methane 1:1 complex. Thus, binding of the first methane molecule may have perturbed the electronic properties of the chromophore, leading to an increase in the binding interaction for the second methane. However, the values differ slightly, there is a 10% increase in the binding energy values obtained when compared to the previous result on the anisole-methane 1:1 complex. The difference in binding energies can be attributed to the presence of three body effects,[87] as observed for argon clusters of benzene and *p*-difluorobenzene.[153,86,159]

Table 3.1: Comparison of 2CAP and VMI experimental results of anisole-methane 1:1 and 1:2 complexes. Experimental values reported to one standard deviation in parenthesis.

	Binding Energy (kJ/mol)					
	Anisole···CH$_4$ 1:1 cluster			Anisole···CH$_4$ 1:2 cluster		
Method	S_0	S_1	D_0	S_0	S_1	D_0
Experiment (2CAP)	5.8(2)	6.6(2)	9.2(2)	6.5(3)	7.2(3)	9.9(4)
Experiment (VMI)	5.8(1)	6.6(1)	9.2(1)	6.4(2)	7.1(2)	9.8(2)

3.2.4 THEORETICAL CALCULATIONS ON ANISOLE-METHANE 1:2 VAN DER WAALS CLUSTER

To support the experimental results, electronic structure calculations were performed to determine the equilibrium geometries and energetics. Representative structures of anisole-methane 1:2 complex are presented in Figure 3.1-5. Calculations at the MP2/6-311++G(3dp,3df) level of theory show three structures corresponding to a minima on the potential energy surface – two out of plane π-type geometries and one σ-type - π-type structure. Structure A, which is the global minimum, has two methane molecules occupying equivalent positions above and below the plane of the anisole ring (isotropic clusters) while structures B and C have both methane molecules on the same side of the ring (anisotropic clusters). The global minimum energy structure is consistent with the additive red–shift in the excitation spectrum of the anisole-methane 1:2 complex, which is twice that observed for the 1:1 complex. Previous studies of the 1:2 complexes of benzene and toluene with methane have also found the same type of geometries.[123,156] Due to computational constraints, we could not perform a frequency calculation for the 1:2 complex at the MP2/6-311+G(3dp,3df) level of theory. Nevertheless, our earlier study of anisole-methane 1:1 complex showed that in addition to MP2, B3LYP-D3 and M06-2X/6-311++G(3pd, 3df) levels of theory well reproduced the experimental results.
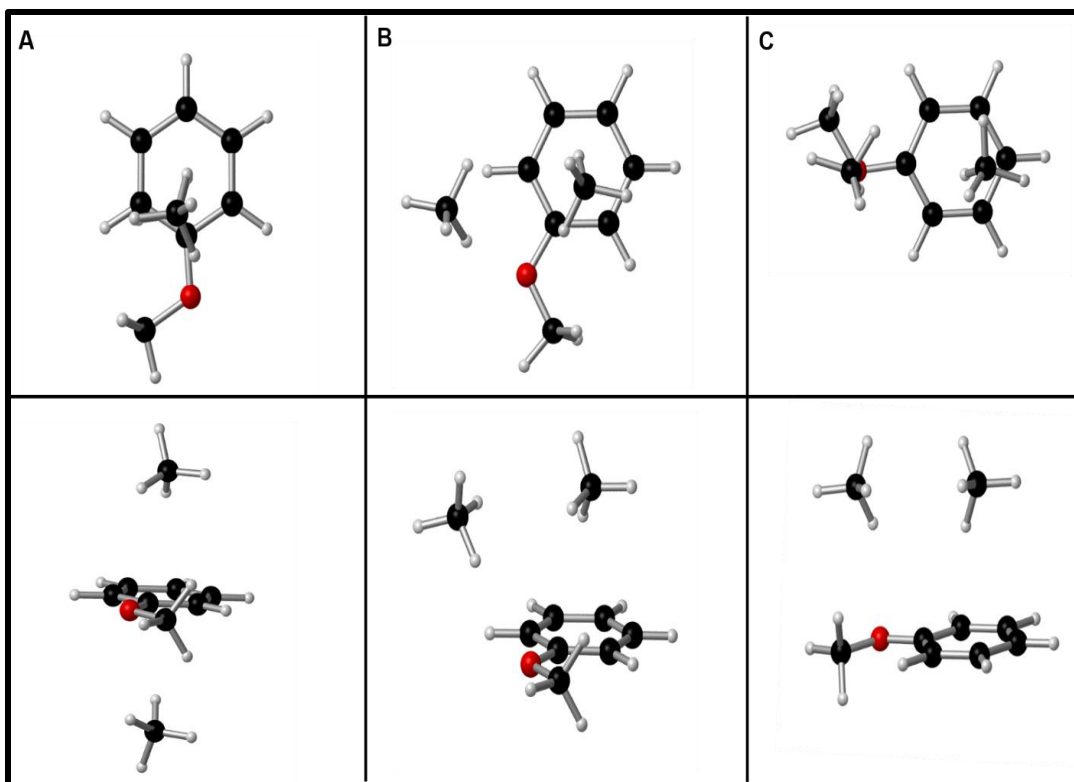
Figure 3.1-5: Comparison of the ground state optimized structures of anisole-methane 1:2 at the MP2/ 6-311++G (3df,3pd) level of theory. A = isotropic π-type geometry, B = anisotropic σ-π-type geometry and C = anisotropic π-type geometry. The upper panels give the top-down view while the lower panels give the side-on view.

Complete geometry optimizations were then carried out at various DFT methods shown in Table 3.2 and the predicted minimum energy structure was consistent with the one presented in Figure 3.1-5 A. The calculated binding energies of the anisole-methane 1:2 complex in the ground (S_0) and cation radical (D_0) states are also provided in Table 3.2. Noticeably, the B3LYP-D3 and CAMB3LYP-D3 methods underestimated the binding energies, particularly in the ground state. However, M06(2X) at both the aug-cc-pVTZ and 6-311++g(3dp,3df) basis set well reproduced the ground and excited state binding energies. The PBE0-D3 at the 6-311++g(3dp,3df) basis set was also in good

agreement with experimental binding energies and provided the best performance in both

the neutral and cation radical states at the aug-cc-pVTZ basis set.

Table 3.1: Comparison of experimental and computed binding energies for the anisole-methane 1:2 complex. Experimental values list one standard deviation in parenthesis and all DFT binding energies were corrected for zero-point energy and basis set superposition error using the counterpoise method.

Method	Binding Energy (kJ/mol)		
	S_0	S_1	D_0
Experiment (2CAP)	6.5(3)	7.2(3)	9.9(4)
Experiment (VMI)	6.4(2)	7.1(2)	9.8(2)
PBE0-D3/aug-cc-pVTZ	6.4		9.9
PBE0-D3/6-311++G(3df,3pd)	6.0		9.6
M06-2X-D3/aug-cc-pVTZ	5.8		10.2
M06-2X-D3/6-311++G(3df,3pd)	5.7		10.8
B3LYP-D3/6-311++G(3df,3pd)	4.9		9.1
CAM-B3LYP-D3/6-311++G(3df,3pd)	4.8		8.9

To gain more insight into the observed increase in binding energy of the 1:2

complex, we carried out a Mulliken map analysis on the optimized ground state structures

of anisole, anisole-methane 1:1 and 1:2 complexes, respectively at the PBE0-D3/aug-cc-

pVTZ level of theory as illustrated in Figure 3.1-6. Charges on atoms were different

across the monomer, 1:1 and 1:2 complexes and the dipole moment of the 1:2 complex

was reduced (1.1693 D) relative to that of the 1:1 (1.2344 D) and monomer (1.2841 D).

The low dipole moment is indicative of the electron density being drawn from the methoxy group to the aromatic ring.
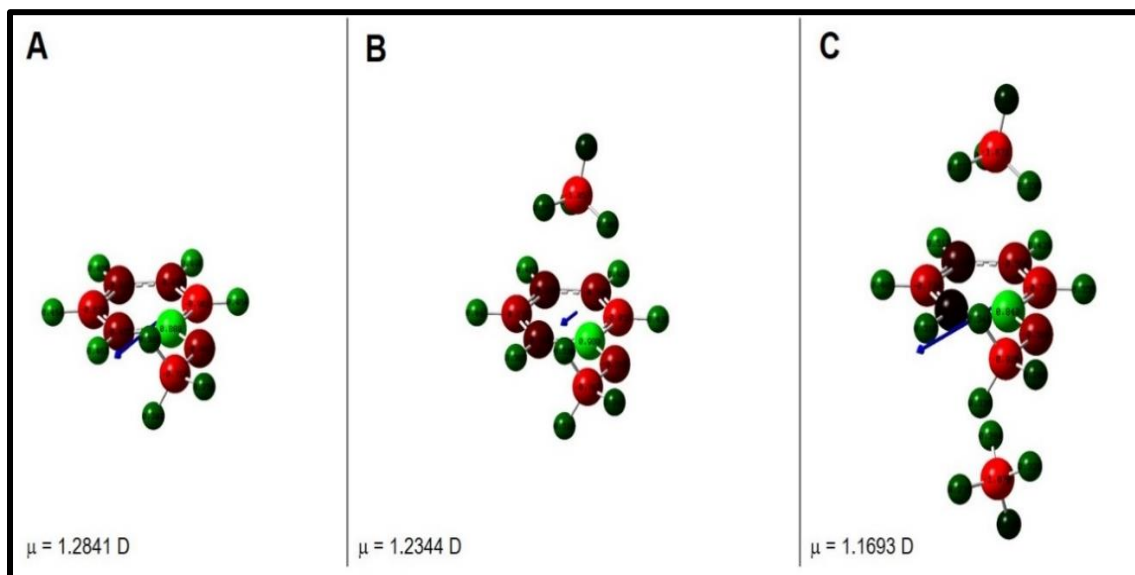
Figure 3.1-6: Predicted atomic charges from Mulliken population analysis. A = anisole, B = anisole-methane 1:1 complex and C = anisole-methane 1:2 complex at the PBE0-D3/aug-cc-pVTZ.

3.3 CONCLUSIONS ON ANISOLE-CH$_4$ 1:2 VAN DER WAALS CLUSTER

In this chapter we have presented a follow up to our work on the detection and characterization of the anisole$\cdots$CH$_4$ 1:1 complex. We have reported on the spectroscopy and precise measurement of binding energies of anisole-methane 1:2 complex in the ground (S$_0$), excited (S$_1$) and cation radical (D$_0$) states using 2CAP and VMI techniques. The global minimum structure predicted a dual mode of interaction (C-H$\cdots$O vs C-H$\cdots\pi$) on opposite faces of the aromatic ring and was consistent with the observed additive spectral red-shift, roughly twice that of the 1:1 complex origin. Binding energy data for anisole-methane 1:2 complex showed an increase with the addition of the second methane relative to the first, indicative of cooperative binding, with this trend consistent across the three electronic states. The experimental binding energies were in good agreement with a few selected DFT methods, with the PBE0-D3 providing the most accurate description across the S$_0$ and D$_0$ states. In future we plan to carry out a more comprehensive theoretical study to establish the source of the observed change in binding. One approach will be to perform an energy decomposition analysis to discern the energy terms or type of forces contributing to the increase in binding observed for the 1:2 complex of anisole-methane.

CHAPTER 4: ANILINE-CH$_4$ 1:1 AND 1:2 VAN DER WAALS CLUSTERS

This chapter will provide a discussion on prior studies on aniline-methane 1:1 complex highlighting on the major findings and ambiguous questions that remain with respect to dissociation energies in the three electronic states (S_0, S_1, D_0). The spectroscopy of 1:2 complex of aniline-methane will also be discussed. Here, we will explain in detail the experimental and theoretical results of the complexes.

4.1 BACKGROUND ON ANILINE AND PREVIOUS STUDIES OF ANILINE-CH$_4$ VAN DER WAALS CLUSTERS

Aniline is the simplest aromatic amine, and is amenable to ionization and detection via mass selective resonant two-photon ionization (R2PI) methods.[160–162] The spectroscopy of aniline in the S_0, S_1 and D_0 states has been studied in detail.[160–163] It has been firmly established that the molecule is nonplanar in the S_0 state, but becomes essentially planar in the S_1 and D_0 states due to a significant lowering of the barrier to inversion of the amino hydrogens upon electronic excitation and ionization, respectively. A variety of studies have reported on the formation and characterization of van der Waals complexes of aniline with rare gases,[164–177] small molecules,[157,178–185] and larger molecules.[186–191]

Furthermore, the homocomplexes of aniline have been studied by both infrared (IR) and R2PI spectroscopy. In chapter 2, we examined the 1:1 complex of anisole with methane,[192] where a dual modality of binding was exhibited, with the methane interacting with both the oxygen and conjugated π system through C-H$^{..}$O and C-H$^{..}$π interactions.

Like anisole, aniline possesses two sites that can act as proton acceptors, the electron lone pair on nitrogen and the conjugated π system, and thus both C-H$\cdots\pi$ and C-H$\cdots$N type of interactions can be expected for the aniline$\cdots$CH$_4$ 1:1 complex. In addition, the amino hydrogens of aniline can also afford hydrogen bonding with solvents containing O or N atoms. Unlike anisole, the planarization of the amino group which occurs upon electronic excitation or ionization of aniline may significantly impact the structure and energetics of binding in these states. We note that C-H$\cdots$N interactions have emerged as important binding motifs in molecular self-assembly, protein structure, and crystal engineering.

Prior studies have examined the spectroscopy of the aniline$\cdots$(CH$_4$)n (n=1,2) complexes; however, the dissociation energies have not been accurately determined. In 1984, Bernstein *et al*. examined the spectroscopy of the 1:1 complex and estimated an upper limit to the dissociation energy in the S$_1$ state of ~699 cm^{-1} (8.4 kJ/mol) from the onset of monomer fluorescence.[157] Later on, the same group revised this estimate downward to 480 cm^{-1} (5.7 kJ/mol) by observing the absence of higher vibronic bands from a two-color excitation spectrum, and using an RRKM model analysis to fit the observed vibrational predissociation rates.[180] Subsequently, Knee and coworkers used photoelectron spectroscopy to predict the change in dissociation energy of the aniline$\cdots$CH$_4$ complex upon ionization from IP measurements of the monomer and the complex.[181] For the D$_0$ state, the dissociation energy was predicted to increase by 169 and 92 cm^{-1}, respectively, compared to that in the S$_0$ and S$_1$ states. A later study by the Knee group which employed picosecond photoelectron spectroscopy reported a S$_1$ state dissociation energy of 450 cm^{-1} (5.4 kJ/mol) from an RRKM model analysis.[182] Thus,

some ambiguity remains concerning the dissociation energies of the 1:1 complex of aniline and methane, and a direct experimental measurement is desired.

Building upon our prior studies of related anisole-methane complexes,[192] the goal of this work is to accurately determine the dissociation energies of the aniline$\cdots$(CH$_4$)$_n$ (n=1,2) complexes in the three respective states (S$_0$, S$_1$, D$_0$). Thus, we report on measurement of the dissociation energies of the aniline$\cdots$(CH$_4$)$_n$ (n=1,2) complexes using a combination of experimental methods, including two-color R2PI or 2CR2PI, two color appearance potential measurements or 2CAP, and velocity-mapped ion imaging or VMI. Our experimental findings are compared with the results of selected theoretical (density functional theory or DFT) methods. In addition to being used as a benchmark for theoretical studies, experimental dissociation energy measurements can also afford important insights into competitive non-covalent interactions and cooperativity–i.e., how the binding of the first "solvent" molecule affects the binding of the second. In studies of anisole-methane complexes, we found that the dissociation energy of methane loss from the 1:2 complex increased by 10% with respect to that of the 1:1 complex, although both solvent molecules occupied similar sites on opposite faces of the aromatic ring. Related model systems such as the benzene and toluene$\cdots$CH$_4$ complexes have also been used to investigate such effects.[121,123,156,193–196]

4.2 EXPERIMENTAL METHODS

The experimental approach employed in this work is very similar to that described in chapter 2 for anisole-methane complexes. Briefly, it consisted of a TOF mass spectrometer equipped with a pulsed nozzle. Two frequency-doubled Nd/YAG pumped dye lasers were used for excitation and ionization of the aniline methane complex, and an 8-channel digital pulse delay generator was used for temporal control of the experiment. Aniline (99.5%, Sigma-Aldrich) soaked cotton swabs were placed in a temperature-controlled oven that was connected to the inlet of a pulsed nozzle. The oven and nozzle were heated to 60 °C to generate the aniline vapor. At this temperature, the aniline vapor pressure is roughly 6.5 Torr according to an estimate from the Antoine equation parameters.[197] A mixture of 5 % methane in Ar carrier gas at a backing pressure of 50 psi was passed through the heated oven, and the resultant gaseous mixture was injected into the TOF source chamber by a 0.8 mm diameter pulsed nozzle, forming a molecular beam. The beam passed through a 1.5 mm diameter conical nickel skimmer before entering the ionization region of the TOF. As the aniline S_1 lifetime is relatively short, or order 2-3 ns,[198,199] for all the two color experiments reported here the laser pulses were overlapped temporally. Typical laser fluences were of order 0.1 mJ, with the beams loosely focused into the ionization region using 2 m spherical lenses with resonant excitation and ionization achieved using the two frequency-doubled Nd/YAG pumped dye lasers, Sirah Cobra-Stretch and Lambda-Physik Scanmate 2E, pumped by the second harmonic of a Spectra-Physics INDI and Quantel Q-Smart 850, respectively. The ions were extracted via a three–plate stack and flew a distance of 1 m before striking a dual chevron microchannel plate detector.

Ion yield spectra for the aniline monomer, and aniline$\cdots$$CH_4$ 1:1 and 1:2 complexes, were determined by setting the pump laser (λ_1) on resonance and scanning the frequency of the second laser (λ_2) through the ionization threshold, monitoring the onset of monomer or complex ion signal. To determine the S_0 state binding energy of the 1:1 and 1:2 complexes, 2CAP measurements were performed, where the pump laser was set on resonance (λ_1) of the complex of interest and the second (ionizing) laser (λ_2) was scanned above the dissociation threshold while monitoring the mass channel of the fragment species of interest.

Velocity-mapped ion imaging experiments were carried out in a separate spectrometer which utilized the same beam conditions and laser configuration used for recording the two-color experiments described above. The counter propagating lasers intercepted the molecular beam between the repeller and extractor electrodes, downstream of the skimmer orifice. The voltages of the electrodes were tuned precisely for optimum velocity mapping conditions. During image acquisition, the rear MCP voltage was gated to monitor the species of interest. Unlike in the anisole methane complexes where the images were acquired over a 30-minute integration period, here images were collected above and below the dissociation threshold over a period of 60 minutes. Typically, 36000 laser shots were acquired, with the signal attenuated using a linear polarizer to avoid image blurring by ensuring that only a few ions were detected each shot. Images collected at energies above the dissociation threshold were background-corrected using images obtained with the second photon set below the dissociation threshold. The resultant images were inverse Abel transformed using a pBASEX algorithm in a LABVIEW coded program.

4.3 THEORETICAL METHODS

To supplement the experimental results, electronic structure calculations were performed to estimate the equilibrium geometries and energetics of aniline, aniline-methane 1:1 and 1:2 complexes using the Gaussian 09 software package. A previous study by the Reid group of dispersion dominated, fluorene based π-stacked dimers revealed that PBE0 and M06-2X density functionals augmented with Grimme's D3 dispersion term[200] well reproduced the ground state binding energy, but overestimated the binding in the excited and cation radical states.[60] In contrast, the CAM-B3LYP-D3 functional with def2-QZVPPD or 6-311++G(3df, 3pd) basis sets reproduced in the most balanced way the dissociation energies across all three states. Recently, dissociation energies calculated using various DFT and *ab initio* methods were benchmarked against experimental values for the anisole$\cdots$CH$_4$ complex in the S_0 and D_0 states, and it was found that the PBE0, CAM-B3LYP, and M06–2X methods with a 6-311++G(3pd,3df) basis set well reproduced the experimental results across the S_0 and D_0 states.[192] Accordingly, here we performed complete geometry optimizations on the aniline$\cdots$CH$_4$ complex. After optimization, vibrational frequency calculations were performed to confirm that the optimized structure(s) corresponded to minima on the potential energy surface. The derived dissociation (binding) energies were corrected for zero-point vibrational energy (ZPE). For the basis set used here (def2-QZVPPD), the basis set superposition error (BSSE) corrections were negligible (i.e., < 0.2 kJ/mol). The calculated dissociation energies were compared with experimental data from 2CAP and VMI measurements.

4.4 RESULTS AND DISCUSSION ON ANILINE-CH4 1:1 CLUSTER

4.4.1 2CR2P1 SPECTRA OF ANILINE AND ANILINE-CH$_4$ 1:1 CLUSTER

The 2CR2PI spectra of aniline monomer and 1:1 complex of aniline-methane are presented in the Figure 4.1-1. The electronic origin of the complex is red-shifted by –81 cm^{-1} with respect to the monomer origin, consistent with previous publications.[157,180–182] Often, van der Waals complexes involving a π system are more strongly bound in the excited state, and exhibit a red-shift due to the delocalization of the electronic cloud. Noticeably, the shift here is significantly larger than observed for 1:1 complexes of CH$_4$ with benzene (-41 cm^{-1}), toluene (- 43 cm^{-1}) and anisole (-64 cm^{-1}).[121,156,192]
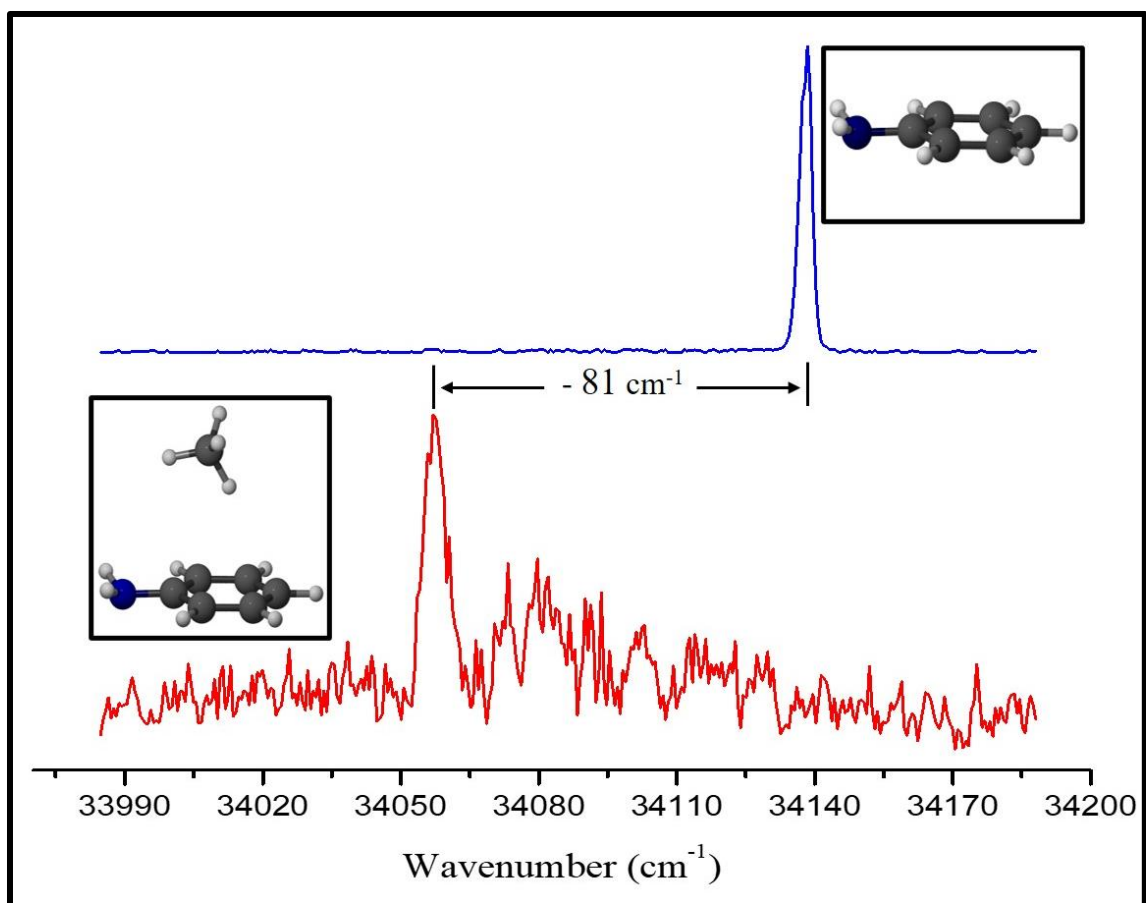
Figure 4.1-1: mass selected 2CR2P1 spectrum of aniline (blue) and aniline-methane 1:1 cluster (red).

Following measurement of the excitation spectra using a 2CR2PI scheme with a fixed ionizing photon wavelength, we then set the excitation wavelength to the respective electronic origins and measured ion yield spectra of the aniline and the aniline···CH_4 complex, to determine the respective ionization potentials shown in the upper panels of Figure 4.1-2. Relatively well defined onsets are observed from the spectra of monomer and complex, which gave the following IP values: aniline, 7.723 eV; aniline···CH_4 complex, 7.711 eV, with our measured IP values slightly higher than previous determinations, monomer (7.7206 eV) and complex (7.701 eV).[181,201] We note that our IP values are not corrected for shifts due to electric fields inevitably present in the ionization

region, as the primary focus of our measurement is the determination of dissociation

energies taken from the *difference* in IPs of the monomer and complex.
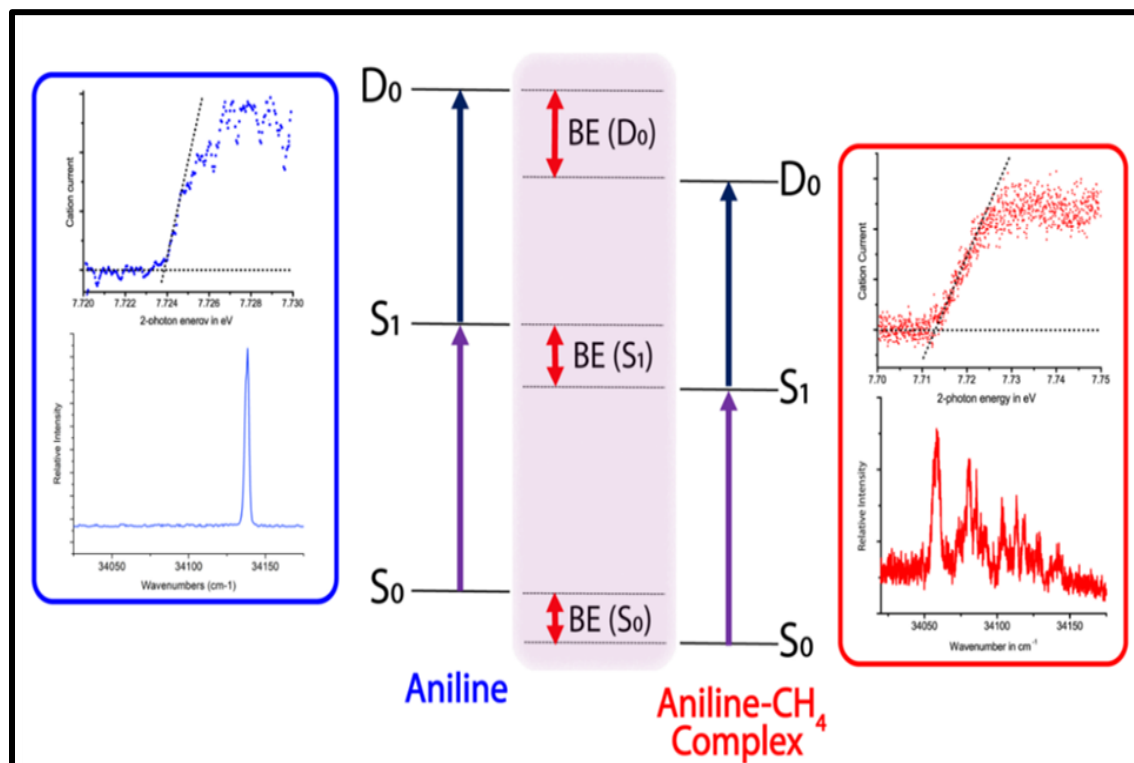
Figure 4.1-2: Spectroscopic data for aniline and aniline-methane 1:1 complex. The lower figure in each panel shows the 2CR2PI spectrum, while the upper figure in each panel displays the ion yield curve from which the ionization potential was determined. The ladder diagram links the energy levels of the monomer and complex.

4.4.2 TDDFT CALCULATIONS FOR ANILINE-CH$_4$ 1:1 CLUSTER

To assign the isomeric structure of the complex, we carried out theoretical calculations. Initial geometry optimizations were performed at the PBE0-D3/def2-TZVPPD level of theory, and subsequently refined at the PBE0-D3/def2-QZVPPD level of theory. These calculations identified two isomeric structures, and in each the methane sits above the aromatic plane Figure 4.1-3 and interacts with aniline via C-H···N and C-H···π interactions, a dual-mode of interaction similar to that observed in the anisole-methane complex. Interestingly, these calculations predict that isomer 2, where the methane sits on the same face as the amino hydrogens, is the more stable.
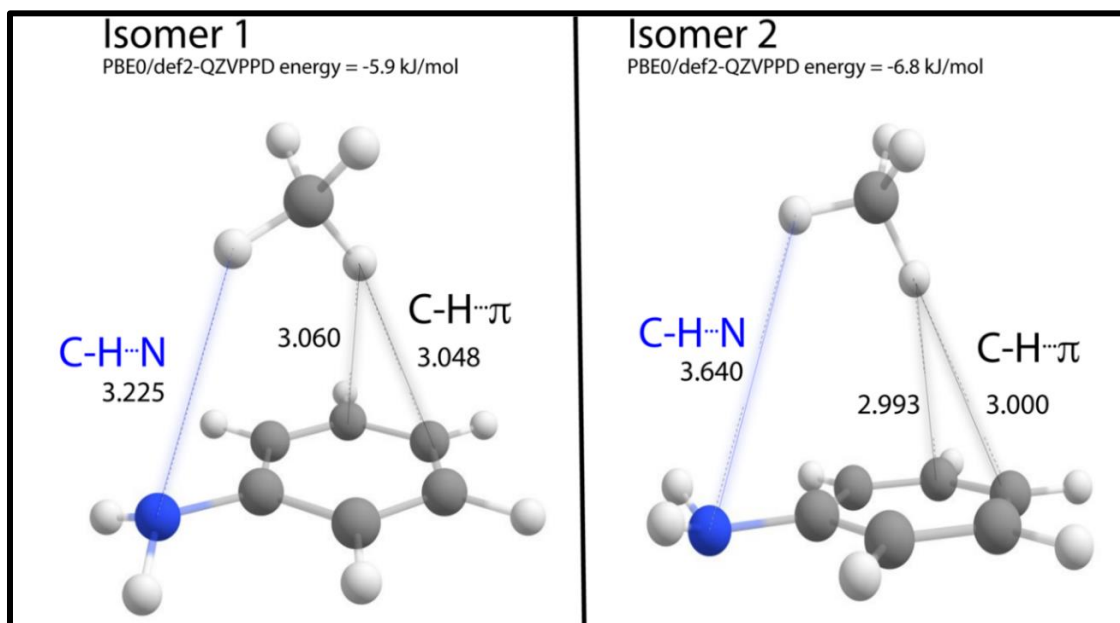
Figure 4.1-3: Isomeric structures of the aniline-methane 1:1 complex calculated at the PBE0-D3/def2-QZVPPD level of theory. The energies reflect the stabilization of the complex with respect to the isolated monomers and are corrected for ZPE. With this basis set, the BSSE correction is negligible.

To identify which isomer(s) might be contributing to the observed 2CR2PI spectrum, we performed calculations using time-dependent DFT, at the TDPBE0-D3/def2-QZVPPD level, on the PBE0-D3/def2-QZVPPD optimized ground state structures. As shown in Table 4.1, these calculations predict red-shifts of -35 and -85 cm^{-1} for isomers 1 and 2. Thus, while both isomers may contribute to the observed spectrum, it appears that the most red-shifted band is consistent with the origin of the isomeric complex 2, the most stable complex as predicted both by the calculations presented above, and additional calculations that we outline in Table 4.2. In this work, we used this feature to derive the ion yield spectra (Figure 4.1-2) and both 2CAP and VMI results presented below. Thus, for the remainder of this section we will assume that the structure of the 1:1 complex conforms to isomer 2.

Table 4.1: Predicted shifts of the S_0-S_1 electronic spectrum of the aniline-methane 1:1 complex isomers at TD PBE0-D3/def2-TZVPPD level of theory.

	Excited state (S_1) energy at TD-PBE0-D3/def2-TZVPPD		
	Energy (eV)	Energy (cm^{-1})	Shift (cm^{-1})
Isomer 1	4.8019	38730.7	-34.7
Isomer 2	4.7956	38679.9	-85.5
Aniline	4.8062	38765.4	

4.4.3 2CAP MEASUREMENTS OF ANILINE-CH$_4$ 1:1 CLUSTER

To determine the ground (S_0) state binding energy of the 1:1 complex, we performed two-color appearance potential (2CAP) measurements, which set an upper limit to the binding energy. The excitation laser was fixed on the origin of the complex, and the ionization laser scanned while monitoring the signal in the mass channel of the

aniline cation. The energetic onset of the aniline cation can be represented as the sum of the ground (S_0) state complex binding energy and the adiabatic complex ionization energy, as illustrated in Figure 4.1-4A. The 2CAP spectrum of the aniline···CH_4 1:1 complex is shown in Figure 4.1-4B, where the energy scale was determined by subtracting the monomer IP from the two-photon excitation energy, and thus provides a direct readout of the ground state dissociation energy. A clear onset representing the appearance potential was observed, and a linear extrapolation of the rising edge returns an upper limit to the S_0 state dissociation energy of 6.6(2) kJ/mol or ~550 cm^{-1}, in excellent agreement with the PBE0/def2-QZVPPD prediction for isomer 2.
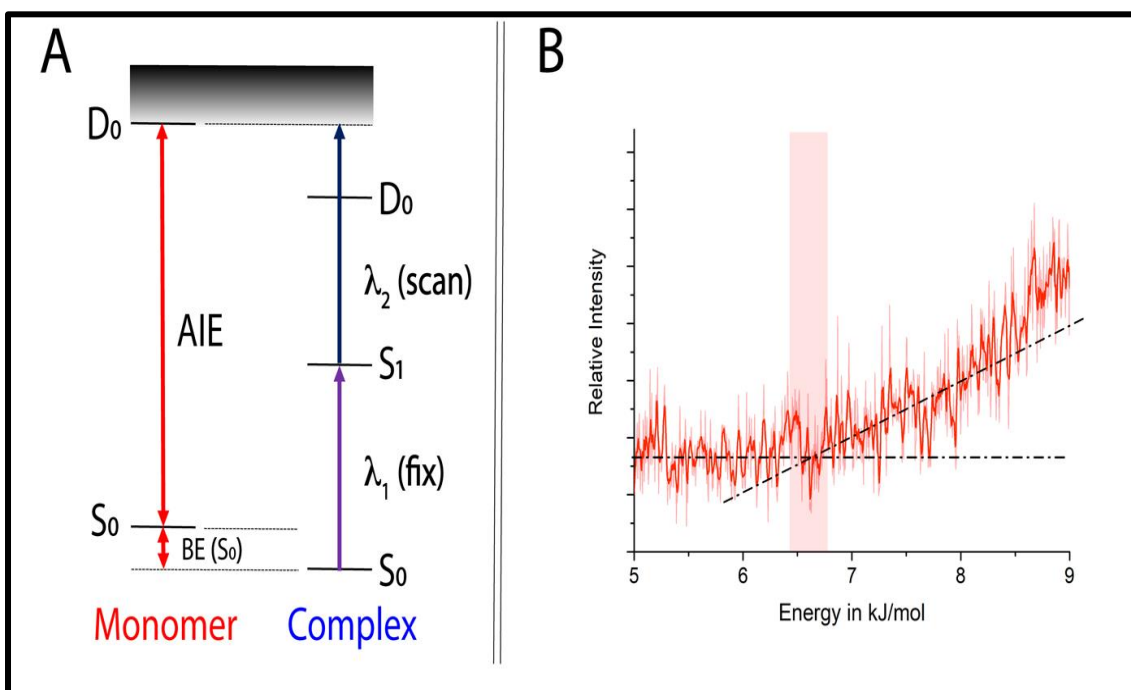
Figure 4.1-4: A: Illustration of the 2CAP method. Appearance energy of the monomer fragment is represented as the sum of ground state binding energy of the complex and adiabatic ionization energy (AIE) of the monomer. B: 2CAP spectrum of the aniline- methane complex, where the energy axis is scaled to show the ground state dissociation.

Application of the thermochemical cycle shown in Figure 4.1-2 affords the dissociation energy in the excited (S_1) and cation radical (D_0) states, presented in Table 6 in units of kJ/mol. The value derived for the S_1 state binding energy is 7.6 kJ/mol or 640 cm^{-1}. It is noteworthy that the 2CAP data show an increase in binding energies between S_0 and S_1, but a similar binding energy for S_1 and D_0.

4.4.4 VMI MEASUREMENTS OF ANILINE$\cdots$CH$_4$ 1:1 CLUSTER

In addition to the 2CAP measurements, VMI experiments were also performed. Complementary to the 2CAP results, the VMI measurements provide a direct measure of the kinetic energy release to the monomeric cation following ionization-induced fragmentation. Thus, this method can provide a direct estimate of the dissociation energy in the *cation radical state* (D_0). Shown in Figure 4.1-5 (left panel) are VMI images of the aniline cation obtained at the total (two-photon) energies shown, which span one energy below and three above the dissociation threshold of the aniline$\cdots$CH$_4$ complex. Images taken at total energies above the dissociation threshold were background subtracted and inverse Abel transformed, and the kinetic energy (KE) distributions obtained following transformation are shown in the right panel of Figure 4.1-5.
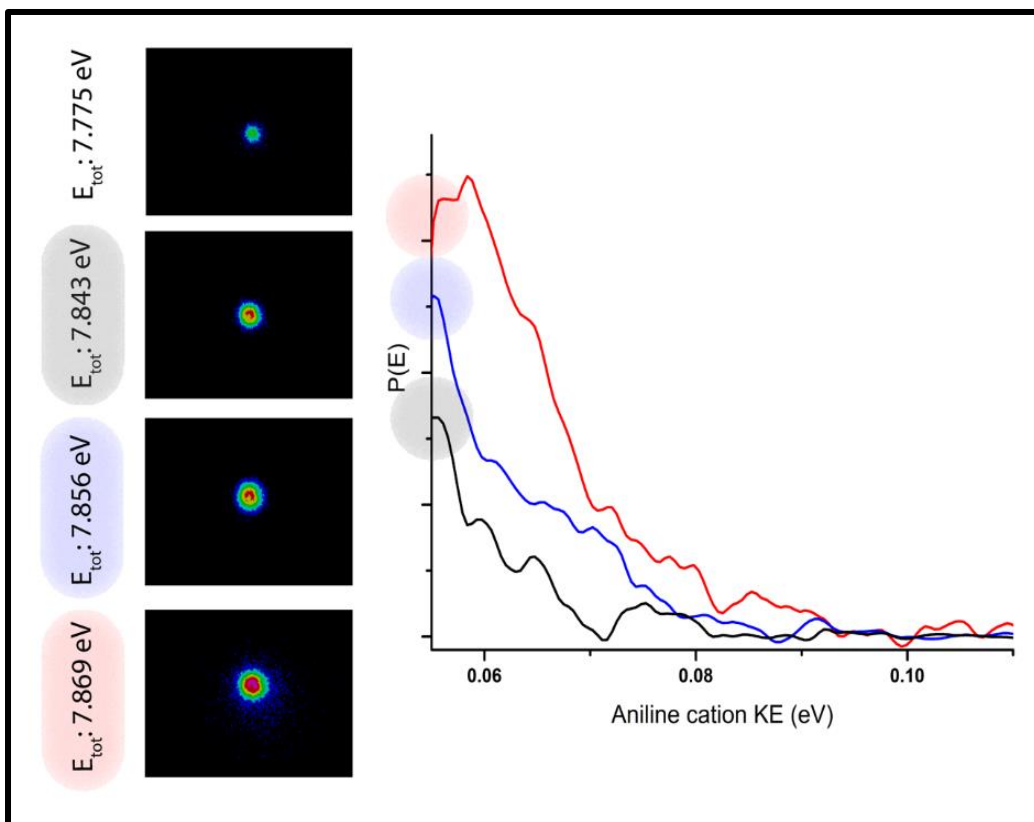
Figure 4.1-5: At left: aniline monomer ion images obtained following the dissociation of the aniline$\cdots$CH$_4$ complex at four different total energies indicated, corresponding to one energy below (top) and three above the complex dissociation threshold. The plot at right shows the P(E) distributions obtained following the transformation of the three images collected above the dissociation threshold. The maximum kinetic energy values from the plots were used to determine the D$_0$ state binding energy, as described in the text.

From the data shown in Figure 4.1-5, it is apparent that KE$_{max}$, which reflects the complex dissociation energy assuming the formation of cold (ground state) monomer cation, scales in proportion to the total energy, as expected. A dissociation energy in the D$_0$ state (9.9 kJ/mol or 830 cm^{-1}) was determined from the observed KE$_{max}$ and the total available energy and is an average of measurements taken at three different total energies. Using the energetic cycle derived from spectroscopic data in Figure 4.1-2, the dissociation energies in S$_0$ and S$_1$ were then determined, and these are provided in Table 4.2.

Unlike our prior study of anisole-methane complexes,[192] here the 2CAP and VMI experiments do not agree regarding the aniline-CH_4 dissociation energy in the D_0 state (Table 4.2). As the VMI experiments are analyzed with the assumption that KE_{max} corresponds to the formation of vibrationally cold fragments, one possible explanation for this discrepancy is the preferential formation of vibrationally excited aniline cation radical in the VMI experiments. Indeed, this was previously observed in VMI measurements of the anisole dimer.[77] The difference in D_0 state binding energy between the VMI and 2CAP result is $\sim$180 cm^{-1}, which corresponds exactly to the lowest vibrational frequency (10b) of the aniline cation, an out–of–plane NH_2 wag ring deformation. Thus, the discrepancy between the 2CAP and VMI measurements can be resolved if it is assumed that the aniline cation fragment is preferentially produced with one quantum of excitation in mode 10b following dissociation of the ionized aniline$^{..}CH_4$ complex. With this assumption, the corrected dissociation energy values are reported in Table 7, in good agreement with the 2CAP measurement. This illustrates the benefit of comparing VMI measurements with those from 2CAP (or other methods) to identify cases where dissociation preferentially populates excited vibrational states.[172]

Regarding comparison with previous experiments, these are also listed in Table 4.2. Our S_1 dissociation energy lies between the two experimental values derived by Bernstein,[157,180] and is roughly 2 kJ/mol higher than that estimated by Knee and co-workers.[182] The *difference* in S_0 and S_1 dissociation energies that we measure is in good agreement with that derived by Knee *et al.*[181]

4.4.5 THEORETICAL BINDING ENERGY CALCULATIONS

To aid in understanding the experimental results, we performed additional calculations of the complex geometry, spectroscopic properties, and dissociation energies of isomer 2, using theoretical methods including dispersion corrected single and double hybrid density functional theory methods (PBE0-D3, M06-2X-D3, Cam-B3LYP-D3) with def2-XZVPPD (X=T,Q). The calculated dissociation energies are listed in Table 4.2 and were corrected for zero-point energy (ZPE) In practice, we found that the BSSE correction was negligible (i.e, < 0.2 kJ/mol) when employing the larger basis set (def2-QZVPPD). The dissociation energies range from 6.0 to 6.9 kJ/mol, in close agreement with the 2CAP and corrected VMI estimates. For all of the theoretical methods employed, the predicted difference in energy of the two isomers was similar, of order ~ 1 kJ/mol, with isomer 2 as the global minimum energy structure.

Table 4. 2: Comparison of experimental and computed dissociation energies for aniline-methane 1:1 complex. All theoretical energies were corrected for ZPE, while the BSSE correction was negligible with the employed basis set. Unrestricted wavefunctions were employed for calculations of the cation radical state.

Method	Dissociation Energy (kJ/mol)		
	S_0	S_1	D_0
Experiment (this work, 2CAP)	6.6(3)	7.6(3)	7.8(3)
Experiment (this work VMI	8.7(2)	9.7(2)	9.9(2)
Experiment (this work, VMI	6.6(4)	7.6(2)	7.8(2)
Experiment (Bernstein *et al*, 1984)[157]		5.7-8.4	
Experiment (Bernstein *et al*, 1989)[180]	5.8	5.7	
Experiment (Zhang *et al*, 1992)[181]			S_1 DE + 1.1
Experiment (Smith *et al*, 1993)[182]		5.4	
CAM-B3LYP-D3/def2-QZVPPD	6.0	...	7.6
M06-2X-D3/def2-QZVPPD	6.2	...	7.8
PBE0-D3/def2-QZVPPD	6.9	...	8.3

Considering the D_0 state, complete geometry optimizations were performed using spin unrestricted wavefunctions, at the various levels of theory presented earlier in Table 4.2. The estimated dissociation energies were also corrected for ZPE, again the BSSE correction became insignificant with this basis set. Figure 4.1-6 compares the optimized structures of the aniline-methane 1:1 complex in the ground and cation radical states. In the later, the amide group planarizes, and the methane is shifted towards the amide substituent, and the C-H··N bond shortens than in the former. The calculated D_0 dissociation energies range from 7.6 to 8.3 kJ/mol, in excellent agreement with the experimental 2CAP and corrected VMI results.
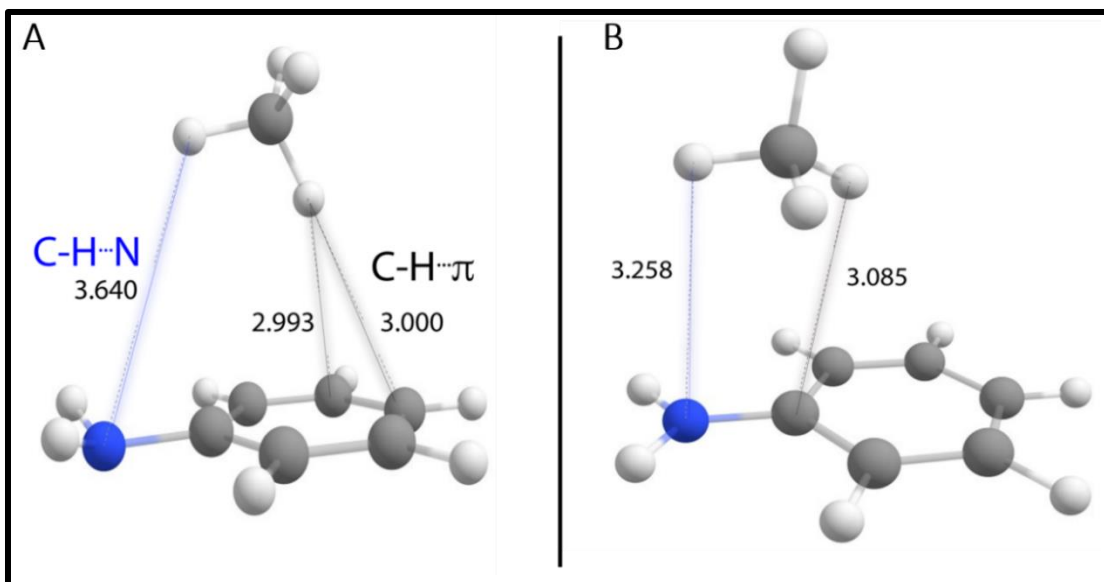
Figure 4.1-6: Optimized structure of the ground (A) and cation radical (D_0) state (B) of aniline-methane 1:1 complex at the PBE0-D3/def2-QZVPPD level of theory.

The experimental and theoretical predictions of the 1:1 complex structure are suggestive of a dual mode of non-covalent interaction (Figure 4.1-6). The measured S_0 state dissociation energy is approximately additive if we consider previously determined interaction energies for complexes exhibiting only C/H···π interactions such as benzene or toluene···CH_4 (~ 4.31–4.5 kJ/mol)[156,121] and C/H···N interactions in the prototypical ammonia···CH_4 complex (~ 2.5 kJ/mol). The experimental result suggests that the bond dissociation energy of a C-H···N type of interaction (~ 2.5 kJ/mol) is stronger than that of previously determined C-H···O interaction (~ 1 kJ/mol).[192] Considering that the electron donating, ability of aromatic substituents trends as $-NH_2$ > $-OCH_3$ > $-CH_3$, it is noteworthy that the strength of methane binding trends also in this order, as found by experiment (dissociation energies in kJ/mol: 6.6 > 5.8 > 4.5) and predicted by theory (PBE0-D3/def2-QZVPPD, in kJ/mol: 6.9 > 6.0 > 5.0).

4.5 RESULTS AND DISCUSSION ON ANILINE-CH$_4$ 1:2 VAN DER WAALS CLUSTER

4.5.1 2CR2PI SPECTRA OF ANILINE AND ANILINE-(CH$_4$)$_n$ (n=1,2) VAN DER WAALS CLUSTERS

The mass selected 2CR2PI spectra of aniline$\cdots$CH$_4$ 1:1 and 1:2 complexes are presented in Figure 4.1-7 below. The 1:2 complex spectrum is red shifted by -163 cm^{-1} with respect to the aniline monomer origin, a shift approximately twice that of the 1:1 complex (-81 cm^{-1}). A similar, nearly additive, shift has been observed in chapter 3 for anisole-methane 1:2 complex, and previously for benzene and toluene$\cdots$CH$_4$ 1:2 complexes,[121,123,156] and reflects the two solvent molecules occupying opposite positions with respect to the ring plane. Unlike the related studies of benzene and toluene$\cdots$CH$_4$ 1:2 complexes, no obvious peak corresponding to the origin of a second isomer (with the two solvent molecules on the same face of the ring) was observed within the proximity of the 1:1 complex origin.
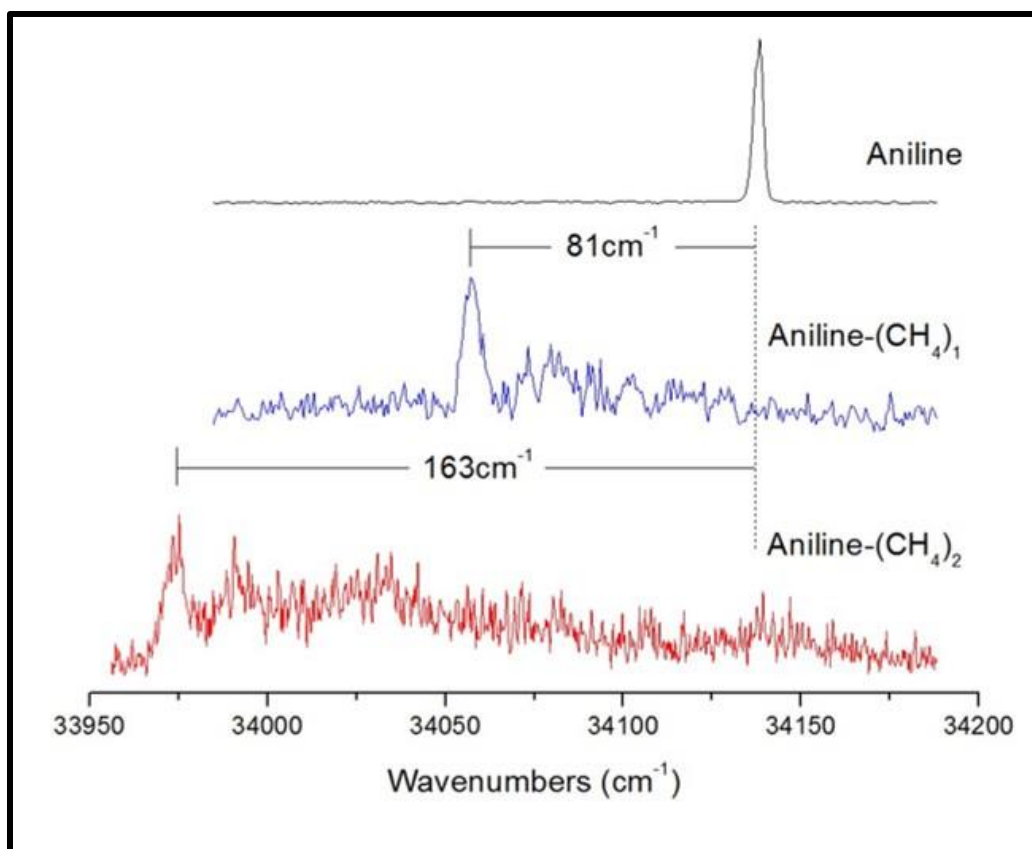
Figure 4.1-7: A comparison of mass selected 2CR2PI spectra of aniline, and aniline methane 1:1 and 1:2 clusters.

4.5.2 2CAP MEASUREMENTS OF ANILINE-CH4 1:2 CLUSTER

Figure 4.1-8 presents an overview of the spectroscopic information collected for the 1:1 and 1:2 complexes, presented with an energy ladder diagram following the mass selected 2CR2PI experiments. The electronic spectra of the complexes, recorded using 2CR2PI, are also presented in the lower panels of Figure 4.1-8, while the corresponding ion yield spectra are presented in the upper panels of Figure 4.1-8. The 1:2 complex ion yield curve is similar in shape to that of the 1:1 complex, and an ionization onset was

clearly observed around 7.688 eV, lowered as expected relative to the monomer and 1:1 complex.
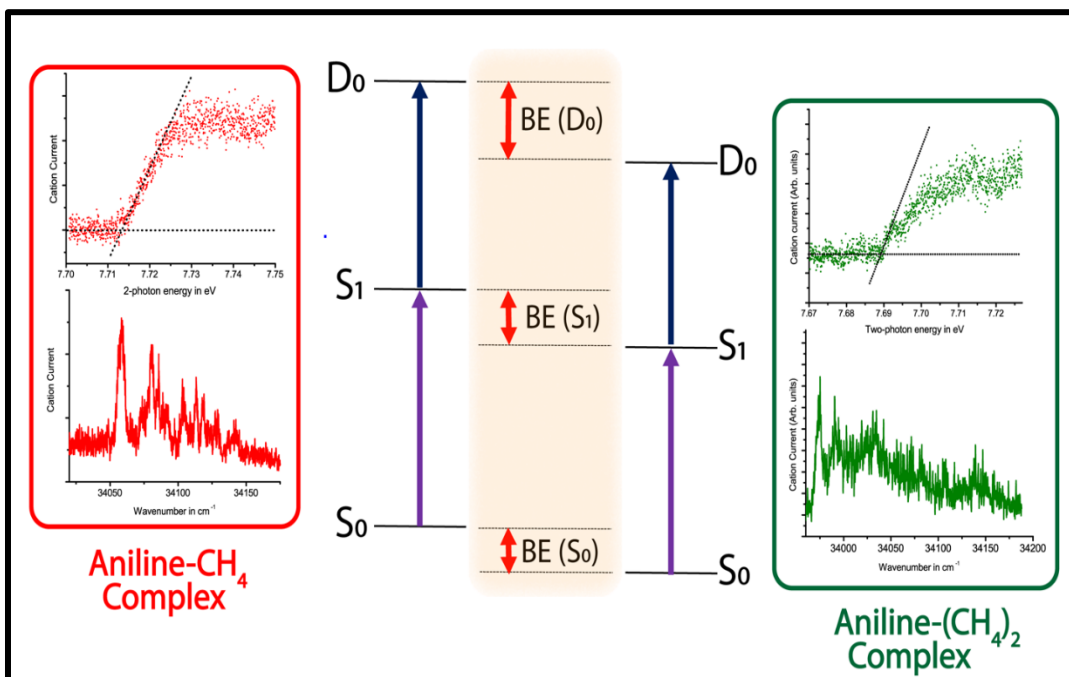
Figure 4.1-8: Spectroscopic data obtained for jet cooled aniline-methane 1:1 and 1:2 complexes, presented with an energy ladder diagram. For each species, jet-cooled electronic spectra were obtained using 2CR2PI experiments as described in the text (lower panels). Ion yield spectra, also obtained via 2CR2PI measurements with a tunable second photon, are shown in the upper panels.

To determine the experimental S_0 state dissociation energy of the 1:2 complex, 2CAP measurements were employed, as shown in Figure 4.1-9. Here, the mass channel of the (aniline$\cdots CH_4$)$^+$ fragment was monitored from dissociation of the 1:2 complex by setting the first photon on resonance with the origin of the 1:2 complex and scanning the second above the ionization threshold. As described above for the 1:1 complex, the energetic onset of fragmentation represents the sum of the S_0 state dissociation energy and the adiabatic IP of 1:1 complex. This method sets an upper limit to the ground state

dissociation energy and using the energy ladder diagram presented in Figure 4.1-8, we then obtain dissociation energies for the S_1 and D_0 states. These are given with associated uncertainties in Table 4.3, in units of kJ/mol. We note that VMI experiments for the 1:2 complex were not performed due to the heavily reduced upper state lifetime of the complex.
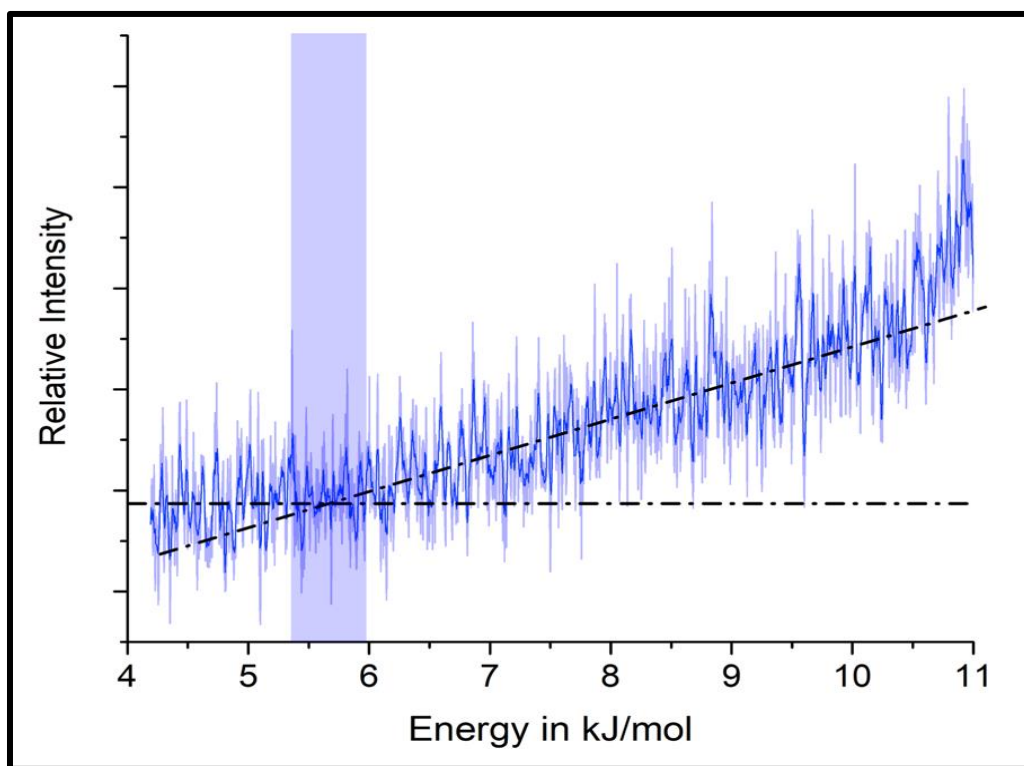
Figure 4.1-9: 2CAP measurement of aniline-methane 1:2 cluster.

In our previous study of the anisole-methane 1:2 complex, we found that the dissociation energy corresponding to loss a single methane increased by 10% with respect to the 1:1 complex across all three states (S_0, S_1, D_0). In contrast, here we find that the ground state dissociation energy of the 1:2 complex with respect to loss of one methane is decreased by ~ 10% relative to the 1:1 complex in the S_0 state. This trend is consistent

with the inequivalence of the two dissociation sites, and thus loss of the weakly bound

methane. The dissociation energy in the S_1 state is decreased by $\sim$ 10% for the 1:2

complex, while the D_0 (cation radical state) dissociation energy is similar to that found

for the 1:1 complex.

Table 4.3: Experimental dissociation energies for the aniline-methane 1:2 complex. Dissociation energies are reported to one standard deviation in parenthesis.

	Dissociation Energy (kJ/mol)					
	Aniline···CH$_4$ 1:1 cluster			Aniline···CH$_4$ 1:2 cluster		
Method	S_0	S_1	D_0	S_0	S_1	D_0
Experiment (2CAP)	6.6(3)	7.6(3)	7.8(3)	5.7(3)	6.7(3)	7.9(3)
Experiment (VMI)	6.6(2)	7.6(2)	7.8(2)	....	....	....

To gain further insight into these trends, we performed theoretical calculations on

the 1:2 complex. Calculations found two minima on the ground state PES, corresponding

to structures where the two methane molecules are on the same face or opposite faces of

the aromatic ring, respectively. The global minimum energy structure corresponded to the

latter and is illustrated in Figure 4.2-1 A. The two methane molecules do not occupy

equivalent positions in the 1:2 complex due to the presence of pyramidal amino group,

and this is further supported by the calculated interaction distances, which are different

above and below the plane of the ring. The computed ground state binding energies were

in good agreement with the observed ground state binding energies as shown in Table

4.4. The methane on the weaker binding site (same side as the amino hydrogens) is

removed first from the aniline methane 1:2 complex.
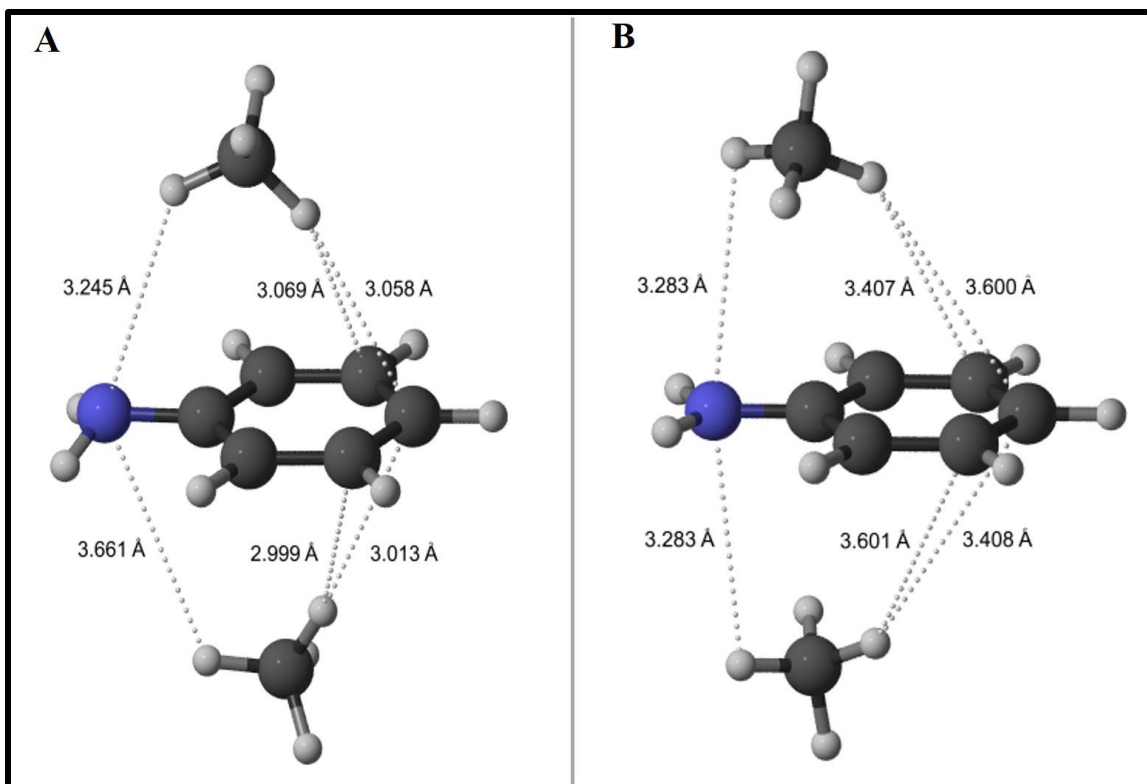
Figure 4.2-1: Comparison of the optimized ground state (S_0) and cation radical state (D_0) geometries of the aniline-methane 1:2 complex at the PBE0-D3/def2-QZVPPD and UPBE0-D3/def2-QZVPPD, respectively.

For the cation radical state, calculations performed at the (U)PBEO-D3/def2-QZVPPD level of theory predicated a geometry shown in Figure 4.2-1 B. Unlike in the ground state where the optimized structure shows the two methane solvents occupying different binding sites on opposite faces of the aromatic ring, here the predicted geometry has the two methane solvents occupying equivalent positions. This is attributed to the amino hydrogens planarizing upon excitation and subsequent ionization. This is further evidenced by the calculated interaction distances which are identical above and below the plane of the aromatic ring. The calculated dissociation energies well reproduced the experimental dissociation energies as presented in Table 4.4.

Table 4.4: Comparison of experimental and theoretical dissociation energies for aniline-methane 1:2 complex. All theoretical energies were corrected for ZPE, while the BSSE correction was negligible with the employed basis set. Unrestricted wavefunctions were employed for calculations of the cation radical state.

Method	Dissociation Energy (kJ/mol)		
	S_0	S_1	D_0
Experiment (2CAP)	5.7(3)	6.7(3)	7.9(3)
PBE0-D3/def2-QZVPPD	5.9	...	8.3
CAMB3LYP-D3/def2-QZVPPD	5.2		...
M06(2X)-D3/def2-QZVPPD	5.3		7.1

4.6 CONCLUSIONS ON ANILINE⋯$(CH_4)_n$ (n=1,2) VAN DER WAALS CLUSTERS

To probe cooperativity in C-H⋯N and C-H⋯π interactions, we have measured the dissociation energies of aniline⋯$(CH_4)_n$ (n=1,2) van der Waals complexes, in their ground (S_0), excited (S_1) and cation radical (D_0) states, using 2CAP and VMI experiments (the latter for the 1:1 complex only). The dissociation energies of the aniline⋯CH_4 1:1 complex derived from the 2CAP experiments are consistent with isomeric structure 2, where the methane sits above the aromatic ring but on the same side as the amino hydrogens and are in good agreement with a range of DFT and *ab initio* methods. We found that the VMI and 2CAP experiments were not in agreement but could be reconciled if it is assumed that dissociation of the complex in the D_0 state leads to the selective population of a low frequency inversion mode in the ionized aniline fragment, this is consistent with the expected (rigid) planarization of the amino group upon ionization. The dual mode of interaction C-H⋯π and C-H⋯N predicted by the ground state equilibrium geometry of the 1:1 complex is consistent with the large experimental

dissociation energy observed when compared to systems exhibiting only C-H$\cdots\pi$ interactions such as toluene/benzene$\cdots$CH$_4$.

Studies of the 1:2 complex show a red-shift in the S_0-S_1 spectrum which is nearly twice that observed for the 1:1 complex, suggestive of a geometry where the two methane moieties lie on opposite faces of the aromatic ring. We find that the ground state dissociation energy of the 1:2 complex with respect to loss of one methane is *decreased* by ~ 10% relative to the 1:1 complex in the S_0 and D_0 states, consistent with the solvents not occupying equivalent binding sites and loss of the weakly bound methane. The measured dissociation energies are in good agreement with theoretical expectations.

CHAPTER 5: ANISOLE-CF₃I 1:1 VAN DER WAALS CLUSTER

This following chapter focuses on a study of an experimentally characterized sigma hole interaction in a potential halogen bonded van der Waals complex. Here, a system comprised of anisole as a chromophore and trifluoroiodomethane (CF_3I) as a solvent is employed for the study of halogen bonding non-covalent interactions via mass selected R2PI experiments.

5.1 BACKGROUND ON HALOBENZENZE CLUSTERS (Ph-X) (X=F, Cl, Br, I)

In the introduction, the uniqueness of halogen bonding interactions was discussed paying attention to sigma hole interactions. Whilst fluorene is the most electronegative halogen atom, it can not form a sigma hole due to its inability to undergo sp hybridization. The ability to form a sigma bonding interaction increases in the order: $F <$ $Cl < Br < I$.[202] The size of the sigma hole on the halogen can be enhanced by introducing a strong electron withdrawing residue to the halogenated precursor.[34,138,203]

A lot of studies have focused on clusters of phenyl halides with small molecules and rare gas atoms as prototypes for halogen bonding in biological systems. For example, the Reid group previously examined mono-substituted halobenzenes (Ph-X) where X=F, Cl, Br and I) as prototypical systems, which when compared to benzene or toluene also include the potential for halogen bonding. The electronic spectra of chlorobenzene (PhCl) monomer and that of the clusters up to the tetramer were obtained with mass selected R2PI experiments supported by density functional theory (DFT) and post Hartree Fork

methods (HF). In all cases, cluster spectra were broadened, and red shifted with respect to monomer origin band. The obtained results agreed well with previous reported studies of related systems including toluene and other halo and mixed halobenzene clusters.[204,205,206,207] Following from the studies of PhCl clusters where π-π and C-H-π interactions were identified as the important binding motifs, similar work was conducted on bromobenzene (PhBr) and mixed bromobenzene clusters.[8,208] With respect to the PhCl system, the primary difference was the presence of a halogen bonded dimer where the sigma hole on Br interacted with the π cloud of the aromatic partner or alternatively with the halogen of that partner. However, these studies were hampered by the photochemistry of the aromatic chromophore as the S_1 state of the halobenzene is predissociative, crossed by a $n\sigma^*$ state that correlated with the ground state products. This was first demonstrated by Smalley and co-workers, who found that chlorobenzene and bromobenzene could be detected with nanosecond scale R2PI methods through the S_1 state.[209] However, most of the bromobenzene dissociated as this was attributed to very short excited state lifetime ~ 30 ps.[7] Building upon the studies of non-covalent interactions in chlorobenzene and bromobenzene clusters, further studies were carried out on the interactions between PhCl with ammonia (NH_3), a prototypical N atom donor.[72] The initial focus was identifying halogen bonded (donor-acceptor) complexes between the N atom donor and Cl acceptor. However, it was found based upon simulation of the electronic spectrum that the dominant structure corresponded to an in-plane σ-type complex involving a four-center interaction. This contrasted with prior studies which assumed the dominance of a π-type complex.[210] Upon ionization an intracluster reaction occurred, whereby the ammonia molecule added to the ring to form a Wheland-type intermediate. Loss of the halogen

atom or HCl led to the observed products, aniline cation radical and protonated aniline, and the relative branching between the channels was consistent with expectations based upon statistical decomposition of the intermediate. Similar studies on the PBr···NH$_3$ cluster, which showed an in-plane σ-type complex structure found out that the product branching was not statistical, with the favored channel corresponding to the formation of a Br atom and protonated aniline.[73] This result was explained with the aid of theoretical calculations, which predicted that in this case the reaction proceeded via a distonic ion radical reactive intermediate, where the radical density was localized on the Br atom, leading to the observed preference for Br atom loss.

From the reported studies, it is evident that there are limitations in utilizing halogenated aromatics.[7,8,72,73] As the size of the halogen substituent increases, the dissociation becomes too rapid for the species to be detected, and this was the case for iodobenzene. This clearly shows that phenyl halides have limited viability as chromophores for the study of weakly bound clusters.[209,208] A system composed of an aromatic donor-based chromophore (anisole) and a halomethane (CF$_3$I) has been proposed for the study of important but less frequent halogen bonding interactions (C-X···O). The O-atom donor chromophores are suitable candidates, they display longer S$_1$ lifetimes that makes them possible to analyze using the conventional spectroscopic methods (2CR2PI and LIF).[211]

5.2 RESULTS AND DISCUSSION

Mass selected 2CR2P1 spectra of anisole and anisole-CF_3I van der Waals cluster were recorded under the experimental conditions used to produce anisole-methane clusters. A premix of 5-10% CF_3I in Ar carrier gas, at a backing pressure of 20-70 psi was bubbled through liquid anisole contained in a bubbler held at -5 °C in refrigerated bath. The 2CR2PI spectra of anisole and anisole methane are shown in Figure 5.1-1. The anisole-CF_3I spectrum was obtained by scanning a wide spectral range that covered the lower and higher energy side of the anisole origin peak. The complex spectrum shows a Frank Condon maximum and structure to the blue and red of the anisole monomer origin, respectively. This makes it difficult to identify the true origin of the cluster. Furthermore, not only does CF_3I absorb light, but dissociate in the same region of the anisole monomer origin to give a broad and structureless spectrum. Multi-photon dissociation studies of CF_3I have demonstrated that the delay times between the two lasers in two color excitation schemes should be around 200-400 fs.[212] This makes it difficult to do spectroscopic analysis using the nanosecond lasers as the excited state lifetime of CF_3I is short. It may be ideal to do 1CR2PI mass spectroscopy since the 2CR2PI technique is difficult to use with such a short, excited state lifetime.
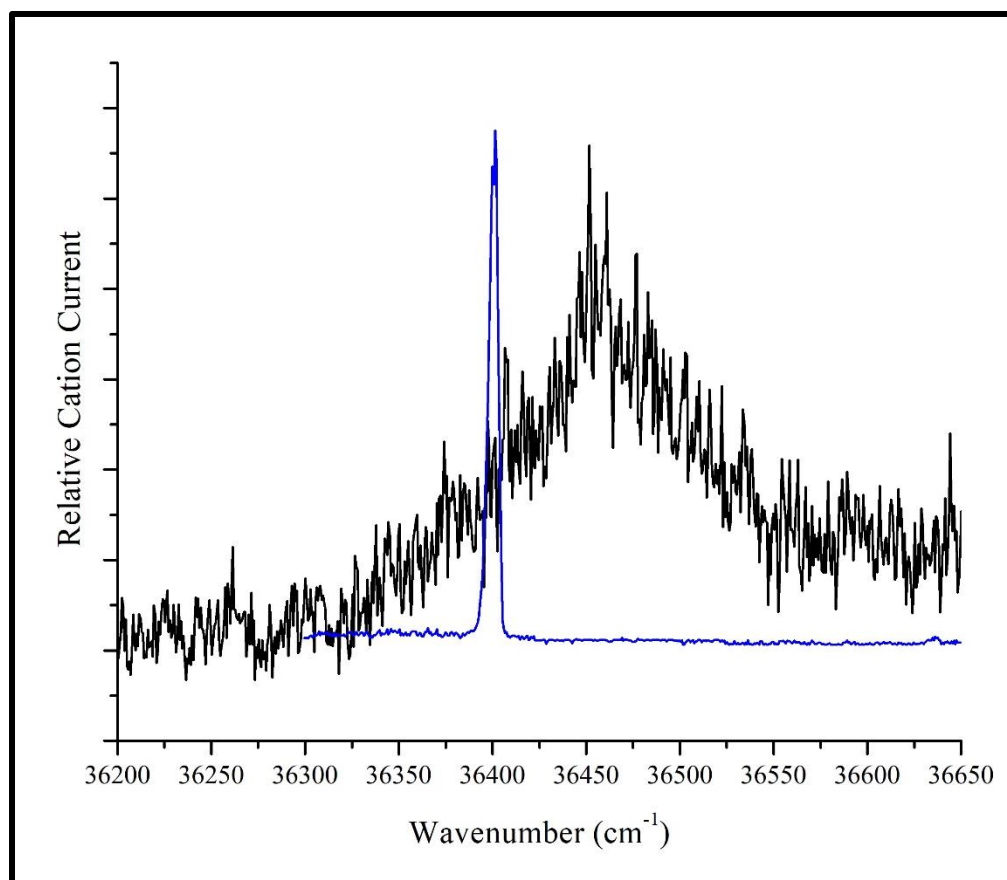
Figure 5.1-1: 2CR2PI mass spectrum of the anisole (blue) and anisole-CF_3I cluster (black).

5.3 CONCLUSIONS ON CF_3I CLUSTER AND FUTURE DIRECTIONS

This research is ongoing and, in the future, the plan is to look at much simpler systems such as the anisole-methane that do not absorb and dissociate in the monomer origin. One such system is anisole-FI, the only limitation with such a system is that iodine monofluoride (FI) gas is very expensive, hence the need to do some theoretical studies before carrying out the experiments. Preliminary theoretical results on the optimized ground state structure of anisole-FI performed at the M06-2X-D3/DGZVP level of theory are presented in Figure 5.1-2. The geometry optimization yielded eight

conformers, four in-plane bifurcated hydrogen bonded conformers (**A**, **B**, **C**, **D**) and four out of plane conformers (**E**, **F**, **G**, **H**). In all cases, the identified geometries did not involve a π interaction. The most stable structure corresponds to conformer **H** which feature a sigma hole interaction between the halogen atom, iodine and the electronegative oxygen lone pair of anisole.

FI reacted with anisole, making it difficult to do spectroscopic analysis. This research is ongoing, and part of the future work includes developing a coaxial dual pulsed nozzle to try and overcome the problem. An example of the nozzle is shown in Figure 5.1-3. In principle the dual puzzled nozzle separates the two monomer fragments long enough to ensure sufficient cooling through two body collisions before clustering can take form at the mixing stage.
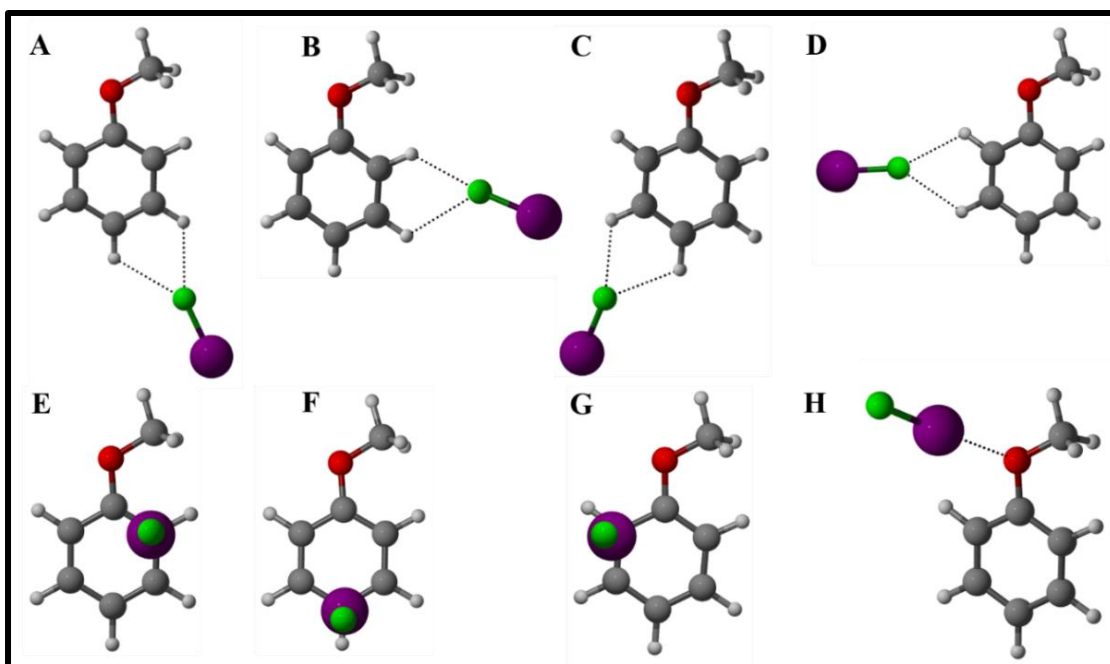
Figure 5.1-2: Optimized ground state (S_0) geometries for the anisole-FI complex at the M06(2X)-D3/DGDZVP level of theory. The most stable isomer **H** shows a sigma hole interaction in the complex.
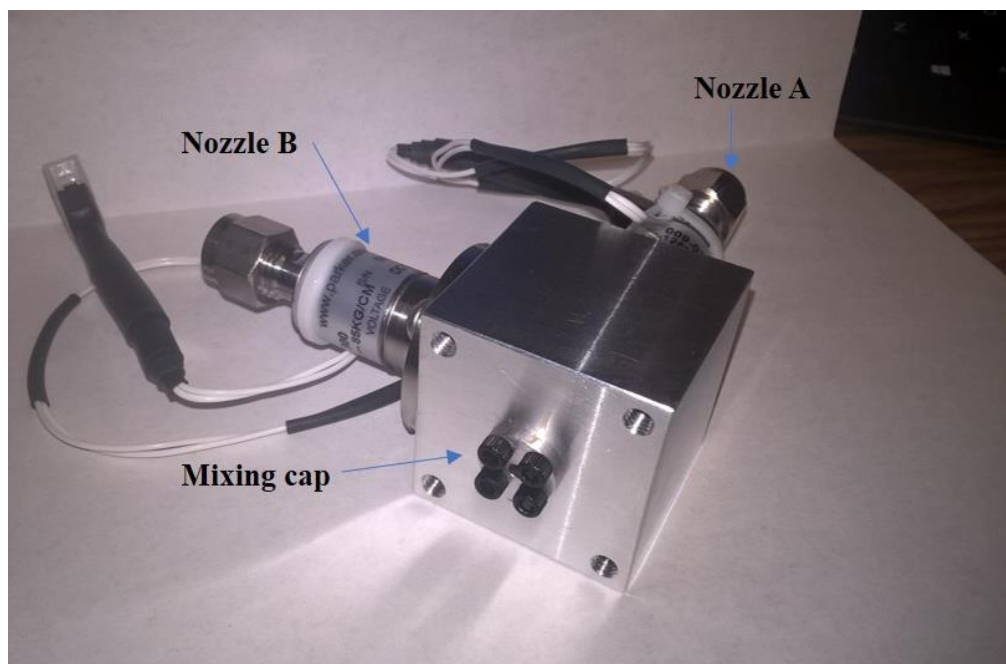
Figure 5.1-3: Dual pulsed nozzle, the respective monomers are fed separately through nozzle **A** and **B**.

CHAPTER 6: ANILINE-SO$_2$ 1:1 VAN DER WAALS CLUSTER

In chapter 5 halogen bonding was discussed as a noncovalent interaction involving a sigma hole. The following section is a continuation of a search of an experimentally characterized sigma hole interaction. Here, a system comprising of aromatic aniline and sulfur dioxide as a solvent is used to study chalcogen noncovalent interactions via mass selected REMPI spectroscopy.

6.1 BACKGROUND ON CHALCOGEN BONDED COMPLEXES OF SO$_2$

Sulfur dioxide is a prototypical molecule that offer two possible binding sites for studying different intermolecular interactions. Due to its unique structure, the cis nonbonding pair on one of the oxygens of SO$_2$ can act as an electron donor while the σ-hole on the outer surface of sulfur atom can act as an acceptor. The former results in planar hydrogen bonded dimers of SO$_2$ with molecules like HF, HCl and ClF,[43,213,214] with the latter giving rise to complexes with perpendicular geometries, stabilized by a chalcogen interaction formed between sulfur and a non-bonding pair of a Lewis base (HCN, N$_2$, CO, H$_2$O, H$_2$S, N(CH$_3$)$_3$, (CH$_3$)$_2$O).[43,215,216,217,218,219,220] The chalcogen and hydrogen bonded heterodimers have been characterized by microwave spectroscopy in a supersonic expansion. The geometries of the complexes are determined by analysis of the ground state rotational spectra with the aid of electrostatic energy calculations. Very recently, Barone *et al* investigated the sulfur dioxide-dimethyl sulfide complex using the same technique in combination with quantum chemical calculations to accurately determine the structure and energetic properties of the complex. The authors identified a

DMS···SO$_2$ complex structure which shows the two monomer units in a parallel arrangement, stabilized by a S···S noncovalent chalcogen interaction.[221]

A few studies on chalcogen bonded complexes of SO$_2$ with π electron donors also exist in literature. Kuczkowski and coworkers employed rotational spectroscopy with the aid of electrostatic energy calculations to study 1:1 complexes of SO$_2$ with ethylene (C$_2$H$_4$), acetylene (C$_2$H$_2$), cyclopropane (C$_3$H$_6$), benzene (C$_6$H$_{12}$) and furan (C$_4$H$_4$O)[222,223,224,225] In all cases, the determined structures preferred a stacked arrangement with the SO$_2$ tilted towards the π system of the electron donor, resulting in a structure stabilized by S···π chalcogen interaction. In a related study, the same group employed the same experimental and theoretical approach to study sulfur dioxide-pyridine 1:1 complex.[226] They obtained a structure similar to that observed for complexes of SO$_2$ with HCN, (CH$_3$)$_2$N and (CH$_3$)$_3$N, stabilized by a N···S interaction. Thus, utilizing aniline, a prototypical nitrogen containing chromophore and sulfur dioxide as solvent could be of great relevance in unravelling potential chalcogen noncovalent interactions between sulfur and nitrogen lone pair (N···S interaction) of the amino substituent and with the π system (π···S interaction) of aniline.

6.2 EXPERIMENTAL AND THEORETICAL METHODS

To generate the aniline-SO$_2$ 1:1 complex, a premix of 1-5 % SO$_2$ in Ar carrier gas at a backing pressure of 40 – 70 psi was passed through a heated oven containing aniline soaked cotton swabs. The rest of the experimental set up remains the same as the one detailed for the aniline- methane complexes. One color resonance two photon ionization

(ICR2PI) spectroscopy was used to excite and ionize the aniline-sulfur dioxide 1:1 complex. Due to the highly reactive nature of SO_2 with atmospheric oxygen, we observed aniline-SO_3 in the TOF mass spectrum. To make sure that the premixed gas was not contaminated with SO_3, we had to evacuate the experiment overnight, and purge with Ar carrier gas before experimentation. Ground state electronic structure calculations were performed at the PBE0 functional with def2-QZVPPD basis set and the Grimme's dispersion correction term.

6.3 RESULTS AND DISCUSSION

The observed mass selected one-color resonant two photon ionization (ICR2PI) spectrum of aniline$^{...}SO_2$ complex and a stick spectrum of aniline vibrational modes are illustrated in Figure 6.1-1. Considering the cluster spectrum, we observe three broad absorption peaks covering ~ 500 and 900 cm^{-1} to the lower and higher energy side of the aniline origin respectively. No additional peaks were observed scanning further to the red of the aniline origin. Considering the lowest energy peak red shifted by ~ 113 cm^{-1} relative to monomer origin as the cluster origin, the two peaks to the higher energy side can be ascribed to intermolecular vibration modes of aniline-sulfur dioxide complex or aniline vibrational modes built off the cluster as shown by the stick spectrum. The relative intensities of the stick spectrum were adopted from a previously reported high resolution aniline REMPI excitation spectrum.[181] Often two-color R2PI experiments produce a better resolved spectrum than one-color R2PI experiments. However, it was

difficult to perform 2CR2PI experiments due to the heavily reduced upper state lifetime
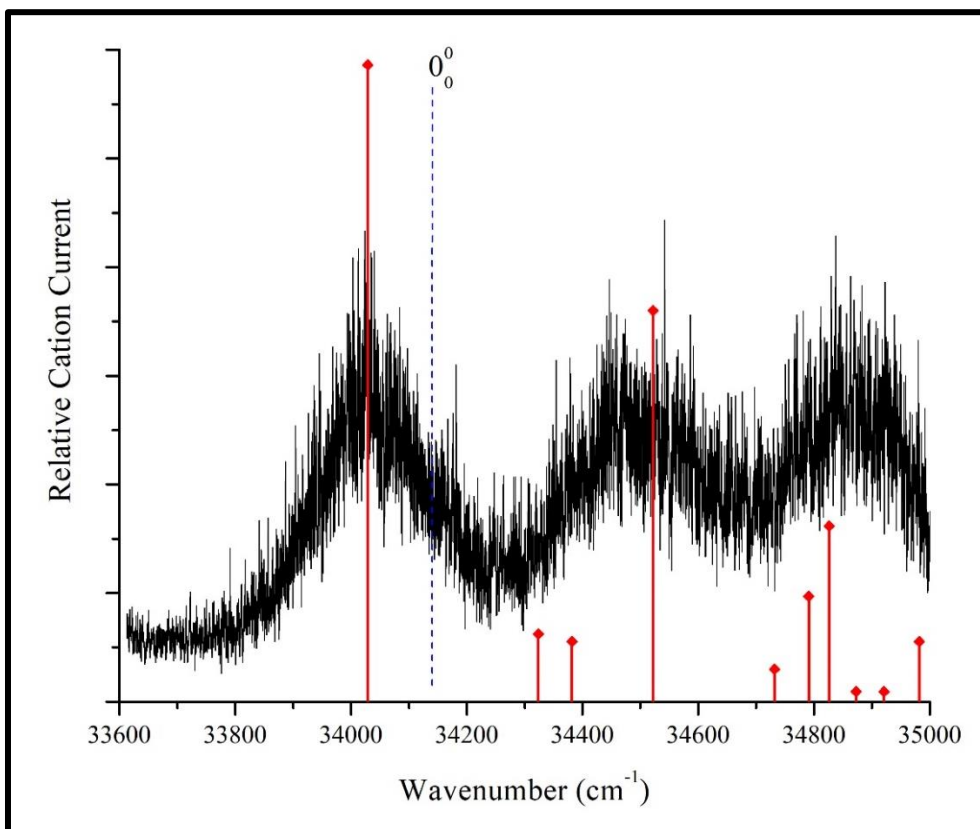
of the complex.

Figure 6.1-1: (Black) mass selected R2PI spectrum of aniline-(SO$_2$) 1:1 complex obtained by scanning the excitation laser with fixed wavelength ionization monitoring the complex mass channel. (Red) The aniline stick spectrum showing the aniline intramolecular vibrational modes. The stick spectrum and the cluster spectrum share a common origin. The dashed blue line indicates the aniline origin position.

For anisole-methane complex we observed that operating at a higher backing

pressure minimize hot bands which can lead to peak broadening. In a similar way, the

R2PI spectrum of aniline-sulfur dioxide complex was recorded at 70 psi to minimize the

effect of hot bands which can lead to peak broadening. Additional experiments were

performed to investigate on the effect of laser power (varying the power of the first

photon) on peak broadening as shown in Figure 6.1-2. The peak widths (FWHM) are all

consistent across the recorded spectra. This suggest the broadening is independent of the

power of the laser. However, other factors may contribute to the observed broadening.

The presence of multiple conformers in the molecular beam, which may absorb in the

same wavelength region as the cluster of interest. Populating a low frequency vibrational

mode of SO_2 upon excitation of cluster can also contribute towards the observed

broadening. In principle the shorter the lifetime of states involved in a transition the

broader the corresponding spectral lines. Aniline is known to have a shorter excited state

lifetime of the order of ~5 ns. The formed weakly bound aniline-sulfur dioxide complex

can result in lifetime broadening. Furthermore, the presence of very weak Franck Condon

activity in the low frequency intermolecular vibrational modes of the cluster. If the low

frequency modes are unresolved, this can result in broad features in the spectrum that are

difficult to characterize.
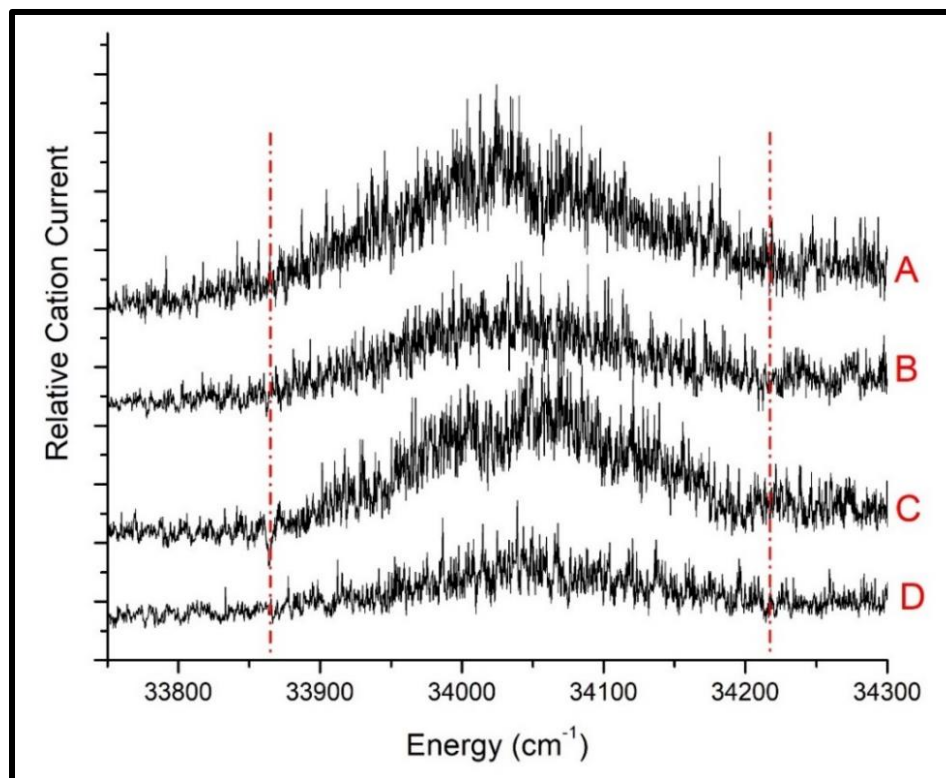
Figure 6.1-2: A and **B** one-color R2PI spectra of aniline-(SO_2) 1:1 complex with maximum power through put and with polarizer set at 90° respectively. **C** and **D** two-color R2PI spectra with polarizer set at 60° and 45° respectively.
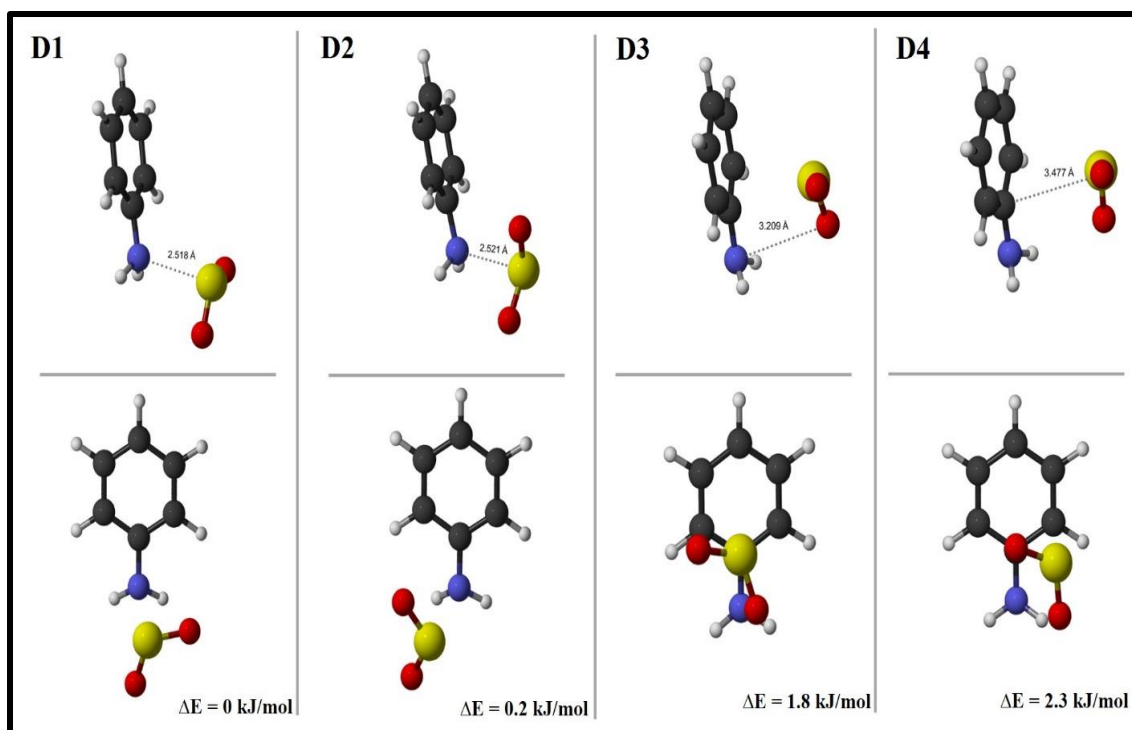
Figure 6.1-3: Ground state optimized geometries and relative energies (kJ/mol) for anisole-sulfur dioxide 1:1 complex. Upper panels show the side-on view while the lower panels show the top-down view.

The ground state optimizations yielded four conformers as shown in Figure 6.1-3. The lowest energy structure corresponds to conformer D1, which shows the sulfur dioxide tilted towards the nitrogen substituent, in a stacked arrangement that is stabilized by a N···S chalcogen interaction. This geometry is consistent with what was observed from microwave spectroscopic studies of pyridine-sulfur dioxide complex.[226] The amino group of aniline planarizes upon excitation and subsequent ionization. Due to the nature of the electronic transition (n-π*), the excited state structure is expected to be more strongly bound than the ground state, consistent with the red shift observed in the aniline-SO_2 excitation spectrum.

6.4 CONCLUSIONS ON ANILINE-SO$_2$ 1:1 VAN DER WAALS CLUSTER

This project is ongoing and additional experiments and theoretical calculations are required. For example, to gain insight on the ionization process, IP measurement of the complex can be conducted considering the lowest energy peak as the complex origin. TD-DFT calculations can be performed for aniline monomer and aniline-sulfur dioxide complex. From the TD-DFT calculations we obtain excitations energies used to calculate the relative shift which should correspond to that observed in the excitation spectrum. Furthermore, a Frank Condon analysis of the cluster spectrum can be caried out from the vibrational frequencies of the fully optimized ground state and excited state geometries to simulate the excitation spectrum. Aniline has been our prototypical nitrogen containing chromophore amenable to REMPI and Fluorescence spectroscopy. However, it has been observed the amino group planarizes upon excitation and subsequent ionization, complicating the dynamics.[227–229] In the future the same experiment can be repeated using an alternative nitrogen containing chromophore with a longer excited state lifetime. A simple system to look at will be indole⋯SO$_2$ 1:1 complex.

CHAPTER 7: TOLUENE-CH$_3$F 1:1 VAN DER WAALS CLUSTER

In the previous chapters anisole and aniline$\cdots$CH$_4$ van der Waals clusters were studied, where a decrease in binding of the order: C-H$\cdots$N > C-H$\cdots$O > C-H$\cdots\pi$ was observed. In the same context, a theoretical study is carried out on another class of hydrogen bonding interactions involving Fluorine. Here, Toluene$\cdots$CH$_3$F 1:1 complex was used as a model system to probe C-H$\cdots$F non-covalent interactions. Due to unexpected circumstances, experimental investigations of the 1:1 complex of Toluene$\cdots$CH$_3$F were not performed.

7.1 BACKGROUND ON FLUORINATED AROMATIC VAN DER WAALS CLUSTERS

In chapter 5 halogen bonding was discussed as a type of noncovalent interaction arising from the anisotropic electronic distribution on the surface of a covalently bonded halogen atom. Fluorine as a halogen atom is not involved in halogen bonding due to its low polarizability. However, fluorine is believed to form weak hydrogen bonding interactions with various proton donors. Whilst some researchers have found no evidence of fluorine involvement in hydrogen bonding,[230,231] such interactions have been identified in organic crystals. For example, a recent survey of protein ligand interactions showed weak hydrogen contacts between fluorine and positively charged carbon amides C=O groups.[232] Also, the C-H$\cdots$F interactions have been identified in nucleic acid derivatives.[233,234] The fluorine atom has tremendous influence on properties of many compounds. Fluorine is widely used in medicinal chemistry to improve on molecules

potency, permeability, modulation of pKa, and lipophilicity as well as the control of conformation.[235]

Gas phase spectroscopic studies in combination with theory have been conducted to understand the structure and bonding of fluorine hydrogen bonded interactions in aromatic van der Waals complexes. In 1999, Hobza *et al*.[236] employed double resonance ion depletion (IR/UV) spectroscopy supplemented by *ab initio* studies to characterize the weakly bound fluorobenzene$\cdots$CHCl$_3$ 1:1 complex. Calculations performed at the MP2 level of theory with 6-311g* and 6-311g** basis sets identified three isomers on the ground state potential energy surface. The global minimum geometry is an out of plane structure stabilized by a C-H$\cdots\pi$ interaction, with a binding energy of 2.5 kcal/mol. The second conformer was characterized by an in-plane C-F$\cdots$H-C contact with a binding energy of 1.7 kcal/mol. The least stable conformer is characterized by an out of plane structure with the chlorine of chloroform pointing directly to the π system of fluorobenzene forming a C-Cl$\cdots\pi$ interaction and had a binding energy of 0.7 kcal/mol. The same group[237] performed a similar study on a related 1:1 complex of fluorobenzene$\cdots$CHF$_3$. Two isomers were identified for the ground state structure. The C-H$\cdots\pi$ bound structure was the most stable isomer and had the most-blue shifted C-H vibrational frequency shift when compared to that of the least stable in-plane C-H$\cdots$F isomer. In another study, Cockett and coworkers used REMPI spectroscopy augmented by *ab initio* calculations to investigate the effect of electron withdrawing and donating groups in stabilizing different conformers. They determined a fluorobenzene-ammonia complex which feature two in-plane hydrogen interactions, one between ammonia hydrogen and fluorine atom (N-H$\cdots$F interaction), and a second between the lone pair on

ammonia nitrogen and a ring hydrogen ortho to the fluorine substituent (C-H⋯N). In a later study[238] the same group investigated on 4-fluorotoluene-ammonia complex by IR-UV depletion spectroscopy and hole burning spectroscopy, supplemented by *ab initio* and DFT calculations. The R2PI spectrum of 4-fluorotoluene-ammonia 1:1 complex had two complex origin bands, one red shifted, and the other blue shifted with respect to 4-fluorotoluene origin transition. The blue shifted band corresponded to a structure in which the NH_3 solvent was bound in plane to the hydrogen meta to the methyl group (C-H⋯N interaction), and with the fluorene of 4-fluorotoluene (N-H⋯F interaction). The red shifted band was assigned to an out of plane structure with ammonia positioned above the ring, forming two weak interactions, one between a hydrogen of ammonia and the π system (N-H⋯π interaction) and the other between ammonia nitrogen lone pair and an acidic hydrogen of the methyl substituent (C-H⋯N) interaction). In a similar study, the Buchhold group[239] investigated 1:1 complexes of fluorobenzene and difluorobenzene with methanol. Two hydrogen bonded conformers were predicted, one was an out of plane structure featuring an O-H⋯π, The other was an in-plane conformer with two hydrogen bonding interactions, one involved fluorine as a proton acceptor (O-H⋯F interaction) and the other was between the aromatic ring C-H and the solvent oxygen (C-H⋯O interaction).

In the same context, a preliminary theoretical investigation is carried out to determine the geometries and binding energies of toluene⋯CH_3F 1:1 complex in the ground and cation radical state using single hybrid DFT methods benchmarked from prior studies of complexes of anisole and aniline with methane. Here we observe a ground state structure stabilized by both C-H⋯π and C-H⋯F binding motifs. An increase in binding is

observed relative to that of toluene-methane and benzene-methane systems. Also, to gain insight on the complex ionization process, the binding energy and geometry for the complex were predicted for the cation radical state. A three-fold increase in binding is observed relative to the predicted ground state binding energy.

7.2 THEORETICAL METHODS

All calculations were performed using Gaussian 09 suite of chemistry programs on the Pere supercomputing cluster. DFT single hybrid methods (B3LYP, PBE0 and M06-2X) in combination with def2-QZVPPD basis set have been used for the preliminary investigation. The choice of methods was based on their previous success with other related hydrogen bonded complexes.

In search of the global minimum structure, optimizations and frequency calculations were performed for the toluene and CH_3F monomers using the tight convergence procedure. The vibrational frequency calculations were performed to confirm the structures were true minima on the potential energy surface. The same procedure was then used for the optimization and frequency calculations of the toluene$\cdots$$CH_3F$ 1:1 complex. Binding energy calculations were performed by considering the complex energy and the respective individual monomer energies. With the size of basis set employed, the basis set superposition error (BSSE) was negligible, and all calculated binding energies were corrected for zero-point energy (ZPE).

For the cation radical state calculations, spin unrestricted wave factions were employed. The same levels of theory, basis set and dispersion correction term as the

ground state were used. Optimization and frequency calculations were performed on both

the toluene and CH$_3$F monomers. This was followed by optimizations and frequency

calculation of the ionized toluene -fluoromethane 1:1 complex. The binding energies

were computed using the same method of analysis as the ground state structures.

7.3 RESULTS AND DISCUSSION

In search of the global minimum structure, optimizations were carried out from a

variety of initial configurations which included sampling of out of plane and in plane

interactions. Three isomers were identified for the ground state structure of toluene$^{..}$CH$_3$F

1:1 complex as shown in Figure 7.1-1. The global minimum structure corresponds to an

out of plane isomer **A** which feature a dual mode of interaction between the solvent

hydrogen and the aromatic ring system (C-H$^{..}\pi$ interaction), and between an acidic

hydrogen of the methoxy substituent of the aromatic ring and fluorine of the solvent (C-

H$^{..}$F interaction). It should be mentioned that the in-plane structure optimizations

performed starting with fluorine pointing directly to the meta and para hydrogens of

toluene converged to bifurcated hydrogen bonded isomers, where the interactions are

between fluorine and two neighboring aromatic ring hydrogens (C-H$^{..}$F interaction). The

bifurcated isomers **B** and **C** are less bound by 3.8 and 4.0 kJ/mol relative to the most

stable isomer **A**. An in-plane optimization started with fluorine pointing at the ortho

hydrogen converged to a geometry identical to that of isomer **A**.
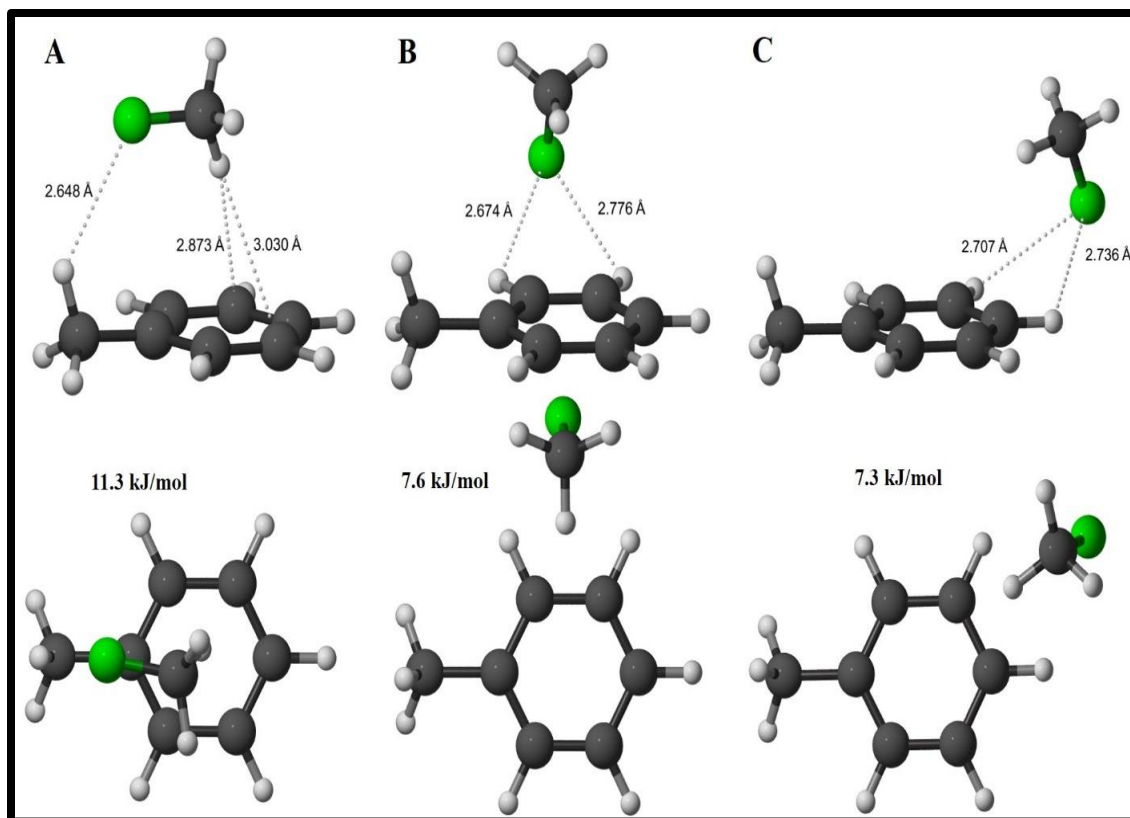
Figure 7.1-1: Optimized ground state structures of Toluene···CH$_3$F 1:1 complex and their corresponding binding energies computed at the B3LYP-D3/def2-QZVPPD level of theory. The binding energies were ZPE corrected and the BSSE is negligible at the basis set employed. All structures were determined to be minima at this level of theory with conformer **A** as the global minimum structure.

The calculated ground state binding energies, and the C-H···F-C and C···F-C interaction distances for the most stable isomer of Toluene···CH$_3$F 1:1 complex are included in Table 7.1. The binding energies agreed very well, and the structures were consistent across the methods. There are no previous reported experimental binding energy values of the complex to benchmark the theoretical values. However, an increase in binding (~7.0 kJ/mol) is observed on comparison with that previously determined for toluene···CH$_4$ 1:1 complex (~ 4.5 kJ/mol).Considering how the selected DFT methods were good at estimating the experimental ground state binding energies of for the weakly bound 1:1 complexes of methane with anisole and aniline, they should also give a good

approximation of the ground state binding energy for toluene-methane complex. We note

that some values are missing from Table 7.1. Optimization of the complex in the cation

radical state at the M06-2X-D/def2-QZVPPD gave an imaginary value for the lowest

vibrational frequency mode.

Table 7.1: Comparison of the S_0 and D_0 binding energies and interaction distances. The binding energy values were corrected for ZPE.

	Toluene···CH$_3$F Binding Energies and Interaction Distances				
Method	S_0	C-H···F (Å)	D_0	C-H···F (Å)	F···C (Å)
B3LYP-D3/def2-QZVPPD	11.3	2.569	32.1	2.390	2.844
CAM-B3LYP-D3/def2-QZVPPD	11.8	2.512	33.5	2.392	2.799
PBE0-D3/def2-QZVPPD	11.6	2.648	30.5	2.411	2.822
M06-2X-D3/def2-QZVPPD	12.2	2.554	...	....	.....

For a normal hydrogen bonded system like the water dimer, the O-H covalent

bond is characterized by a red shift in stretching vibrational frequency and bond

elongation. However, for weak hydrogen bonding interactions like C-H···N, C-H···O and

C-H···π interactions, the opposite is true. An internal geometry analysis was performed for

the bonds involved in the interaction before and after complexation as shown in Table

7.2. Similar to fluoromethane dimer,[240] we observe an elongation of C-F bond length by

~0.0047 Å, and a contraction in C-H bond length by ~0.0006 Å which is characteristic of

a weak but very important non-conventional hydrogen bonding interaction .

Table 7.2: Internal bond length analysis of the bonds directly involved in C-H··F interaction before and after complexation at the PBE0-D3/def2-QZVPPD level of theory.

Covalent bond	Bond length before	Bond length after
C-H	1.0933	1.0927
C-F	1.3776	1.3823

The predicted cation radical state structure is illustrated in Figure 7.1-2. There is a geometry change relative to the ground state structure. The solvent shifts to a position where the electronegative fluorine points directly to the electropositive alpha carbon leading to a C··F interaction. In this position, fluorine can also possibly interact with the nearby acidic hydrogen of the methyl substituent forming a C-H··F interaction. The computed binding energies are shown in Table 7.1. They range from ~ 30 - 32 kJ/mol and are in reasonable agreement between methods. A threefold increase in binding is observed and can be attributed to the stabilization of the complex by both C-H··F and C··F interactions in the ionized state.
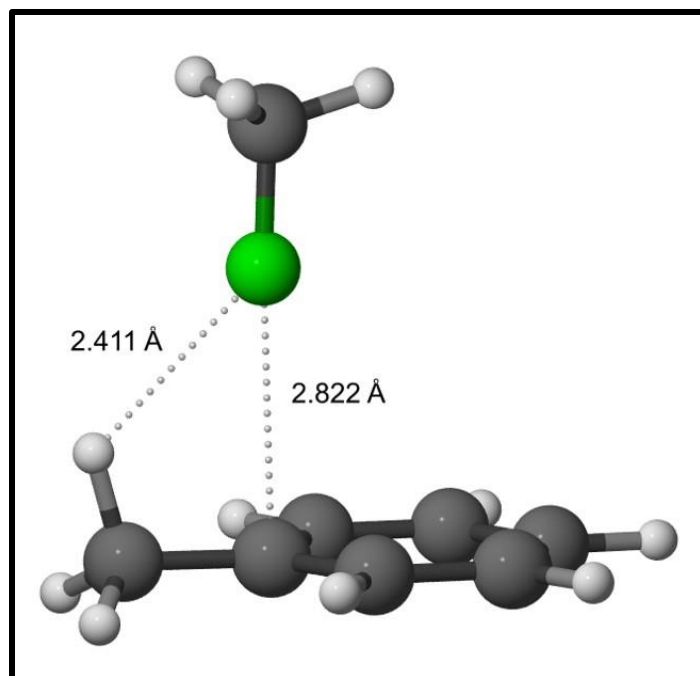
Figure 7.1-2: The calculated cation radical structure for toluene···CH₃F 1:1 complex at PBE0-D3/def2-QZVPPD level of theory.

To gain more insight into the cation radical state structure, a Mulliken charge analysis was performed at the PBE0-D3/def2-QZVPPD level of theory. From the result presented in Figure 7.1-3, we observe the electronegative fluorine interacting directly with the most electropositive alpha carbon. Furthermore, the electronegative fluorine is also in proximity to the most acidic hydrogen of the methyl substituent which supports the presence of a possible C-H···F interaction.
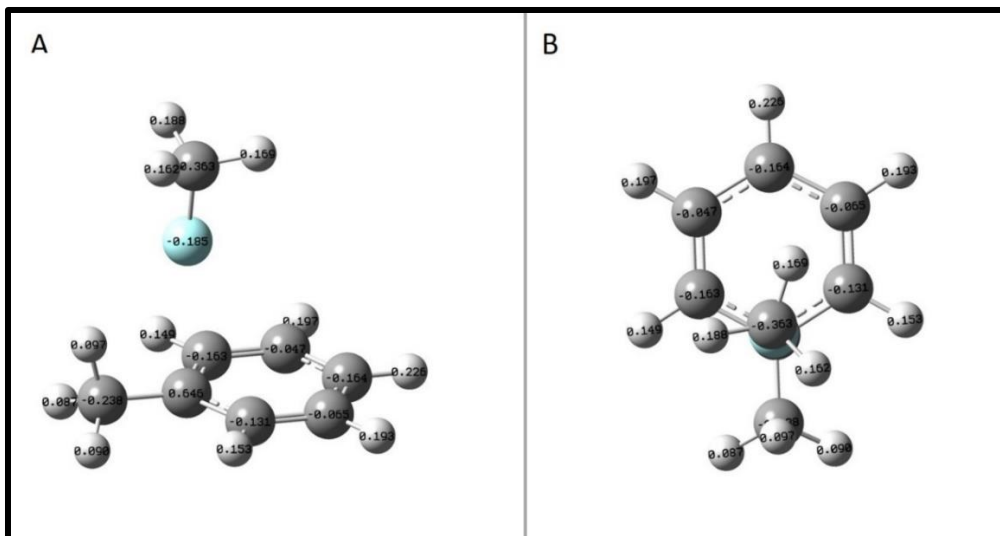
Figure 7.1-3: The Mulliken Map analysis for toluene$\cdots$CH$_3$F cation radical structure at the PBE0-D3/def2-QZVPPD. **A** is the side on view and **B** is the top view.

7.4 CONCLUSIONS ON TOLUENE-CH$_3$F 1:1 VAN DER WAALS CLUSTER

With the assumption that the selected DFT methods reproduce accurately the structure of the ground and cation radical state similar to what was observed for anisole and aniline-methane 1:1 and 1:2 complexes, the reported binding energy values should give a good approximation for the true binding energies. The objective of this theoretical study was to advance our knowledge on understanding C-H$\cdots$F-C interactions. However, experimental work should be carried out to supplement the computational results. The experimental binding energies in the ground, excited and cation radical states should be determined using two color appearance potential (2CAP) experiments and Velocity Ion Imaging (VMI) spectroscopy. Also, Hole burning (UV/UV) experiments can be carried out to discern between the different conformers predicted for the ground state structure which may be present in the molecular beam and can contribute to the excitation spectrum.

REFERENCES

(1)   Muller-Dethlefs, K.; Hobza, P. Noncovalent Interactions : A Challenge for Experiment and Theory. *Chemical Reviews* **2000**, *100*, 143–167.

(2)   Hobza, P.; Zahradník, R.; Müller-Dethlefs, K. The World of Non-Covalent Interactions: 2006. *Collection of Czechoslovak Chemical Communications* **2006**, *71* (4), 443–531.

(3)   Armstrong, K. M.; Fairman, R.; Baldwin, R. L. The (i, I+4) Phe-His Interaction Studied in an Alanine-Based α-Helix. *Journal of Molecular Biology* **1993**, *230* (1), 284–291.

(4)   Morita, S. I.; Fujii, A.; Mikami, N.; Tsuzuki, S. Origin of the Attraction in Aliphatic C-H/π Interactions: Infrared Spectroscopic and Theoretical Characterizationof Gas-Phase Clusters of Aromatics with Methane. *Journal of Physical Chemistry A* **2006**, *110* (36), 10583–10590.

(5)   Law, K. S.; Schauer, M.; Bernstein, E. R. Dimers of Aromatic Molecules: (Benzene)$_2$, (Toluene)$_2$, and Benzene-Toluene. *The Journal of Chemical Physics* **1984**, *81* (11), 4871–4882.

(6)   Yamamoto, N.; Hino, K.; Mogi, K.; Ohashi, K.; Sakai, Y.; Sekiya, H. Hole-Burning Spectroscopy and Ab Initio Calculations for the Aniline Dimer. *Chemical Physics Letters* **2001**, *342* (3–4), 417–424.

(7)   Muzangwa, L.; Nyambo, S.; Uhler, B.; Reid, S. A. On π-Stacking, C-H/π, and Halogen Bonding Interactions in Halobenzene Clusters: Resonant Two-Photon Ionization Studies of Chlorobenzene. *Journal of Chemical Physics* **2012**, *137* (18), 1–9.

(8)   Reid, S. A.; Nyambo, S.; Muzangwa, L.; Uhler, B. π-Stacking, C-H/π, and Halogen Bonding Interactions in Bromobenzene and Mixed Bromobenzene-Benzene Clusters. *Journal of Physical Chemistry A* **2013**, *117* (50), 13556–13563.

(9)   Clark, T. σ-Holes. *Wiley Interdisciplinary Reviews: Computational Molecular Science* **2013**, *3* (1), 13–20.

(10)   Shields, Z. P.; Murray, J. S.; Politzer, P. Directional Tendencies of Halogen and Hydrogen Bonds. *International Journal of Quantum Chemistry* **2010**, *110* (15), 2823–2832.

(11)   Perrin, C. L. Hydrogen Bonding: A Theoretical Perspective. *Journal of the American Chemical Society* **1998**, *120* (35), 9117–9118.

(12)   Steiner, T.; Desiraju, G. R. Distinction between the Weak Hydrogen Bond and the van der Waals Interaction. *Chemical Communications* **1998**, *1* (8), 891–892.

(13)   Steiner, T. Donor and Acceptor Strengths in C–H···O Hydrogen Bonds Quantified from Crystallographic Data of Small Solvent Molecules. *New Journal of Chemistry* **1998**, *22* (10), 1099–1103.

(14)   Aakeröy, C. B.; Evans, T. A.; Seddon, K. R.; Pálinkó, I. The C–H···Cl Hydrogen Bond: Does It Exist? *New Journal of Chemistry* **1999**, *23* (2), 145–152.

(15)   Road, H. The Role of Aromatic Rings as Hydrogen-Bond Acceptors in Molecular

Recognition. *Philosophical Transactions of the Royal Society of London. Series A: Physical and Engineering Sciences* **1993**, *345* (1674), 105–112.

(16) Shi, T.; Ge, J.; Guo, J.; Zhu, Q. The Ionization and Dissociation Mechanisms of Pyridine–Ammonia Hydrogen Bonding Complex. *Chemical Physics Letters* **2004**, *397* (1–3), 160–168.

(17) Nishio, M. The C-H/π Hydrogen Bond in Chemistry. Conformation, Supramolecules, Optical Resolution and Interactions Involving Carbohydrates. *Physical Chemistry Chemical Physics* **2011**, *13* (31), 13873–13900.

(18) Ringer, A. L.; Sinnokrot, M. O.; Lively, R. P.; Sherrill, C. D. The Effect of Multiple Substituents on Sandwich and T-Shaped π–π Interactions. *Chemistry - A European Journal* **2006**, *12* (14), 3821–3828.

(19) Tsuzuki, S.; Honda, K.; Uchimaru, T.; Mikami, M.; Tanabe, K. The Magnitude of the C-H/π Interaction between Benzene and Some Model Hydrocarbons. *Journal of the American Chemical Society* **2000**, *122* (15), 3746–3753.

(20) Honda, K.; Mikami, M.; Tsuzuki, S.; Uchimaru, T.; Tanabe, K. Origin of the Attraction and Directionality of the N-H/π Interaction: Comparison with O-H/π and C-H/π Interactions. *Journal of the American Chemical Society* **2002**, *122* (46), 11450–11458.

(21) Gu, Y.; Kar, T.; Scheiner, S.; June, R. V; Re, V.; Recei, M.; August, V. Fundamental Properties of the C-H··O Interaction: Is It a True Hydrogen Bond? *Journal of American Chemical Society* **1999**,121, 9411–9422.

(22) Scheiner, S.; Kar, T. Spectroscopic and Structural Signature of the C-H-O Hydrogen Bond. *Journal of Physical Chemistry A* **2008**, *112* (46), 11854–11860.

(23) Tsuzuki, S.; Uchimaru, T.; Mikami, M. Magnitude of C-H/O Interactions between Carbohydrate and Water. *Theoretical Chemistry Accounts* **2012**, *131* (3), 1–8.

(24) Mahadevi, A. S.; Rahalkar, A. P.; Gadre, S. R.; Sastry, G. N. Ab Initio Investigation of Benzene Clusters: Molecular Tailoring Approach. *Journal of Chemical Physics* **2010**, *133*, 164308.

(25) Hobza, P.; Selzle, H. L.; Schalag, E. W. Structure and Properties of Benzene-Containing Molecular Clusters: Nonempirical Ab Initio Calculations and Experiments. *Chemical Reviews* **1994**, *94*, 1767–1785.

(26) Politzer, P.; Murray, J. S. Halogen Bonding: An Interim Discussion. *ChemPhysChem* **2013**, *14* (2), 278–294.

(27) Bauzá, A.; Alkorta, I.; Frontera, A.; Elguero, J. On the Reliability of Pure and Hybrid DFT Methods for the Evaluation of Halogen, Chalcogen, and Pnicogen Bonds Involving Anionic and Neutral Electron Donors. *Journal of Chemical Theory and Computation* **2013**, *9* (11), 5201–5210.

(28) Aakeröy, C. B.; Fasulo, M.; Schultheiss, N.; Desper, J.; Moore, C. Structural Competition between Hydrogen Bonds and Halogen Bonds. *Journal of the American Chemical Society* **2007**, *129* (45), 13772–13773.

(29) Alkorta, I.; Blanco, F.; Solimannejad, M.; Elguero, J. Competition of Hydrogen Bonds

and Halogen Bonds in Complexes of Hypohalous Acids with Nitrogenated Bases. *Journal of Physical Chemistry A* **2008**, *112* (43), 10856–10863.

(30)   Lu, Y.; Wang, Y.; Zhu, W. Nonbonding Interactions of Organic Halogens in Biological Systems: Implications for Drug Discovery and Biomolecular Design. *Physical Chemistry Chemical Physics* **2010**, *12* (18), 4543–4551.

(31)   Luo, X.; Yang, H.; Lu, Y.; Shi, T.; Jiang, H.; Wang, Y.; Zhu, W.; Yan, X. Halogen Bonding-A Novel Interaction for Rational Drug Design? *Journal of Medicinal Chemistry* **2009**, *52* (9), 2854–2862.

(32)   Andrea, V.; P., H. The Role of Halogen Bonding in Inhibitor Recognition and Binding by Protein Kinases. *Current Topics in Medicinal Chemistry* **2007**, *7* (14), 1336–1348.

(33)   Auffinger, P.; Hays, F. A.; Westhof, E.; Ho, P. S. Halogen Bonds in Biological Molecules. *Proceedings of the National Academy of Sciences* **2004**, *101* (48), 16789–16794.

(34)   Clark, T.; Hennemann, M.; Murray, J. S.; Politzer, P. Halogen Bonding: The σ-Hole. *Journal of Molecular Modeling* **2006**, *13* (2), 291–296.

(35)   Vogel, L.; Wonner, P.; Huber, S. M. Chalcogen Bonding: An Overview. *Angewandte Chemie - International Edition* **2019**, *58* (7), 1880–1891.

(36)   Wang, W.; Ji, B.; Zhang, Y. Chalcogen Bond: A Sister Noncovalent Bond to Halogen Bond. *Journal of Physical Chemistry A* **2009**, *113* (28), 8132–8135.

(37)   Mahmudov, K. T.; Gurbanov, A. V.; Guseinov, F. I.; Guedes da Silva, M. F. C. Noncovalent Interactions in Metal Complex Catalysis. *Coordination Chemistry Reviews* **2019**, *387*, 32–46.

(38)   Chen, L.; Xiang, J.; Zhao, Y.; Yan, Q. Reversible Self-Assembly of Supramolecular Vesicles and Nanofibers Driven by Chalcogen-Bonding Interactions. *Journal of the American Chemical Society* **2018**, *140* (23), 7079–7082.

(39)   Gleiter, R.; Haberhauer, G.; Werz, D. B.; Rominger, F.; Bleiholder, C. From Noncovalent Chalcogen-Chalcogen Interactions to Supramolecular Aggregates: Experiments and Calculations. *Chemical Reviews* **2018**, *118* (4), 2010–2041.

(40)   Beno, B. R.; Yeung, K. S.; Bartberger, M. D.; Pennington, L. D.; Meanwell, N. A. A Survey of the Role of Noncovalent Sulfur Interactions in Drug Design. *Journal of Medicinal Chemistry* **2015**, *58* (11), 4383–4438.

(41)   Fanfrlík, J.; Přáda, A.; Padělková, Z.; Pecina, A.; Macháček, J.; Lepšík, M.; Holub, J.; Růžička, A.; Hnyk, D.; Hobza, P. The Dominant Role of Chalcogen Bonding in the Crystal Packing of 2D/3D Aromatics. *Angewandte Chemie* **2014**, *126* (38), 10303–10306.

(42)   Jin, Y.; Lu, T.; Feng, G. The Preferred Conformation of the Tetrafluoro-1,3-Dithietane···isopropylamine Complex as Revealed by Rotational Spectroscopy. *Physical Chemistry Chemical Physics* **2020**, *22* (48), 28339–28344.

(43)   Goodwin, E. J.; Legon, A. C. The Rotational Spectrum and Molecular Geometry of an Antihydrogen-Bonded Dimer of Sulfur Dioxide and Hydrogen Cyanide. *The Journal of Chemical Physics* **1986**, *85* (12), 6828–6836.

(44)   Legon, A. C. Tetrel, Pnictogen and Chalcogen Bonds Identified in the Gas Phase before They Had Names: A Systematic Look at Non-Covalent Interactions. *Physical Chemistry Chemical Physics* **2017**, *19* (23), 14884–14896.

(45)   Ramasami, P.; Ford, T. A. Chalcogen-Bonded Complexes of Some Carbon Dioxide Analogues. *Journal of Molecular Structure* **2014**, *1072* (1), 28–31.

(46)   Kumpf, R. A.; Dougherty, D. A. A Mechanism for Ion Selectivity in Potassium Channels: Computational Studies of Cation-π Interactions. *Science* **1993**, *261* (5129), 1708–1710.

(47)   Hunter, C. A.; Sanders, J. K. M. The Nature of π-π Interactions. *Journal of the American Chemical Society* **2005**, *112* (14), 5525–5534.

(48)   Pietraperzia, G.; Pasquini, M.; Mazzoni, F.; Piani, G.; Becucci, M.; Biczysko, M.; Michalski, D.; Bloino, J.; Barone, V. Non-covalent Interactions in the Gas Phase: The Anisole-Phenol Complex. *Journal of Physical Chemistry A* **2011**, *115* (34), 9603–9611.

(49)   Williams, D. H.; Stephens, E.; O'Brien, D. P.; Zhou, M. Understanding Noncovalent Interactions: Ligand Binding Energy and Catalytic Efficiency from Ligand-Induced Reductions in Motion within Receptors and Enzymes. *Angewandte Chemie - International Edition*. December 10, 2004.

(50)   Grimme, S. Do Special Noncovalent π-π Stacking Interactions Really Exist? *Angewandte Chemie - International Edition* **2008**, *47* (18), 3430–3434.

(51)   Langreth, D. C.; Cooper, V. R.; Schröder, E.; Puzder, A.; Lundqvist, B. I.; Thonhauser, T. Stacking Interactions and the Twist of DNA. *Journal of the American Chemical Society* **2007**, *130* (4), 1304–1308.

(52)   Knowles, R. R.; Jacobsen, E. N. Attractive Noncovalent Interactions in Asymmetric Catalysis: Links between Enzymes and Small Molecule Catalysts. *Proceedings of the National Academy of Sciences* **2010**, *107* (48), 20678–20685.

(53)   Keinan, S.; Contreras-García, J.; Johnson, E. R.; Yang, W.; Mori-Sánchez, P.; Cohen, A. J. Revealing Noncovalent Interactions. *Journal of the American Chemical Society* **2010**, *132* (18), 6498–6506.

(54)   Kollman, P. A.; Jaffe, R.; Pearlman, D. A.; Chipot, C.; Maigret, B. Benzene Dimer: A Good Model for π−π Interactions in Proteins? A Comparison between the Benzene and the Toluene Dimers in the Gas Phase and in an Aqueous Solution. *Journal of the American Chemical Society* **2002**, *118* (45), 11217–11224.

(55)   Hohenstein, E. G.; Duan, J.; Sherrill, C. D. Origin of the Surprising Enhancement of Electrostatic Energies by Electron-Donating Substituents in Substituted Sandwich Benzene Dimers. *Journal of the American Chemical Society* **2011**, *133* (34), 13244–13247.

(56)   Arunan, E.; Gutowsky, H. S. The Rotational Spectrum, Structure and Dynamics of a Benzene Dimer. *The Journal of Chemical Physics* **1993**, *98* (5), 4294–4296.

(57)   Gutowsky, H. S.; Emilsson, T.; Arunan, E. Low-J Rotational Spectra, Internal Rotation, and Structures of Several Benzene-Water Dimers. *The Journal of Chemical Physics* **1993**, *99* (7), 4883–4893.

(58)   Thonhauser, T.; Puzder, A.; Langreth, D. C. Interaction Energies of Monosubstituted Benzene Dimers via Nonlocal Density Functional Theory. *The Journal of Chemical Physics* **2006**, *124*, 164106.

(59)   Kokkin, D.; Ivanov, M.; Loman, J.; Cai, J. Z.; Uhler, B.; Reilly, N.; Rathore, R.; Reid, S. A. π-π Stacking vs. C-H/π Interaction: Excimer Formation and Charge Resonance Stabilization in van der Waals Clusters of 9,9′-Dimethylfluorene. *Journal of Chemical Physics* **2018**, *149* (13), 134314.

(60)   Kokkin, D.; Ivanov, M. V.; Loman, J.; Cai, J.-Z. Z.; Rathore, R.; Reid, S. A. Strength of π-Stacking, from Neutral to Cation: Precision Measurement of Binding Energies in an Isolated π-Stacked Dimer. *Journal of Physical Chemistry Letters* **2018**, *9* (8), 2058–2061.

(61)   Reilly, N.; Ivanov, M.; Uhler, B.; Talipov, M.; Rathore, R.; Reid, S. A. First Experimental Evidence for the Diverse Requirements of Excimer vs Hole Stabilization in π-Stacked Assemblies. *Journal of Physical Chemistry Letters* **2016**, *7* (15), 3042–3045.

(62)   Ivanov, M. V; Reilly, N.; Uhler, B.; Kokkin, D.; Rathore, R.; Reid, S. A. Cofacially Arrayed Polyfluorenes: Spontaneous Formation of π-Stacked Assemblies in the Gas Phase. *Journal of Physical Chemistry Letters* **2017**, *8* (21), 5272–5276.

(63)   Barnes, A. J. Jet Spectroscopy and Molecular Dynamics. *Journal of Molecular Structure* **1996**, *385* (1), 69.

(64)   Anderson, J. B.; Fenn, J. B. Velocity Distributions in Molecular Beams from Nozzle Sources. *Physics of Fluids* **1965**, *8* (5), 780–787.

(65)   Robertson, W. H.; Kelley, J. A.; Johnson, M. A. A Pulsed Supersonic Entrainment Reactor for the Rational Preparation of Cold Ionic Complexes. *Review of Scientific Instruments* **2000**, *71* (12), 4431–4434.

(66)   Smalley, R. E.; Ramakrishna, B. L.; Levy, D. H.; Wharton, L. Laser Spectroscopy of Supersonic Molecular Beams: Application to the NO$_2$ Spectrum. *The Journal of Chemical Physics* **2004**, *61* (10), 4363–4364.

(67)   Luria, K.; Christen, W.; Even, U. Generation and Propagation of Intense Supersonic Beams. *Journal of Physical Chemistry A* **2011**, *115* (25), 7362–7367.

(68)   Barnes, A. J. Jet Spectroscopy and Molecular Dynamics. *Journal of Molecular Structure* **2003**, *385* (1), 69.

(69)   Smalley, R. E.; Auerbach, D. A.; Fitch, P. S. H.; Levy, D. H.; Wharton, L. Laser Spectroscopic Measurement of Weakly Attractive Interatomic Potentials: The Na+Ar Interaction. *The Journal of Chemical Physics* **1977**, *66* (8), 3778–3785.

(70)   Brutschy, B. Reactions in Molecular Clusters Following Photoionization. *Journal of Physical Chemistry* **1990**, *94*, 8637–8647.

(71)   Giardini-Guidoni, A.; Piccirillo, S.; Palleschi, A.; Toja, D. Resonance Enhanced Multiphoton Ionization Processes to Study Spectroscopy and Reactivity of van der Waals Clusters of Aromatic Molecules. *Proceedings of the Indian Academy of Sciences: Chemical Sciences* **1998**, *110* (3), 153–162.

(72)   Reid, S. A.; Nyambo, S.; Kalume, A.; Uhler, B.; Karshenas, C.; Muzangwa, L. Reactive

Pathways in the Chlorobenzene-Ammonia Dimer Cation Radical: New Insights from Experiment and Theory. *Journal of Physical Chemistry A* **2013**, *117* (47), 12429–12437.

(73)   Nyambo, S.; Uhler, B.; Muzangwa, L.; Ivanov, M.; Welch, B. K.; Dawes, R.; Reid, S. A. Reactive Pathways in the Bromobenzene-Ammonia Dimer Cation Radical: Evidence for a Roaming Halogen Radical. *Journal of Molecular Structure* **2018**, *1172*, 113–118.

(74)   Chandler, D. W.; Houston, P. L. Two-Dimensional Imaging of State-Selected Photodissociation Products Detected by Multiphoton Ionization. *The Journal of Chemical Physics* **1987**, *87* (2), 1445–1447.

(75)   Eppink, A. T. J. B.; Parker, D. H. Velocity Map Imaging of Ions and Electrons Using Electrostatic Lenses: Application in Photoelectron and Photofragment Ion Imaging of Molecular Oxygen. *Review of Scientific Instruments* **1997**, *68* (9), 3477–3484.

(76)   Cavanagh, S. J.; Gibson, S. T.; Gale, M. N.; Dedman, C. J.; Roberts, E. H.; Lewis, B. R. High-Resolution Velocity-Map-Imaging Photoelectron Spectroscopy of the O-Photodetachment Fine-Structure Transitions. *Physical Review A - Atomic, Molecular, and Optical Physics* **2007**, *76* (5), 1–9.

(77)   Mazzoni, F.; Pasquini, M.; Pietraperzia, G.; Becucci, M. Binding Energy Determination in a π-Stacked Aromatic Cluster: The Anisole Dimer. *Physical Chemistry Chemical Physics* **2013**, *15* (27), 11268–11274.

(78)   Sampson, R. K.; Lawrance, W. D. The Dissociation Energy of the Benzene-Argon van Der Waals Complex Determined by Velocity Map Imaging. *Australian Journal of Chemistry* **2003**, *56* (4), 275–277.

(79)   Samanta, A. K.; Wang, Y.; Mancini, J. S.; Bowman, J. M.; Reisler, H. Energetics and Predissociation Dynamics of Small Water, HCl, and Mixed HCl-Water Clusters. *Chemical Reviews* **2016**, *116* (9), 4913–4936.

(80)   Samanta, A. K.; Czakó, G.; Wang, Y.; Mancini, J. S.; Bowman, J. M.; Reisler, H. Experimental and Theoretical Investigations of Energy Transfer and Hydrogen-Bond Breaking in Small Water and HCl Clusters. *Accounts of Chemical Research* **2014**, *47* (8), 2700–2709.

(81)   Chng, L. C.; Samanta, A. K.; Czakó, G.; Bowman, J. M.; Reisler, H. Experimental and Theoretical Investigations of Energy Transfer and Hydrogen-Bond Breaking in the Water Dimer. *Journal of the American Chemical Society* **2012**, *134* (37), 15430–15435.

(82)   Rocher-Casterline, B. E.; Chng, L. C.; Mollner, A. K.; Reisler, H. Communication: Determination of the Bond Dissociation Energy (D_0) of the Water Dimer, $(H_2O)_2$, by Velocity Map Imaging. *Journal of Chemical Physics* **2011**, *134* (21), 211101.

(83)   Yoder, L. M.; Barker, J. R.; Lorenz, K. T.; Chandler, D. W. Ion Imaging the Recoil Energy Distribution Following Vibrational Predissociation of Triplet State Pyrazine-Ar van der Waals Clusters. *Chemical Physics Letters* **1999**, *302* (5–6), 602–608.

(84)   Gascooke, J. R.; Lawrance, W. D. Translational Energy Distributions for Dissociation of the van Der Waals Cation Species $(C_6H_6 \cdots Ar_n)^+$ ($n = 1,2$) Measured by Velocity Map Imaging. *The Journal of Physical Chemistry A* **2002**, *104* (45), 10328–10335.

(85)   Sampson, R. K.; Bellm, S. M.; Gascooke, J. R.; Lawrance, W. D. Velocity- and Mass-Resolved REMPI Spectroscopy of van der Waals Molecules. A Technique for Determining the Cluster Size Responsible for Spectral Features. *Chemical Physics Letters* **2003**, *372* (3–4), 307–313.

(86)   Bellm, S. M.; Gascooke, J. R.; Lawrance, W. D. The Dissociation Energy of van Der Waals Complexes Determined by Velocity Map Imaging: Values for S_0 and S_1 *p*-Difluorobenzene-Ar and D_0 (p-Difluorobenzene-Ar) $^+$. *Chemical Physics Letters* **2000**, *330* (1–2), 103–109.

(87)   Bellm, S. M.; Lawrence, W. D. The Binding Energy of Ar to *p*-Difluorobenzene - Ar. How Large Are Three-Body Effects in *p*-Difluorobenzene-Ar$_2$? *Chemical Physics Letters* **2003**, *368*, 542–546.

(88)   Bellm, S. M.; Lawrance, W. D. The Partitioning of Energy amongst Vibration, Rotation, and Translation during the Dissociation of *p*-Difluorobenzene-Ar Neutral and Cation Complexes. *Journal of Chemical Physics* **2003**, *118* (6), 2581–2589.

(89)   Holmes-Ross, H. L.; Lawrance, W. D. The Binding Energies of NO-Rg (Rg = He, Ne, Ar) Determined by Velocity Map Imaging. *Journal of Chemical Physics* **2011**, *135* (1), 14302.

(90)   Holmes-Ross, H. L.; Lawrance, W. D. The Dissociation of NO-Ar (Ã) from around Threshold to 200 cm $^{-1}$ above Threshold. *Journal of Chemical Physics* **2010**, *133* (1), 14304.

(91)   Wright, D. S.; Holmes-Ross, H. L.; Lawrance, W. D. Dissociation of the NO-CH$_4$ van Der Waals Complex: Binding Energy and Correlated Motion of the Molecular Fragments. *Chemical Physics Letters* **2007**, *435* (1–3), 19–23.

(92)   Mazzoni, F.; Becucci, M.; Řezáč, J.; Nachtigallová, D.; Michels, F.; Hobza, P.; Müller-Dethlefs, K. Structure and Energetics of the Anisole-Ar$_n$ (n = 1, 2, 3) Complexes: High-Resolution Resonant Two-Photon and Threshold Ionization Experiments, and Quantum Chemical Calculations. *Physical Chemistry Chemical Physics* **2015**, *17* (19), 12530–12537.

(93)   CNRS LV_pBASEX. 2.10; Iramis CEA. **2013**.

(94)   Botti, S. Applications of Time-Dependent Density Functional Theory. **2004**, 54–60.

(95)   Zhao, Y.; Truhlar, D. G.; Zhao, Y.; Truhlar, · D G. The M06 Suite of Density Functionals for Main Group Thermochemistry, Thermochemical Kinetics, Noncovalent Interactions, Excited States, and Transition Elements: Two New Functionals and Systematic Testing of Four M06-Class Functionals and 12 Other Function. *Theor Chem Account* **2008**, *120*, 215–241.

(96)   Boys, S. F.; Bernardi, F. Molecular Physics An International Journal at the Interface Between Chemistry and Physics The Calculation of Small Molecular Interactions by the Differences of Separate Total Energies. Some Procedures with Reduced Errors The Calculation of Small Molecular. *Molecular Physics* **1970**, *19* (4), 553–566.

(97)   Sherrill, C. D. Distinguishing Basis Set Superposition Error (BSSE) from Basis Set Incompleteness Error (BSIE). **2017**, 1–4.

(98)   Biczysko, M.; Piani, G.; Pasquini, M.; Schiccheri, N.; Pietraperzia, G.; Becucci, M.; Pavone, M.; Barone, V. On the Properties of Microsolvated Molecules in the Ground (S_0) and Excited (S_1) States: The Anisole-Ammonia 1:1 Complex. *Journal of Chemical Physics* **2007**, *127* (14), 0–11.

(99)   Eisenhardt, C. G.; Pasquini, M.; Pietraperzia, G.; Becucci, M. A Study on the Anisole-Carbon Dioxide van der Waals Complex by High Resolution Electronic Spectroscopy. *Physical Chemistry Chemical Physics* **2002**, *4* (22), 5590–5593.

(100)   Lin, T.; Zhang, W.; Wang, L. Complex Formation between Anisole and Boron Trifluoride: Structural and Binding Properties. *Journal of Physical Chemistry A* **2008**, *112* (51), 13600–13608.

(101)   Becucci, M.; Pietraperzia, G.; Pasquini, M.; Piani, G.; Zoppi, A.; Chelli, R.; Castellucci, E.; Demtroeder, W. A Study on the Anisole-Water Complex by Molecular Beam-Electronic Spectroscopy and Molecular Mechanics Calculations. *Journal of Chemical Physics* **2004**, *120* (12), 5601–5607.

(102)   Piani, G.; Pasquini, M.; Pietraperzia, G.; Becucci, M.; Armentano, A.; Castellucci, E. The Anisole-Ammonia Complex: Marks of the Intermolecular Interactions. *Chemical Physics Letters* **2007**, *434* (1–3), 25–30.

(103)   Řezáč, J.; Nachtigallová, D.; Mazzoni, F.; Pasquini, M.; Pietraperzia, G.; Becucci, M.; Müller-Dethlefs, K.; Hobza, P. Binding Energies of the π-Stacked Anisole Dimer: New Molecular Beam - Laser Spectroscopy Experiments and Ccsd(t) Calculations. *Chemistry - A European Journal* **2015**, *21* (18), 6740–6746.

(104)   Pasquini, M.; Pietraperzia, G.; Piani, G.; Becucci, M. Excitonic Coupling in van Der Waals Complexes: The Anisole Dimers. *Journal of Molecular Structure* **2011**, *993* (1–3), 491–494.

(105)   Balfour, W. J. The Vibrational Spectrum of Anisole. *Spectrochimica Acta Part A: Molecular Spectroscopy* **1983**, *39* (9), 795–800.

(106)   Faust, S.; Dreier, T.; Schulz, C. Photo-Physical Properties of Anisole: Temperature, Pressure, and Bath Gas Composition Dependence of Fluorescence Spectra and Lifetimes. *Applied Physics B: Lasers and Optics* **2013**, *112* (2), 203–213.

(107)   Hoffmann, L. J. H.; Marquardt, S.; Gemechu, A. S.; Baumgärtel, H. The Absorption Spectra of anisole-h8, anisole-d3 and anisole-d8. The Assignment of Fundamental Vibrations in the S_0 and the S_1 states. *Physical Chemistry Chemical Physics* **2006**, *8* (20), 2360–2377.

(108)   Pradhan, M.; Li, C.; Lin, J. L.; Tzeng, W. B. Mass Analyzed Threshold Ionization Spectroscopy of anisole cation and the OCH_3 substitution effect. *Chemical Physics Letters* **2005**, *407* (1–3), 100–104.

(109)   Eisenhardt, C. G.; Gemechu, A. S.; Baumgärtel, H.; Chelli, R.; Cardini, G.; Cardini, G.; Califano, S.; Califano, S. Excited State Photoelectron Spectroscopy of anisole. *Physical Chemistry Chemical Physics* **2001**, *3* (24), 5358–5368.

(110)   Eisenhardt, C. G.; Pietraperzia, G.; Becucci, M. The High Resolution Spectrum of the $S_1 \leftarrow S_0$ Transition of anisole. *Physical Chemistry Chemical Physics* **2001**, *3* (8), 1407–

1410.

(111) Zwier, T. S. The Spectroscopy of Solvation in Hydrogen-Bonded Aromatic Clusters. *Annual Review of Physical Chemistry* **1996**, *47* (1), 205–241.

(112) Reimann, B.; Buchhold, K.; Barth, H. D.; Brutschy, B.; Tarakeshwar, P.; Kim, K. S. Anisole-(H_2O)n (n=1-3) Complexes: An Experimental and Theoretical Investigation of the Modulation of Optimal Structures, Binding Energies, and Vibrational Spectra in Both the Ground and First Excited States. *Journal of Chemical Physics* **2002**, *117* (19), 8805–8822.

(113) Pasquini, M.; Schiccheri, N.; Piani, G.; Pietraperzia, G.; Becucci, M.; Biczysko, M.; Pavone, M.; Barone, V. Isotopomeric Conformational Changes in the Anisole-Water Complex: New Insights from HR-UV Spectroscopy and Theoretical Studies. *Journal of Physical Chemistry A* **2007**, *111* (49), 12363–12371.

(114) Giuliano, B. M.; Maris, A.; Melandri, S.; Caminati, W. Pure Rotational Spectrum and Model Calculations of Anisole-Ammonia. *Journal of Physical Chemistry A* **2009**, *113* (52), 14277–14280.

(115) Takayanagi, M.; Hanazaki, I. SEP-LIF Study on Dynamics of Vibrationally Excited States of van der Waals Complexes: The Anisole·Ar Complex. *Chemical Physics Letters* **1992**, *190* (1–2), 115–118.

(116) Pietraperzia, G.; Pasquini, M.; Schiccheri, N.; Piani, G.; Becucci, M.; Castellucci, E.; Biczysko, M.; Bloino, J.; Barone, V. The Gas Phase Anisole Dimer: A Combined High-Resolution Spectroscopy and Computational Study of a Stacked Molecular System. *Journal of Physical Chemistry A* **2009**, *113* (52), 14343–14351.

(117) Heger, M.; Altnö, J.; Poblotzki, A.; Suhm, M. A. To p or Not to p – How Does Methanol Dock onto Anisole? *Physical Chemistry Chemical Physics* **2015**, *17*, 13045.

(118) Becucci, M.; Mazzoni, F.; Pietraperzia, G.; Řezáč, J.; Natchigallová, D.; Hobza, P. Non-Covalent Interactions in Anisole-(CO_2)n (n = 1, 2) Complexes. *Physical Chemistry Chemical Physics* **2017**, *19* (34), 22749–22758.

(119) Thurn, H. V.; Grotemeyer, J. Resonant Two-Photon Ionization Studies of Toluene with Anisole Cluster: A System with Competing Non-Covalent Interactions. *ChemistrySelect* **2016**, *1* (11), 2664–2667.

(120) Tsuzuki, S.; Honda, K.; Fujii, A.; Uchimaru, T. C-H/π Interactions in Methane Clusters with Polycyclic Aromatic Hydrocarbons. *Physical Chemistry Chemical Physics* **2008**, *10*, 2860–2865.

(121) Schauer, M.; Law, K.; Bernstein, E. R. Supersonic Molecular Jet Studies of Toluene-Helium and Toluene-Methane Clusters. *The Journal of Chemical Physics* **1984**, *81* (1), 49–56.

(122) Ringer, A. L.; Figgs, M. S.; Sinnokrot, M. O.; Sherrill, C. D. Aliphatic C-H/π Interactions: Methane-Benzene, Methane-Phenol, and Methane-Indole Complexes. *Journal of Physical Chemistry A* **2006**, *110* (37), 10822–10828.

(123) Schauer, M.; Law, K. S.; Bernstein, E. R. Molecular Jet Study of the Solvation of Toluene by Methane, Ethane, and Propane. *The Journal of Chemical Physics* **1985**, *82* (2), 736–

746.

(124) Gemechu, A. S.; Hoffmann, L. J. H.; Marquardt, S.; Eisenhardt, C. G.; Baumgärtel, H.; Chelli, R.; Cardini, G.; Califano, S. The Absorption Spectrum of Anisole and the Anisole/$CO_2$1:1-Cluster. The Influence of Intermolecular Interaction on Intramolecular Vibrations. *Zeitschrift fur Physikalische Chemie* **2004**, *218* (1), 123–153.

(125) Frisch, M. J.; Trucks, G. W.; Schlegel, H. B.; Scuseria, G. E.; Robb, M. A.; Cheeseman, J. R.; Scalmani, G.; Barone, V.; Mennucci, B.; Petersson, G. A.; et al. Gaussian 09, Revision D.01. *Gaussian Inc.* **2013**, 1–20.

(126) Adamo, C.; V., B.; Scuseria, G. E. Accurate Excitation Energies from Time-Dependent Density Functional Theory. The Assessment of the PBE0 Model. *Journal of ChemicalPhysics***1999**, *111* (November), 2889.

(127) Sinnokrot, M. O.; Sherrill, D. Highly Accurate Coupled Cluster Potential Energy Curves for the Benzene Dimer: Sandwich, T-Shaped, and Parallel-Displaced Configurations. **2004**.

(128) Grimme, S.; Antony, J.; Ehrlich, S.; Krieg, H. A Consistent and Accurate Ab Initio Parametrization of Density Functional Dispersion Correction (DFT-D) for the 94 Elements H-Pu. *Journal of Chemical Physics* **2010**, *132* (15), 5029.

(129) Weigend, F. Accurate Coulomb-Fitting Basis Sets for H to Rn. *Physical Chemistry Chemical Physics* **2006**, *8* (9), 1057–1065.

(130) Frey, J. A.; Holzer, C.; Klopper, W.; Leutwyler, S. Experimental and Theoretical Determination of Dissociation Energies of Dispersion-Dominated Aromatic Molecular Complexes. *Chemical Reviews* **2016**, *116* (9), 5614–5641.

(131) Shibasaki, K.; Fujii, A.; Mikami, N.; Tsuzuki, S. Magnitude of the C-H/π Interaction in the Gas Phase: Experimental and Theoretical Determination of the Accurate Interaction Energy in Benzene-Methane. *Journal of Physical Chemistry A* **2006**, *110* (13), 4397–4404.

(132) Ruckenstein, E.; Shulgin, I. L.; Tilson, J. L. The Structure of Dilute Clusters of Methane and Water by Ab Initio Quantum Mechanical Calculations. *Journal of Physical Chemistry A* **2003**, *107* (13), 2289–2295.

(133) Kollman, P. A. Noncovalent Interactions. *Accounts of Chemical Research* **1977**, *10* (10), 365–371.

(134) Kim, K. S.; Tarakeshwar, P.; Lee, J. Y. Molecular Clusters of π-Systems: Theoretical Studies of Structures, Spectra, and Origin of Interaction Energies. *Chemical Reviews* **2000**, *100* (11), 4145–4185.

(135) Gadre, S. R.; Yeole, S. D.; Sahu, N. Quantum Chemical Investigations on Molecular Clusters. *Chemical Reviews* **2014**, *114* (24), 12132–12173.

(136) Buck, U. Structure, Energetics, Dynamics. Structure and Dynamics of Size Selected Molecular Clusters. *Berichte der Bunsengesellschaft für physikalische Chemie* **1992**, *96* (9), 1275–1284.

(137) Castellano, R. K. Special Issue: Intramolecular Hydrogen Bonding. *Molecules* **2014**, *19*

(10), 15783–15785.

(138) Clark, T.; Hennemann, M.; Murray, J. S.; Politzer, P. Halogen Bonding : The σ-Hole Halogen Bonding : The σ-Hole. *Journal of Molecular Modeling* **2007**, *13*, 291–296.

(139) Politzer, P.; Murray, J. S.; Clark, T.; Resnati, G. The σ-Hole Revisited. *Physical Chemistry Chemical Physics* **2017**, *19* (48), 32166–32178.

(140) Re, S.; Nagase, S. How Is the C-H/π Interaction Important for Molecular Recognition? *Chemical Communications* **2004**, *4* (6), 658–659.

(141) Nishio, M. C-H/π Hydrogen Bonds in Crystals. *CrystEngComm* **2004**, *6*, 130–158.

(142) Nishio, M.; Umezawa, Y.; Honda, K.; Tsuboyama, S.; Suezawa, H. C-H/π Hydrogen Bonds in Organic and Organometallic Chemistry. *CrystEngComm* **2009**, *11* (9), 1757–1788.

(143) Shibasaki, K.; Fujii, A.; Mikami, N.; Tsuzuki, S. Magnitude and Nature of Interactions in Benzene-X (X = Ethylene and Acetylene) in the Gas Phase: Significantly Different C-H/π Interaction of Acetylene as Compared with Those of Ethylene and Methane. *Journal of Physical Chemistry A* **2007**, *111* (5), 753–758.

(144) Fujii, A.; Shibasaki, K.; Kazama, T.; Itaya, R.; Mikami, N.; Tsuzuki, S. Experimental and Theoretical Determination of the Accurate Interaction Energies in Benzene-Halomethane: The Unique Nature of the Activated C-H/π Interaction of Haloalkanes. *Physical Chemistry Chemical Physics* **2008**, *10* (19), 2836–2843.

(145) Tsuzuki, S.; Honda, K.; Fujii, A.; Uchimaru, T.; Mikami, N. C-H/π Interactions in Methane Clusters with Polycyclic Aromatic Hydrocarbons. *Physical Chemistry Chemical Physics* **2008**, *10* (19), 2860–2865.

(146) Fujii, A.; Hayashi, H.; Park, J. W.; Kazama, T.; Mikami, N.; Tsuzuki, S. Experimental and Theoretical Determination of the Accurate C-H/π Interaction Energies in Benzene-Alkane Clusters: Correlation between Interaction Energy and Polarizability. *Physical Chemistry Chemical Physics* **2011**, *13* (31), 14131–14141.

(147) Greer, J. C.; Ahlrichs, R.; Hertel, I. V. Binding Energies and Structures of N-H$_3$ Clusters. *Chemical Physics* **1989**, *133* (2), 191–197.

(148) Feyereisen, M. W.; Feller, D.; Dixon, D. A. Hydrogen Bond Energy of the Water Dimer. *Journal of Physical Chemistry* **1996**, *100* (8), 2993–2997.

(149) Alberto, M. E.; Mazzone, G.; Russo, N.; Sicilia, E. The Mutual Influence of Non-Covalent Interactions in π-Electron Deficient Cavities: The Case of Anion Recognition by Tetraoxacalix[2]Arene[2] Triazine. *Chemical Communications* **2010**, *46* (32), 5894–5896.

(150) Grabowski, S. J. Cooperativity of Hydrogen and Halogen Bond Interactions. *Theoretical Chemistry Accounts* **2013**, *132* (4), 1–10.

(151) Zhao, H.; Tang, S.; Zhang, Q.; Du, L. Weak Hydrogen Bonding Competition between O-H···π and O-H···Cl. *RSC Advances* **2017**, *7* (36), 22485–22491.

(152) Esrafili, M. D.; Mousavian, P. The Strengthening Effect of a Halogen, Chalcogen or Pnicogen Bonding on Halogen–π Interaction: A Comparative Ab Initio Study. *Molecular*

Physics **2018**, *116* (4), 526–535.

(153) Hobza, P.; Bludský, O.; Selzle, H. L.; Schlag, E. W. Ab Initio Calculations on the Structure, Vibrational Frequencies, and Valence Excitation Energies of the Benzene⋯Ar and Benzene⋯Ar$_2$ Cluster. *Chemical Physics Letters* **1996**, *250* (3–4), 402–408.

(154) Schmidt, M.; Mons, M.; Le Calvé, J. Intermolecular Vibronic Spectroscopy of Small Van Der Waals Clusters: Phenol- and Aniline-(Argon)2 Complexes. *Zeitschrift für Physik D Atoms, Molecules and Clusters* **1990**, *17* (2), 153–155.

(155) Takahashi, M.; Ozeki, H.; Kimura, K. Vibrational Spectra of Aniline-Arn van Der Waals Cations (n = 1 and 2) Observed by Two-Color "Threshold Photoelectron" [Zero Kinetic Energy (ZEKE)-Photoelectron] Spectroscopy. *The Journal of Chemical Physics* **1992**, *96* (9), 6399–6406.

(156) Schauer, M.; Bernstein, E. R. Molecular Jet Study of the Solvation of Benzene by Methane, Ethane, and Propane. *The Journal of Chemical Physics* **1985**, *82* (2), 726–735.

(157) Bernstein, E. R.; Law, K.; Schauer, M. Molecular Supersonic Jet Studies of Aniline Solvation by Helium and Methane. *The Journal of Chemical Physics* **1984**, *80* (2), 634–644.

(158) Eisenhardt, C. G.; Oppel, M.; Baumgärtel, H. Excited State Photoelectron Spectroscopy on Molecular Aggregates Containing Aromatic Molecules. *Journal of Electron Spectroscopy and Related Phenomena* **2000**, *108* (1), 141–151.

(159) Bellm, S. M.; Moulds, R. J.; Lawrence, W. D. The Binding Energies of P-Difluorobenzene-Ar,-Kr Measured by Velocity Map Imaging: Limitations of Dispersed Fluorescence in Determining Binding Energies. *Journal of Chemical Physics* **2001**, *115* (23), 10709–10717.

(160) Moll, D. .; Parker Jr, G. R.; Kuppermann, A. Time-Resolved Two-Color Photoacoustic and Multiphoton Spectroscopy of Aniline. *Journal of Chemical Physics* **1984**, *80* (10), 4808–4848.

(161) Smith, M. A.; Hager, J. W.; Wallace, S. C. Two Color Photoionization Spectroscopy of Jet Cooled Aniline: Vibrational Frequencies of the Aniline X̃2B1 Radical Cation. *The Journal of Chemical Physics* **1984**, *80* (7), 3097–3105.

(162) Lemaire, J.; Dimicoli, I.; Piuzzi, F.; Botter, R. Two-Color Photoionization Spectroscopy of Polyatomic Molecules and Cations: Aniline, Phenol and Phenotole. *Chemical Physics* **1987**, *115* (1), 119–128.

(163) Syage, J. A.; Wessel, J. E. Ion Dip Spectroscopy of Higher Excited Vibronic States of Aniline. *The Journal of Chemical Physics* **1986**, *85* (11), 6806–6807.

(164) Yamanouchi, K.; Isogai, S.; Tsuchiya, S. Laser-Induced Fluorescence Spectroscopy of He-, Ne-, Ar-, and Kr-Aniline van der Waals Complexes in a Supersonic Free Jet. Analysis of Rotational Contours. *Chemical Physics* **1987**, *116* (1), 123–132.

(165) Becucci, M.; Pietraperzia, G.; Castellucci, E.; Bréchignac, P. Dynamics of Vibronically Excited States of the Aniline-Neon van der Waals Complex: Vibrational Predissociation versus Intramolecular Vibrational Redistribution. *Chemical Physics Letters* **2004**, *390* (1–

3), 29–34.

(166) Makarewicz, J. Structure and Dynamics of the Aniline-Argon Complex as Derived from Its Potential Energy Surface. *Journal of Physical Chemistry A* **2007**, *111* (8), 1498–1507.

(167) Pino, T.; Parneix, P.; Douin, S.; Bréchignac, P. Solvation Dynamics of Large van Der Waals Aniline-Ar_n Clusters: Experiment and Theory. *Journal of Physical Chemistry A* **2004**, *108* (36), 7364–7371.

(168) Douin, S.; Parneix, P.; Brechignac, P. Solvent Shift of the Ionization Potential of the Aniline-Argon System. *Zeitschrift für Physik D Atoms, Molecules and Clusters* **1991**, *21* (4), 343–348.

(169) Piest, H.; Von Helden, G.; Meijer, G. Infrared Spectroscopy of Jet-Cooled Neutral and Ionized Aniline-Ar. *Journal of Chemical Physics* **1999**, *110* (4), 2010–2015.

(170) Satink, R. G.; Bakker, J. M.; Meijer, G.; Von Helden, G. Vibrational Lifetimes of Aniline-Noble Gas Complexes. *Chemical Physics Letters* **2002**, *359* (1–2), 163–168.

(171) Bieske, E. J.; Rainbird, M. W.; Knight, A. E. W. The van der Waals Vibrations of Aniline-$(Argon)_2$ in the S_1 Electronic State. *The Journal of Chemical Physics* **1991**, *94* (11), 7019–7028.

(172) Bieske, E. J.; Uichanco, A. S.; Rainbird, M. W.; Knight, A. E. W. Mass Selected Resonance Enhanced Multiphoton Ionization Spectroscopy of Aniline-Arn (n=3,4,5,...) van der Waals Complexes. *The Journal of Chemical Physics* **1991**, *94* (11), 7029–7037.

(173) Coutant, B.; Brechignac, P. Anomalous Complex Shift of Low-Frequency out-of-Plane Vibrations in Aniline-M van der Waals Complexes (M=He, Ne, Ar). *The Journal of Chemical Physics* **1994**, *100* (10), 7087–7092.

(174) Douin, S.; Hermine, P.; Parneix, P.; Brechignac, P. Site Specificity of Solvent Shifts as Revealed by Ionization Threshold in Aniline-$(Argon)_n$ Clusters. *The Journal of Chemical Physics* **1992**, *97* (3), 2160–2162.

(175) Parneix, P.; Bréchignac, P. The Hindering of the Inversion Motion in the van der Waals Aniline-Ar_n Clusters: An Adiabatic Molecular Dynamics Simulation for n=1-3. *Journal of Chemical Physics* **1998**, *108* (5), 1932–1939.

(176) Parneix, P.; Bréchignac, P.; Amar, F. G. Isomer Specific Evaporation Rates: The Case of Aniline-Ar_2. *Journal of Chemical Physics* **1996**, *104* (3), 983–991.

(177) Parneix, P.; Halberstadt, N.; Bréchignac, P.; Amar, F. G.; Van Der Avoird, A.; Van Bladel, J. W. I. Quantum Calculation of Vibrational States in the Aniline-Argon van der Waals Cluster. *Journal of Chemical Physics* **1993**, *98* (4), 2709–2719.

(178) Nakanaga, T.; Sugawara, K.; Kawamata, K.; Ito, F. Infrared Depletion Spectroscopy of Aniline-NH_3 and Aniline-NH^+_3 Clusters in a Supersonic Jet. *Chemical Physics Letters* **1997**, *267* (5–6), 491–495.

(179) Fernandez, J. A.; Bernstein, E. R. Structure, Binding Energy, and Intermolecular Modes for the Aniline/Ammonia van der Waals Clusters. *Journal of Chemical Physics* **1997**, *106* (8), 3029–3037.

(180) Nimlos, M. R.; Young, M. A.; Bernstein, E. R.; Kelley, D. F. Vibrational Dynamics of Aniline(Ar)1 and Aniline(CH₄)1 Clusters. *The Journal of Chemical Physics* **1989**, *91* (9), 5268–5277.

(181) Zhang, X.; Smith, J. M.; Knee, J. L. High Resolution Threshold Photoelectron Spectroscopy of Aniline and Aniline van der Waals Complexes. *The Journal of Chemical Physics* **1992**, *97* (5), 2843–2860.

(182) Smith, J. M.; Zhang, X.; Knee, J. L. Aniline-CH4 S1 Vibrational Dynamics Studied with Picosecond Photoelectron Spectroscopy. *The Journal of Chemical Physics* **1993**, *99* (4), 2550–2559.

(183) Foltin, M.; Stueber, G. J.; Bernstein, E. R. Dynamics of Neutral Cluster Growth and Cluster Ion Fragmentation for Toluene/Water, Aniline/Argon, and 4-Fluorostyrene/Argon Clusters: Covariance Mapping of the Mass Spectral Data. *Journal of Chemical Physics* **1998**, *109* (11), 4342–4360.

(184) León, I.; Arnáiz, P. F.; Usabiaga, I.; Fernández, J. A. Mass Resolved IR Spectroscopy of Aniline-Water Aggregates. *Physical Chemistry Chemical Physics* **2016**, *18* (39), 27336–27341.

(185) Alshahateet, S. F.; Bishop, R.; Craig, D. C.; Scudder, M. L. Dimeric C–H···N Interactions and the Crystal Engineering of New Inclusion Host Molecules. *CrystEngComm* **2001**, *3* (48), 225–229.

(186) Chowdhury, P. K.; Sugawara, K.; Nakanaga, T.; Takeo, H. Structure of the Aniline-Benzene and Aniline-Cyclohexane Clusters Based on Infrared Depletion Spectroscopy. *Chemical Physics Letters* **1998**, *285* (1–2), 77–82.

(187) Ohashi, K.; Inokuchi, Y.; Izutsu, H.; Hino, K.; Yamamoto, N.; Nishi, N.; Sekiya, H. Electronic and Vibrational Spectra of Aniline-Benzene Hetero-Dimer and Aniline Homo-Dimer Ions. *Chemical Physics Letters* **2000**, *323* (1–2), 43–48.

(188) Ohashi, K.; Inokuchi, Y.; Nishi, N.; Sekiya, H. Intermolecular Interactions in Aniline-Benzene Hetero-Trimer and Aniline Homo-Trimer Ions. *Chemical Physics Letters* **2002**, *357* (3–4), 223–229.

(189) Chowdhury, P. K. Infrared Depletion Spectroscopy of the Hydrogen-Bonded Aniline-Diethylamine (C₆H₅-NH₂···NHC₄H₁₀) Complex Produced in Supersonic Jet. *Journal of Physical Chemistry A* **2003**, *107* (30), 5692–5696.

(190) Kawamata, K.; Chowdhury, P. K.; Ito, F.; Sugawara, K. I.; Nakanaga, T. Investigation of the N-H Stretching Vibrations of the Aniline - Pyrrole Binary Complex and Its Cation by Infrared Depletion Spectroscopy. *Journal of Physical Chemistry A* **1998**, *102* (25), 4788–4793.

(191) Nakanaga, T.; Ito, F. Investigations on the Hydrogen Bond Interaction in the Aniline-Furan Complex and Its Cation by Infrared Depletion Spectroscopy. *Journal of Physical Chemistry A* **1999**, *103* (28), 5440–5445.

(192) Makuvaza, J. T.; Kokkin, D. L.; Loman, J. L.; Reid, S. A. C-H/π and C-H-O Interactions in Concert: A Study of the Anisole-Methane Complex Using Resonant Ionization and Velocity Mapped Ion Imaging. *The Journal of Physical Chemistry A* **2019**, *16*, 53.

(193)   Bernstein, E. R.; Law, K.; Schauer, M. Molecular Jet Study of Aniline-Helium van Der Waals Molecules and Aniline Radiationless Relaxation in the $^1B_2$ Excited Electronic State. *The Journal of Chemical Physics* **1984**, *80* (1), 207–220.

(194)   Li, J.; Zhang, R. Q. Strong Orbital Deformation Due to C-H-π Interaction in the Benzene-Methane Complex. *Physical Chemistry Chemical Physics* **2015**, *17* (44), 29489–29491.

(195)   Karthikeyan, S.; Ramanathan, V.; Mishra, B. K. Influence of the Substituents on the C-H···π Interaction: Benzene-Methane Complex. *Journal of Physical Chemistry A* **2013**, *117* (30), 6687–6694.

(196)   Menapace, J. A.; Bernstein, E. R. Van der Waals Modes of Solute/Solvent Clusters: Benzene-Methane, -Deuteriomethane, and -Carbon Tetrafluoride. *Journal of Physical Chemistry* **1987**, *91* (11), 2843–2848.

(197)   Hatton, W. E.; Sinke, G. C.; Stull, D. R.; Hildenbrand, D. L. Chemical Thermodynamic Properties of Aniline. *Journal of Chemical and Engineering Data* **1962**, *7* (2), 229–231.

(198)   Von Weyssenhoff, H.; Kraus, F. Vibronic Structure in the Fluorescence Lifetimes and Quantum Yields of Aniline Vapor. *The Journal of Chemical Physics* **1971**, *54* (6), 2387–2392.

(199)   Kraus, F.; Gregorek, E.; von Weysswnhoff, H. Absolute Fluorescence Lifetimes and Quantum Yields of Substituted Anilines in the Gas Phase. *Z Phes Chem Nue Fol* **1972**, *82* (1–4), 139–146.

(200)   Krieg, H.; Grimme, S. Thermochemical Benchmarking of Hydrocarbon Bond Separation Reaction Energies: Jacob's Ladder Is Not Reversed! *Molecular Physics* **2010**, *108* (19–20), 2655–2666.

(201)   Song, X.; Yang, M.; Davidson, E. R.; Reilly, J. P. Zero Kinetic Energy Photoelectron Spectra of Jet-Cooled Aniline. *The Journal of Chemical Physics* **1993**, *99* (5), 3224–3233.

(202)   Politzer, P.; Murray, S.; Clark, T. Halogen Bonding : An Electrostatically-Driven Highly Directional Noncovalent Interaction. **2010**, 7748–7757.

(203)   Politzer, P.; Lane, P.; Concha, M. C.; Ma, Y.; Murray, J. S. An Overview of Halogen Bonding. *Journal of Molecular Modeling* **2007**, *13* (2), 305–311.

(204)   Squire, D. W.; Bernstein, R. B. Multiphoton Ionization Mass Spectrometric Study of Toluene Clusters in a Pulsed Nozzle Beam Time-of-Flight Apparatus. *Journal of Physical Chemistry* **1984**, *88*, 4944–4952.

(205)   Leist, R.; Frey, J. A.; Leutwyler, S. Fluorobenzene-Nucleobase Interactions: Hydrogen Bonding or π-Stacking? *Journal of Physical Chemistry A* **2006**, *110* (12), 4180–4187.

(206)   Sage, A. G.; Oliver, T. A. A.; King, G. A.; Murdock, D.; Harvey, J. N.; Ashfold, M. N. R. UV Photolysis of 4-Iodo-, 4-Bromo-, and 4-Chlorophenol: Competition between C-Y (Y Halogen) and O-H Bond Fission. *Journal of Chemical Physics* **2013**, *138* (16), 164318.

(207)   Brutschy, B.; Dimopoulou-Rademann, U.; Rademann, K.; Baumgärtel, H.; Bisling, P. A Chemical Reaction and Charge Transfer in Heteroclusters of Fluorobenzene. *Berichte der Bunsengesellschaft für physikalische Chemie* **2012**, *88* (3), 215–217.

(208) Dietz, T. G.; Duncan, M. A.; Liverman, M. G.; Smalley, R. E. Resonance Enhanced Two-Photon Ionization Studies in a Supersonic Molecular Beam: Bromobenzene and Iodobenzene. *Journal of Chemical Physics* **1980**, *73* (10), 4816–4821.

(209) Liu, Y. J.; Persson, R.; Karlsson, H. O.; Lunell, S.; Kadi, M.; Karlsson, D.; Davidsson, J. Photodissociation of Bromobenzene, Dibromobenzene, and 1,3,5- Tribromobenzene. *Journal of Chemical Physics* **2004**, *120* (14), 6502–6509.

(210) Vaupel, S.; Brutschy, B.; Tarakeshwar, P.; Kim, K. S. Characterization of Weak N-H-π Intermolecular Interactions of Ammonia with Various Substituted π-Systems. *Journal of the American Chemical Society* **2006**, *128* (16), 5416–5426.

(211) Ford, M. S.; Haines, S. R.; Pugliesi, I.; Dessent, C. E. .; Müller-Dethlefs, K. Rotational Band Contour Analysis in REMPI and ZEKE Spectroscopy: Elucidating the Structures of Phenol-X (X = N_2, CO and Ar) Complexes. *Journal of Electron Spectroscopy and Related Phenomena* **2000**, *112* (1–3), 231–239.

(212) Roeterdink, W. G.; Janssen, M. H. M. Femtosecond Velocity Map Imaging of Dissociative Ionization Dynamics in CF_3I,*Physical Chemistry Chemical Physics* **2002**, *4* (4), 601–612.

(213) Fillery-Travis, A. J.; Legon, A. C. The Geometries of the Heterodimers SO_2···HF and SO_2···HCl as Determined by Rotational Spectroscopy. *Chemical Physics Letters* **1986**, *123* (1–2), 4–8.

(214) Cotti, G.; Holloway, J. H.; Legon, A. C. Molecular Geometry of SO_2 ··· ClF from Its Rotational Spectrum: A Cis, Planar Complex with a Linear O ··· Cl-F Bond. *Chemical Physics Letters* **1996**, *255* (4–6), 401–409.

(215) Connelly, J. P.; Meuwly, M.; Auty, A. R.; Howard, B. J. The Dynamics of N_2-O_3 and N_2-SO_2 Probed by Microwave Spectroscopy. *Journal of Molecular Spectroscopy* **2000**, *199* (2), 205–216.

(216) Lovas, F. J.; Sprague, M. K. Microwave Rotational Spectral Study of SO_2-CO. *Journal of Molecular Spectroscopy* **2015**, *316*, 49–53.

(217) Matsumura, K.; Lovas, F. J.; Suenram, R. D. The Microwave Spectrum and Structure of the H_2O-SO_2 Complex. *The Journal of Chemical Physics* **1989**, *91* (10), 5887–5894.

(218) Uzun, D. R.; Razkazova-Velkova, E.; Beschkov, V.; Petrov, K. A Method for the Simultaneous Cleansing of H_2S and SO_2. *Journal of Chemical Physics* **1987**, *87* (3749).

(219) Oh, J. J.; Hillig, K. W.; Kuczkowski, R. L. Structure of the Dimethyl Ether-Sulfur Dioxide Complex. *Inorganic Chemistry* **1991**, *30* (24), 4583–4588.

(220) Oh, J. J.; LaBarge, M. S.; Matos, J.; Kampf, J. W.; Hillig, K. W.; Kuczkowski, R. L. Structure of the Trimethylamine-Sulfur Dioxide Complex. *Journal of the American Chemical Society* **1991**, *113* (13), 4732–4738.

(221) Obenchain, D. A.; Spada, L.; Alessandrini, S.; Rampino, S.; Herbers, S.; Tasinato, N.; Mendolicchio, M.; Kraus, P.; Gauss, J.; Puzzarini, C.; et al. Unveiling the Sulfur–Sulfur Bridge: Accurate Structural and Energetic Characterization of a Homochalcogen Intermolecular Bond. *Angewandte Chemie - International Edition* **2018**, *57* (48), 15822–

15826.

(222) Andrews, A. M.; Taleb-Bendiab, A.; Labarge, M. S.; Hillig, K. W.; Kuczkowski, R. L. Microwave Spectrum, Structure, Barrier to Internal Rotation, Dipole Moment, and Deuterium Quadupole Coupling Constants of the Ethylene-Sulfur Dioxide Complex. *The Journal of Chemical Physics* **1990**, *93* (10), 7030–7040.

(223) Andrews, A. M.; Hillig, K. W.; Kuczkowski, R. L.; Legon, A. C.; Howard, N. W. Microwave Spectrum, Structure, Dipole Moment, and Deuterium Nuclear Quadrupole Coupling Constants of the Acetylene-Sulfur Dioxide van der Waals Complex. *The Journal of Chemical Physics* **1991**, *94* (11), 6947–6955.

(224) Andrews, A. M.; Hillig, K. W.; Kuczkowski, R. L. Microwave Spectrum, Dipole Moment, Structure, and Internal Rotation of the Cyclopropane-Sulfur Dioxide van der Waals Complex. *Journal of Chemical Physics* **1992**, *96* (3), 1784–1792.

(225) Sun, L. The Microwave Spectrum and Structure of the Carbon Dioxide-Sulphur Dioxide Complex. *Molecular Physics* **1996**, *88* (1), 255–268.

(226) Jung Jing Oh, Kurt W Hillig, Kuczkowski, R. L. Microwave Spectrum and Structure of the Pyridine-Sulfur Dioxide Complex. *Angewandte Chemie International Edition in English* **1991**, *113* (20), 7480–7484.

(227) Rajasekhar, B. N.; Veeraiah, A.; Sunanda, K.; Jagatap, B. N. Excited States of Aniline by Photoabsorption Spectroscopy in the 30 000-90 000 cm^{-1} Region Using Synchrotron Radiation. *Journal of Chemical Physics* **2013**, *139* (6).

(228) Wojciechowski, P. M.; Zierkiewicz, W.; Michalska, D.; Hobza, P. Electronic Structures, Vibrational Spectra, and Revised Assignment of Aniline and Its Radical Cation: Theoretical Study. *Journal of Chemical Physics* **2003**, *118* (24), 10900–10911.

(229) Honda, Y.; Hada, M.; Ehara, M.; Nakatsuji, H. Excited and Ionized States of Aniline: Symmetry Adapted Cluster Configuration Interaction Theoretical Study. *Journal of Chemical Physics* **2002**, *117* (5), 2045–2052.

(230) Dunitz, J. D.; Taylor, R. Organic Fluorine Hardly Ever Accepts Hydrogen Bonds. *Chemistry - A European Journal* **1997**, *3* (1), 89–98.

(231) Cozzi, F.; Bacchi, S.; Filippini, G.; Pilati, T.; Gavezzotti, A. Synthesis, X-Ray Diffraction and Computational Study of the Crystal Packing of Polycyclic Hydrocarbons Featuring Aromatic and Perfluoroaromatic Rings Condensed in the Same Molecule: 1,2,3,4-Tetrafluoronaphthalene, -Anthracene and -Phenanthrene. *Chemistry - A European Journal* **2007**, *13* (25), 7177–7184.

(232) Esterhuysen, C.; Heßelmann, A.; Clark, T. Trifluoromethyl : An Amphiphilic Noncovalent Bonding Partner. *ChemPhysChem* **2017**, *18*, 772–784.

(233) Cole, G. C.; Legon, A. C. Non-Linearity of Weak B ⋯ H-C Hydrogen Bonds: An Investigation of a Complex of Vinyl Fluoride and Ethyne by Rotational Spectroscopy. *Chemical Physics Letters* **2003**, *369* (1–2), 31–40.

(234) Braga, D.; Grepioni, F.; Tedesco, E. X-H⋯π (X = O, N, C) Hydrogen Bonds in Organometallic Crystals. *Organometallics* **1998**, *17* (12), 2669–2672.

(235) Mei, H.; Han, J.; Fustero, S.; Medio-Simon, M.; Sedgwick, D. M.; Santi, C.; Ruzziconi, R.; Soloshonok, V. A. Fluorine-Containing Drugs Approved by the FDA in 2018. *Chemistry - A European Journal* **2019**, *25* (51), 11797–11819.

(236) Hobza, P.; Špirko, V.; Havlas, Z.; Buchhold, K.; Reimann, B.; Barth, H. D.; Brutschy, B. Anti-Hydrogen Bond between Chloroform and Fluorobenzene. *Chemical Physics Letters* **1999**, *299* (2), 180–186.

(237) Reimann, B.; Buchhold, K.; Vaupel, S.; Brutschy, B.; Havlas, Z.; Špirko, V.; Hobza, P. Improper, Blue-Shifting Hydrogen Bond between Fluorobenzene and Fluoroform. *Journal of Physical Chemistry A* **2001**, *105* (23), 5560–5566.

(238) Cockett, M. C. R.; Miyazaki, M.; Tanabe, K.; Fujii, M. Isomer Selective IR-UV Depletion Spectroscopy of 4-Fluorotoluene-NH$_3$: Evidence for π-Proton-Acceptor and Linear Hydrogen-Bonded Complexes. *Physical Chemistry Chemical Physics* **2011**, *13* (34), 15633–15638.

(239) Buchhold, K.; Reimann, B.; Djafari, S.; Barth, H. D.; Brutschy, B.; Tarakeshwar, P.; Kim, K. S. Fluorobenzene and *p*-Difluorobenzene Microsolvated by Methanol: An Infrared Spectroscopic and Ab Initio Theoretical Investigation. *Journal of Chemical Physics* **2000**, *112* (4), 1844–1858.

(240) Kryachko, E.; Scheiner, S. CH···F Hydrogen Bonds. Dimers of Fluoromethanes. *Journal of Physical Chemistry A* **2004**, *108* (13), 2527–2535.